Exploitation of Reactions at Counter Electrode for Electrochemical Detection and Imaging

Qiao Liu

Ecole Doctorale Chimie-Mécanique-Matériaux-Physique (C2MP) ED606

Laboratoire de Chimie Physique et Microbiologie pour les Matériaux et l'Environnement (LCPME)

Thèse

Présentée et soutenue publiquement pour l'obtention du titre de

DOCTEUR DE l'UNIVERSITE DE LORRAINE

Mention : CHIMIE

Par **Qiao LIU**

Sous la direction de Alain WALCARIUS

Exploitation des Réactions à la Contre Electrode pour la Détection Electrochimique et l'imagerie

19 Décembre 2022

Membres du jury :

Directeur de thèse :	**Dr. Alain WALCARIUS**	**Directeur de Recherche CNRS, LCPME, Nancy**
Rapporteurs :	**Prof. Luigi FALCIOLA** **Dr. Sophie GRIVEAU**	**Professeur, Université de Milan, Milan, Italie** **Maitre de Conférence, Chimie ParisTech, Paris**
Examinateurs :	**Dr. Jean-François LEMINEUR** **Prof. Jose-Paulo PINHEIRO** **Dr. Caroline BONNET**	**Maitre de Conférence, Université Paris Diderot, Paris** **Professeur, Université de Lorraine, LIEC, Nancy** ***(Président du jury)*** **Maitre de Conférence, Université de Lorraine, LRGP, Nancy**
Membre invité (co-encadrant de la thèse):	**Dr. Liang LIU**	**Chargé de recherche CNRS, LCPME, Nancy**

Doctoral School Chemistry-Mechanics-Materials-Physics (C2MP) ED606

Laboratory of Physical Chemistry and Microbiology for Materials and the Environment (LCPME)

Thesis

Presented and publicly defended for the title of

DOCTOR OF THE UNIVERSITY OF LORRAINE

Mention: CHEMISTRY

By **Qiao LIU**

Supervised by Alain WALCARIUS

Exploitation of Reactions at Counter Electrode for Electrochemical Detection and Imaging

Public defense scheduled on 19 December 2022

Jury members:

Supervisor :	**Dr. Alain WALCARIUS**	**Directeur de Recherche CNRS, LCPME, Nancy**
Reviewers :	**Prof. Luigi FALCIOLA** **Dr. Sophie GRIVEAU**	**Professeur, Université de Milan, Milan, Italie** **Maitre de Conférence, Chimie ParisTech, Paris**
Examiners :	**Dr. Jean-François LEMINEUR** **Prof. Jose-Paulo PINHEIRO** **Dr. Caroline BONNET**	**Maitre de Conférence, Université Paris Diderot, Paris** **Professeur, Université de Lorraine, LIEC, Nancy** **Maitre de Conférence, Université de Lorraine, LRGP, Nancy**
Invite (co-supervisor of the thesis):	**Dr. Liang LIU**	**Chargé de recherche CNRS, LCPME, Nancy**

Acknowledgements

Three years of my PhD passed by in a flash, and looking back on them like a dream, most of my memories are like erased, with only scattered touching fragments stored in my mind. The epidemic lasted my entire PhD career, from September 20, 2019 to Nancy, just less than three months, the Covid-19 began to spread to all parts of the world, and then each of us began to quarantine at home, going out once a week to the supermarket to stock up on food and living supplies for the next week. I felt helpless and insignificant as I stayed in my rented house praying that people would beat the virus and not burden the local government and medical staff. After almost three months of isolation at home, I was finally able to go to the lab at the end of May, 2020, but in order to keep a safe distance, everyone could not go to the lab every day, and only one person could stay in each lab. Therefore, there was very little communication with my classmates during this period. Looking back at the situation two years ago, I have to sigh again that time is running out. To be honest, I was very apprehensive before coming to this lab because my basic knowledge of electrochemistry was not very good, and I did not study it in depth during my master's degree, so I started from zero in my PhD. I did not know anything about the study field I was going, and even though my supervisor gave me the preparation for the experiments, I was still very confused about what literature to read and how to solve the problems I encountered. I was also very anxious and helpless inside. I would like to thank my two supervisors, **Alain Walcarius** and **Liang Liu**, for their help and guidance in my research. I remember when I first came this lab, my English was very poor and my listening and expressions were not up to par, but **Alain** listened to me very patiently and explained to me many times when I did not understand what he said. Although I didn't report my study work to him every week, he gave me good advice and guidance every time I reported. He is a very academically rigorous person, and I am very grateful to him for his seriousness in revising my papers and giving me many important suggestions and inspirations. I also appreciate his ability to guide me in my academic presentations before each international conference, and despite the fact that my pre-speeches reveal many flaws, he does not criticize me, but always encourages me before giving advice. I am very grateful for his ability to protect the self-esteem of his student. I am also grateful for **Liang 's** guidance in these three years. I am very lucky to have met a teacher who is very strict with himself, his research, and his students. Since my writing skills are very

weak, whether it is writing a paper or a conference abstract he will help me reorganize the content according to the general content I wrote in his strict and concise language. And when I encountered problems during the experiments, he would personally take me through the experiments to help me solve the problems I encountered. To be honest, I was not a frugal student, I was personally rebellious and often ignored the experimental suggestions he gave me, thus causing the progress of the experiment to be hindered. I know that he wants to improve my research ability and I know what he expects from me, and I am grateful that he does not give up on me. I am sorry that I may have let him down due to my own reasons. But no matter what, I learned a lot from him, to be rigorous and respectful of scientific research, and to write with respect for facts without exaggeration. Through him, I also learned that I am not really suitable for scientific research, and I started to think that life is short, and it is important to stop following the clouds and do what I can do.

I would also like to thank my many friends for their help during these three years. **Himanshu** is a very patient and enthusiastic person. I didn't speak English well when I first came to the lab, and I was afraid to speak. But he would take the initiative to communicate with me. He was afraid that I wouldn't understand and would use translation software to help me understand each time. He also provided me with so much help in life, going to the nearby supermarket, helping me apply for discount cards, and so on. I remember that after he graduated, he stayed in Nancy to look for a job, and since I didn't speak French he took me to the hospital many times to have a gastroscopy. I will never forget his help. When I just came to Nancy, **Guofeng Lu** helped me with many things in life and study. He helped me to apply for my bank card. I still remember that it was very difficult to apply for my bank card, he was already in his third year of PhD and had to do many experiments, but he had to leave the lab very early in the afternoon to help me with my bank card. He was responsible for my phone card, enrollment, and insurance. He is really a very responsible and helpful person, and I will always remember this friendship. I also thank **Ning Dang** and **Jianren Wang**, who I would often talk to when I was helpless in my research, one for psychological comfort and the other for research inspiration. It was a blessing to know them. I am also grateful to **Xie Wang** during my research journey, in fact I really like her cooking, it is very delicious. I appreciate her optimism, cheerfulness and spontaneity, and I always say that she is like the sun, always giving positive energy.

I think God favored me because my English was very slow to improve during the first two years of the epidemic due to the lack of communication with other people, and in my third year I met **Rabita**. We actually met in my first year in French, but I hardly remembered her at that time, and even afterwards, during the chemistry class break, I only paid for a cup of coffee for her, which was only 1 euro. Then she went back to her country, Malaysia, due to the epidemic, and I never had any contact with her again. Near the third year of my PhD, she returned to Nancy and contacted me as the epidemic in France subsided, and our friendship continued. Thank her for traveling with me, I remember when I went to Spain, all my things were stolen, she went to the police office with me, went to the embassy together to apply for a temporary passport, helped me to solve the problem of survival during the trip, she is very optimistic and kind-hearted, we have been to many countries together, leaving a lot of good memories, I am very grateful to God for letting me meet her! I also met another good friend of mine, **Harpreet Singh**, in my third year of Ph.D. Before he came to this lab, Liang told me that an Indian student was coming to this lab for his Ph.D. I told Liang before I went on my trip that I could have him in the same office with me. When I came back from my trip, I did find an Indian guy in my office. He seemed very shy at that time. After getting to know him, I realized that he was very smart and enthusiastic. He helped me rewrite the arduino code when I needed to synchronize the camera with the electrochemical workstation for my experiment. He also helped me design my microelectrode template. He knows a lot of things and every time I had a network problem, he would help me solve it. I am very grateful to **Mariela Brites Helu** and **Gustavo Adrian**, **Mariela** knows a lot about electrochemistry, when I first came here, I would ask her for help when I had experimental problems and she would explain it to me patiently. I am also grateful for her help in purchasing and setting up the optical platform for my experiments, as well as helping me synchronize the camera and electrochemistry workstation. Finally, I would like to thank all of you for the good friends I met, such as **Magdalena**, **Dyia**, **Fatin**, **Ranine**, **Asma**, **Anil**, **Wassim**, **Amira**, **Julius**, **Madjid**, **Feifei Li**, *etc*. I am grateful for the time we spent together. I would like to thank you all for your company and for making our PhD life more colorful.

I am grateful to my parents for their support. My parents are silent and small to the world, but to me they are very great, they are farmers without much education, but they are people of high principle and moral character. They were hard-working, and frugal

to send my brother and me from the countryside to the wider world. When I was young, my family was often in trouble, and I could appreciate the helplessness of adults at that time, thinking that when I grew up, I would be able to help them. But as I grew older, I felt a sense of powerlessness. Maybe everyone is like a planet that has to orbit in its own set way. I have been studying away from home since I was in junior high school, and I really have very little time for them. When I graduated with my master's degree and found a job close to home, they thought I could finally settle down. But once again I chose to toss and turn, and after two years of work I chose to quit and go to France to study for my PhD. I didn't go home for three years due to the epidemic, and I couldn't take care of them. I'm ashamed to say that I've reached the age of maturity, but I still make them worry about me. My only hope now is to graduate and go back to be with them, and I hope they can live a long and healthy life. I am also grateful to my grandfather, who is now nearly 90 years old, and his memory is fading, but he still keeps asking my mom where I have been and when I will be home. Every time I video with him, he cries and asks when I'm going back, afraid that he won't have the chance to see me again. Please God bless him with good health and wait for me to go back to honor him. I'm also sorry for my brother and sister-in-law, their wedding should have been a family reunion, but I did not go back.

I would also like to thank myself. When I was a child, my grades were so bad that people thought I would only last until I graduated from junior high school. But I persevered until I got my doctorate. As I was not very smart, the road to education was rather winding and hard. Now that I think about it, life is just a journey to cultivate my heart. Compared to the me of yesterday, I have still improved a lot.

Lastly, I am very grateful to the China Scholarship Council for supporting the cost of my doctoral studies.

Table of Contents

Abstract

Working electrodes (WE) are more commonly used for electrochemical analysis to determine analyte concentration, to study surface electrochemical reaction dynamics and mechanism of reactions. Conversely, the role of the counter electrode (CE) is normally to stabilize the electronic circuit by balancing the current flowing through the WE. It should also be placed at an appropriate distance from WE and being of large size so that it would not interfere with the WE reaction. As far as we are aware, the current on the WE is equal to the current on the CE in both three-electrode and two-electrode systems. On that basis, so some researchers have converted the Faradaic current generated at WE into a remote fluorescence signal on CE to achieve visible detection of analytes. In addition, the electrochromic CE also has been used to study the local catalytical activity of WE material. It must be noted, however, that CE is still given much less attention than WE.

The main objective of this thesis is to study the electrochemical analysis from CE instead of WE. Our study focuses on two study points based on CE: one for concentration analysis based on stripping voltammetry on CE, and the other for mapping WE's electrochemical reactivity via local optical changes on CE.

As we known, electrochemical stripping analysis (anodic, cathodic, or adsorptive) is usually based on the pre-concentration of a target analyte on the WE surface and then measuring its quantity *via* its direct quantitative electrochemical transformation (with the electrode refreshed afterwards). However, not all analytes could be pre-concentrated on the WE.

To solve this problem, in the first study point, we demonstrated a new approach to carry out electrochemical stripping analysis of non-adsorbing species, thus not based on the analyte being directly pre-concentrated on the WE, but on the signal obtained indirectly from CE where metal ions are reduced and then electrochemically stripped. Different from the CE with large surface area in classical electrochemical measurements, an ultramicroelectrode is chosen here as CE to purposely exploit the polarization effect. The concept is based on oxidizing the analyte on WE in one compartment of the electrochemical cell while reducing Cu^{2+} on CE from another compartment connected with an ionic bridge or a less common metal “bridge”. The deposited Cu on CE is then analyzed by stripping in another three-electrode cell, and the charge shows good linear

relationship with the concentration of analyte in the former cell. As the stripping current response (peak) is much clearer than the small current variations corresponding to the direct oxidation of the analyte, it improves the resolution of raw signal. Besides, it may also reduce the background signal from blank solution by "filtering" the non-Faradaic charge. Like in classical electrochemical stripping analysis, one may also prolong the oxidation time in exchange for higher sensitivity of analysis. This work extends the applications of stripping analysis and offers a new angle of electroanalysis by capturing signals from CE.

In addition, understanding local electrochemical reactivity of surfaces is crucial for electrode design and applications at device level, in the fields of energy storage, biosensing, electrocatalysis, *etc.* It is generally measured through two strategies: scanning probe approaches and optical imaging. The former is based on scanning a probe that is close to the sample surface and measuring signals from the probe. This includes scanning electrochemical microscopy, scanning ion conductance microscopy and scanning electrochemical cell microscopy. These methods may reach high spatial resolution in nanometer range, yet are naturally slow due to the point-to-point scanning of the probe. On the other hand, optical imaging may offer much higher throughput by directly mapping the surface. A common way is to design reactions that may induce optical change of the working electrode, such as surface plasmon resonance, electrochemiluminescence and fluorescence. They may offer a balanced spatial and temporal resolution in mapping, but they require specific reactions that may not be compatible for all electrodes and electrolytes.

In the second study point, we attempt to optically map the local electrochemical reactivity of surfaces not by "looking" at the working electrode (WE), but by measuring optical change of the counter electrode (CE). The concept is based on an electrochromic CE that changes color with electron transfer accompanying ion intercalation. Experimentally, a planar WE including some active areas is placed in parallel with a transparent conductive electrochromic CE (WO_3 film on indium-tin oxide (ITO) electrode), using micro-meter spacer (made of PTFE sheet with hole), where water is oxidized locally on WE and WO_3 is reduced correspondingly on CE. An optical microscope with complementary metal oxide semiconductor (CMOS) camera is used to record the color change of the CE under red light (623 nm) while applying a suitable anodic potential on WE. The results show that the optical absorption of CE reduces locally at positions corresponding to the active area of WE. The change can be captured

dynamically in the form of video, which offers information on the transient behavior of the system. The signals are further analyzed by modelling for retrieving the map of reactivity of WE. The spatial resolution of CE imaging decreases as the distance between WE and CE increases, likely due to the homogenization of current distribution on CE. The reported method could avoid the modification of neither the WE nor the electrolyte, which may be generic for measuring “invisible” electrochemical reactions.

Résumé étendu en français

L'électroanalyse constitue une approche de choix pour la détection d'analytes cibles, car elle permet l'obtention par une instrumentation relativement simple et peu couteuse de signaux électrochimiques tels que le potentiel ou le courant. L'application la plus aboutie de l'électroanalyse est probablement le capteur ampérométrique de glucose, qui est commercialisé et couramment utilisé dans la vie quotidienne. Pour arriver à une méthode électroanalytique performante, il est essentiel de considérer les réactions électrochimiques ayant lieu à la surface des électrodes, la distribution du courant, ainsi que le transport de masse de l'analyte, qui sont liés au processus de mesure. Néanmoins, la plupart des recherches en électrochimie analytique se concentrent UNIQUEMENT sur l'élaboration de l'électrode de travail (WE pour « *working electrode* ») et sur les réactions de transfert d'électrons qui y ont lieu. La WE est le plus couramment utilisée en analyse électrochimique pour déterminer la concentration de l'analyte cible, pour étudier la dynamique des réactions électrochimiques de surface et/ou les mécanismes des réactions de transfert de charge. A l'inverse, le rôle de la contre-électrode (CE pour « *counter electrode* ») est normalement de stabiliser le circuit électronique en équilibrant le courant qui traverse la WE. Elle doit également se trouver à une distance appropriée (pas trop près) et être de grande taille afin de ne pas interférer avec les réactions ayant lieu à la surface de la WE. En général, on ne s'occupe que des réactions à la WE. Ceci étant, comme le courant passant au travers de l'électrode d'entrée est égal à celui traversant l'électrode de sortie, à la fois dans les systèmes à deux et trois électrodes, quelques chercheurs ont converti le courant faradique généré à l'électrode d'entrée (WE) en un signal de fluorescence à distance sur l'électrode de sortie (CE) afin de réaliser une détection visualisable des analytes. Ceci peut également être réalisé en ayant recours à une CE électrochrome, comme cela a été démontré pour l'étude de l'activité catalytique locale du matériau de la WE. Il faut cependant noter que l'exploitation des réactions à la CE restent extrêmement rares à comparer aux études menées sur celles ayant lieu à la surface de la WE.

L'objectif principal de cette thèse est de proposer de nouvelles approches électroanalytiques basées sur l'exploitation des réactions à l'EC au lieu de celles ayant lieu à la surfaced de la WE. Notre étude se concentre sur deux processus distincts à la CE : l'un exploitant le dépôt métallique à la CE pour l'analyse par redissolution

anodique d'espèces habituellement impossible à détecter à la WE par cette méthode, et l'autre exploitant le caractère électrochrome de la CE pour la cartographie de la réactivité électrochimique de la WE via des changements optiques locaux sur la CE.

Comme nous le savons, la voltampérométrie par redissolution d'électrode (anodique, cathodique ou par désorption) est basée sur la préconcentration électro-induite d'un analyte cible sur la surface de l'électrode de travail, puis sur la mesure de sa quantité via sa transformation électrochimique quantitative directe par redissolution des espèces accumulées (la surface de l'électrode étant ensuite régénérée). Cependant, elle n'est pas applicable aux analytes qui ne peuvent pas se déposer ou s'adsorber sur la surface de l'électrode de travail.

Dans le premier chapitre expérimental, nous proposons une nouvelle approche et démontrons son aptitude à pouvoir réaliser une analyse par préconcentration et redissolution électrochimique, non pas basée sur la l'accumulation directe de l'analyte sur l'électrode de travail (WE), mais sur le signal obtenu indirectement à la contre-électrode (CE). Contrairement aux CE à grande surface habituellement utilisée pour les mesures électrochimiques classiques, une électrode de petite taille (microélectrode) est choisie ici comme CE pour exploiter délibérément l'effet de polarisation. Le concept est illustré à la **Figure 1**. La cellule 1 est composée de deux compartiments (dénommés Cell 1a et Cell 1b). La première électrode de travail (WE1) et l'électrode de référence associée (RE1) sont placées dans une première demi-cellule (Cell 1a) contenant un analyte modèle (ferrocènedimethanol, $Fc(MeOH)_2$), et la contre-électrode associée à ce circuit (CE1) est placée dans une seconde demi-cellule séparée (Cell 1b) contenant une solution de Cu^{2+}. Les deux demi-cellules (Cell 1a et Cell 1b) sont reliées entre elles par un conducteur métallique ou ionique servant de « pont ». Le principe de la mesure est le suivant. L'oxydant de $Fc(MeOH)_2$ à la WE1 dans la cellule 1a conduit à la réduction simultanée de Cu^{2+} et le dépôt de Cu métallique sur CE1 dans la cellule 1b. La quantitée de Cu formé sur CE1 est directement liée à la quantité de charge correspondant à l'oxydation de $Fc(MeOH)_2$ sur WE1, qui est elle-même dépendante de la concentration de $Fc(MeOH)_2$ dans la Cellule 1a. Ainsi, en mesurant la quantité de Cu déposée, par redissolution anodique (en utilisant WE2 = CE1) dans un système traditionnel à trois électrodes (Cell 2) contenant uniquement une solution électrolytique ($NaNO_3/HNO_3$, pH=2), on peut indirectement avoir accès à la concentration de l'analyte cible dans la première cellule (Cell 1a).

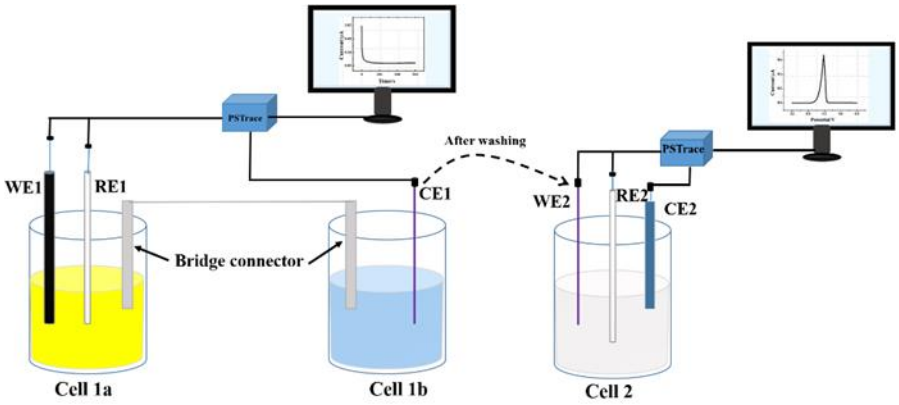

Figure 1. Diagramme schématique illustrant la détection indirecte de $Fc(MeOH)_2$. Après avoir oxydé l'analyte cible à la WE1 dans la première demi-cellule (Cell 1a) et concomitamment réduit Cu^{2+} à la CE1 dans la seconde demi-cellule (Cell 1b), CE1 est transférée dans la seconde cellule (Cell 2) et connectée en tant que WE2 pour la redissolution anodique du Cu métallique formé sur la microélectrode.

A la fois la voltampérométrie à balayage linéaire et la chronoampérométrie peuvent être appliquées pour l'oxydation de $Fc(MeOH)_2$. Cependant, les premiers résultats indiquent que le signal de la solution d'électrolyte vierge (c'est-à-dire sans $Fc(MeOH)_2$) ne peut être efficacement masqué qu'en chronoampérométrie (**Figure 2**), si bien que cette technique a été utilisée dans la suite du travail. La chronoampérométrie offre également l'avantage d'accroitre l'intensité des signaux en prolongeant le temps d'application du potentiel, tout comme pour l'étape de préconcentration en analyse classique par redissolution d'électrode. La relation entre la quantité de Cu déposée et la charge d'oxydation de $Fc(MeOH)_2$ est systématiquement étudiée, et des courbes d'étalonnage sont établies avec le $Fc(MeOH)_2$ variant de 0 à 10 µM. Comme on peut le constater (**Figure 3**), la réponse obtenue à la contre-électrode est linéaire sur tout le domaine des concentrations étudiées, alors que la mesure directe de la charge passée au travers de l'électrode de travail conduit à une moins bonne limite de détection et une non linéarité de la réponse ampérométrique. Il s'avère également que la concentration de Cu^{2+} et le pH dans la cellule 1b peuvent affecter de manière significative la conversion de la charge. Par contre, nous n'avons pas observé d'effet de la nature du pont utilisé pour séparer les deux compartiments (ponts salins ou métalliques) qui ont toujours donné exactement les mêmes signaux, indiquant que le potentiostat fonctionne normalement dans les conditions expérimentales utilisées.

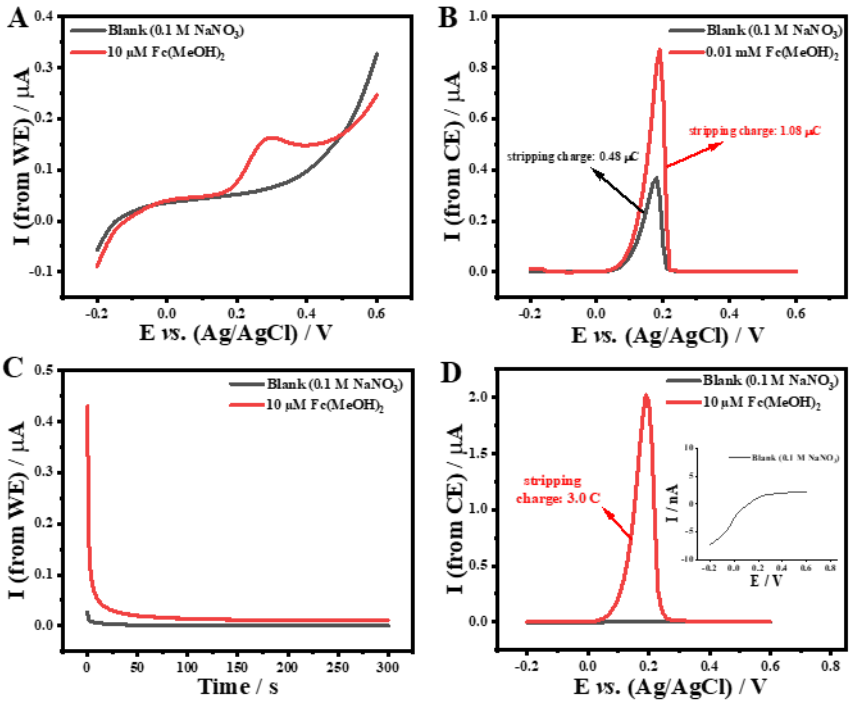

Figure 2. (A) Volatmpérométrie linéaire (LSV) enregistrée à 50 mV/s à une électrode de carbone vitreux en présence (courbe rouge) et en absence (courbe noire) de 10 µM Fc(MeOH)$_2$ dans la cellule 1a. (B) Courbes de redissolution anodique correspondantes (oxydation de $Cu^{(0)}$ déposé sur CE1, mesuré par LSV dans la cellule 2 après traitement « (A) ». (C) Chronoampérométrie à un potentiel de +0,3 V (*vs.* Ag/AgCl) réalisée dans les mêmes solutions qu'en (A). (D) Courbes de redissolution anodique correspondantes après traitement « (C) ». Concentration de Cu^{2+} dans la cellule 1b: 0,02 M; « pont » connecteur : fil de cuivre.

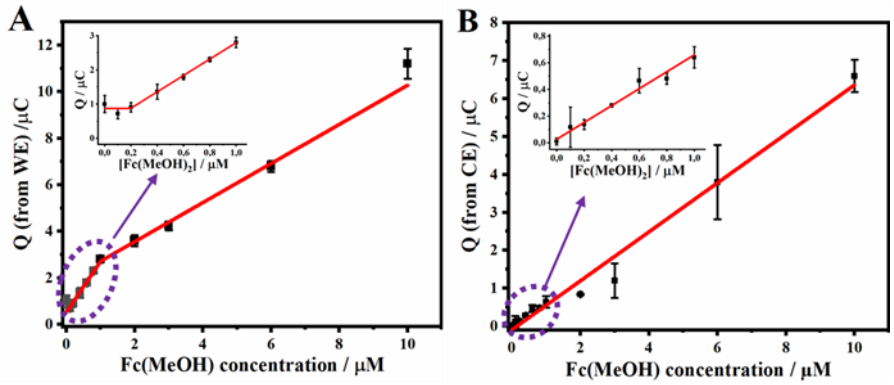

Figure 3. Courbes de calibration obtenues en utilisant le signal de l'électrode de travail (A) ou celui de la contre-électrode (B) pour la détection de concentrations croissantes de Fc(MeOH)$_2$; potentiel appliqué à WE1: +0,3 V (800 s) ; solution dans la cellule 1b : 0,2 M $CuSO_4$ (pH 2). Inserts : agrandissement de la gamme de concentration 0-1µM.

Les résultats de ce travail exploratoire visant un nouvel accès à l'analyse électrochimique en exploitant les signaux de la contre-électrode pour une détection indirecte par redissolution anodique pourraient conduire à une extension des applications de l'analyse par redissolution d'électrode à des analytes cibles qui ne peuvent pas se déposer ou s'adsorber sur une électrode de travail.

Par ailleurs, la compréhension de la réactivité électrochimique de surface à l'échelle locale est cruciale pour la conception des électrodes et leurs applications au sein de dispositifs, en particulier dans les domaines du stockage de l'énergie, de la biodétection ou de l'électrocatalyse. Cette réactivité de surface est généralement appréhendée selon deux stratégies : les approches par sonde à balayage et l'imagerie optique. La première est basée sur le balayage d'une sonde proche de la surface de l'échantillon et sur la mesure des signaux émis par cette sonde. Cela inclut la microscopie électrochimique à balayage, la microscopie de conductance ionique à balayage et la microscopie à balayage de cellule électrochimique. Ces méthodes peuvent atteindre une haute résolution spatiale de l'ordre du nanomètre, mais sont naturellement lentes en raison du balayage point par point de la sonde. En revanche, l'imagerie optique peut offrir un débit beaucoup plus élevé en cartographiant directement la surface. Une méthode courante consiste à concevoir des réactions susceptibles d'induire un changement optique de l'électrode de travail, comme la résonance plasmonique de surface, l'électrochimiluminescence et la fluorescence. Elles peuvent offrir une résolution spatiale et temporelle équilibrée pour des mesures de cartographie, mais elles nécessitent des réactions spécifiques qui peuvent ne pas être compatibles avec toutes les électrodes et tous les électrolytes.

Fort de ces observations, nous proposons dans le deuxième chapitre expérimental de cartographier optiquement la réactivité électrochimique locale des surfaces non pas en « regardant » l'électrode de travail (WE), mais en mesurant le changement optique de la contre-électrode (CE). Le concept est basé sur une CE constituée d'un matériau à propriétés électrochromes (telle que WO_3, connu pour changer de couleur lors d'un transfert d'électrons accompagné par l'intercalation d'ions compensateurs de charge). Le principe de la mesure est illustré à la **Figure 4**. Il implique de positionner la CE électrochrome toute proche d'une WE constituée d'un réseau de

microélectrodes et de les faire fonctionner en tant que système à deux électrodes dans l'eau pure (sans ajout d'électrolyte). Dans ces conditions, lorsque l'eau est oxydée localement sur la WE, le WO_3 est réduit de manière correspondante sur la CE (**Fig. 4a**). Expérimentalement, une WE plane est placé en parallèle avec une CE électrochrome conductrice et transparente, en utilisant un espaceur en plastique (d'épaisseur comprise entre 5 et 100 µm). Un microscope optique avec une caméra CMOS (*complementary metal oxide semiconductor*) est utilisé pour enregistrer le changement de couleur de la CE sous lumière rouge (λ = 623 nm) tout en appliquant un potentiel anodique approprié à la WE (**Fig. 4b**). Les résultats préliminaires montrent que l'absorption optique de la CE diminue localement à des positions correspondant à la zone active de la WE (**Fig. 4c**).

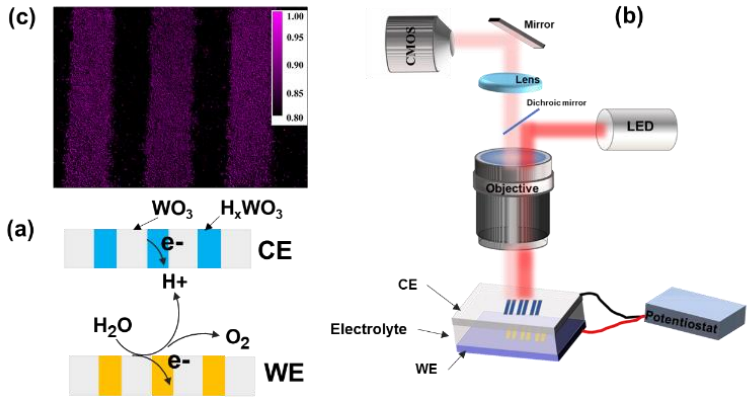

Figure 4 (a) Schéma de principe de la mesure : réactions redox ayant lieu à la surface des WE et CE (WE : la couleur jaune représente la région active ; CE : la couleur bleue est $HxWO_3$ et la couleur grise est WO_3). (b) Illustration schématique d'une technique d'imagerie par courant électrochimique. (c) Image électrochrome de la contre-électrode observée en appliquant un potentiel de 1,6 V.

Ce changement de couleur peut être capturé dynamiquement sous forme de vidéo, ce qui offre des informations sur le comportement transitoire du système. Les signaux sont ensuite analysés par modélisation pour obtenir la carte de réactivité de la WE. La résolution spatiale de l'imagerie CE diminue lorsque la distance entre WE et CE augmente, probablement en raison de l'homogénéisation de la distribution du courant sur la CE. L'eau pure en tant qu'électrolyte a une résistance élevée, ce qui permet d'inhiber la dispersion latérale du courant dans la solution. De plus, en raison d'un électrolyte faiblement supporté, la migration pourrait également jouer un rôle important. Les ions H^+ libérés lors de l'oxydation de l'eau (catalysée par l'application d'un

potentiel positif à la WE) sont susceptibles de migrer vers la CE, contribuant ainsi à localiser la distribution de courant sur la CE. L'effet du temps d'application du potentiel (à tension constante), de la valeur de ce potentiel et de la distance entre les électrodes WE et CE, sur le changement optique local de CE est également exploré. Comme illustré sur les **Figures 5 & 6**, on constate qu'un temps plus long (**Fig. 5**) et une tension plus élevée (**Fig. 6**) conduisent à des changements de couleur plus uniformes sur la surface CE en raison de la propagation de charge latérale. Par conséquent, la meilleure résolution pourrait être obtenue en ajustant la distance, le temps et la tension entre WE et CE. La méthode développée ici permet donc d'effectuer une imagerie de la réactivité de surface d'une WE tout en évitant sa modification ou l'usage d'unélectrolyte ad'hoc, offrant une approche universelle pour observer des réactions électrochimiques « invisibles ».

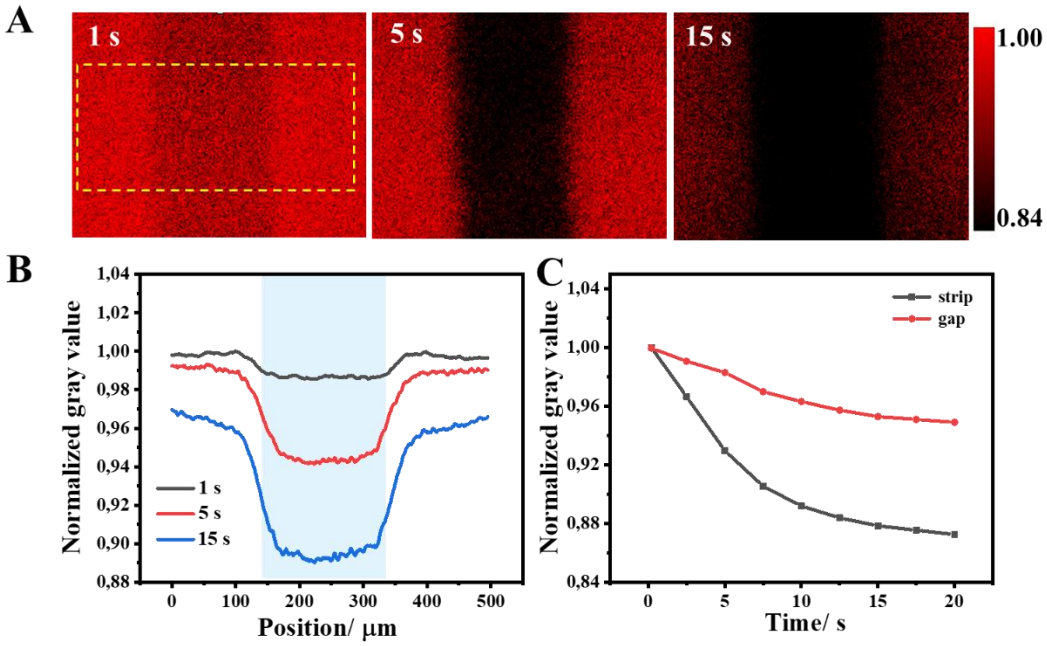

Figure 5. Effet du temps sur le changement de couleur de la CE polarisée à un potentiel de 1,90 V. (A) Images des changements de couleur de la CE à différent temps. (B) Variation des valeurs de gris normalisées, mesurées dans les régions correspondantes au rectangle jaune en pointillés dans la partie (A) de la figure, à différent temps. (C) Variation des valeurs de gris normalisées en fonction du temps, pour la bande conductrice de la WE (strip) et l'espace entre deux bandes (gap).

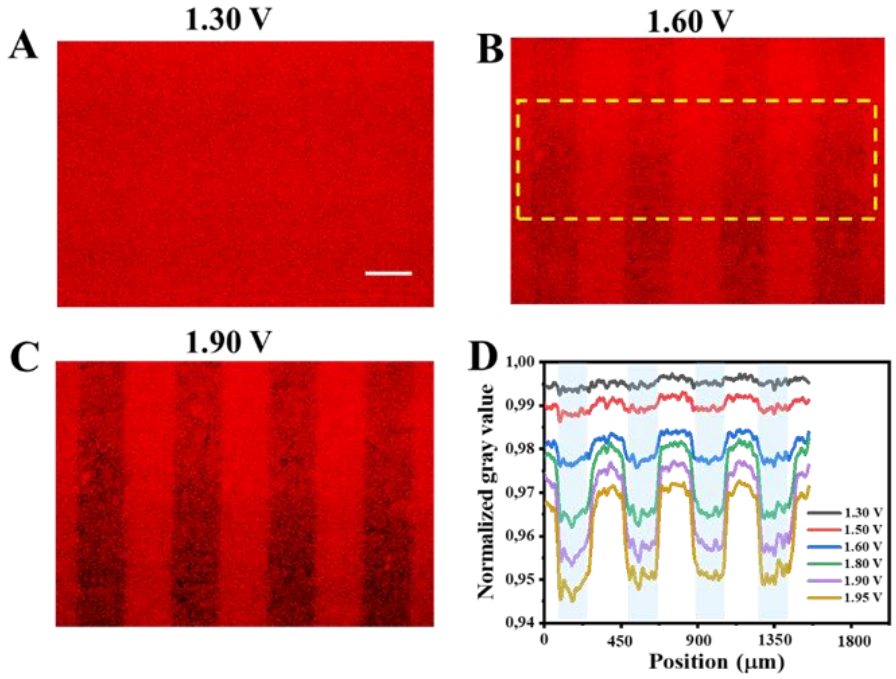

Figure 6. (A-C) Images des changements de couleur de la CE polarisée à des potentiels respectifs de 1,30 V (A), 1,60 V (B) et 1,90 V (C). (D) Variation des valeurs de gris normalisées, mesurées à différents potentiels imposés dans la région correspondante au rectangle jaune en pointillés dans la partie (B) de la figure, pour les bandes conductrices de la WE et les espaces entre elles.

Chapter I

Introduction

Electrochemical analysis is an important domain in electrochemistry and analytical chemistry [1,2]. It directly converts chemical information such as concentration and reactivity to electronic signals (potential or current) that can be read by modern instrumentation [3–5]. For example, potentiometry measures the equilibrium potential without any excitation signal and it is a common method for measuring pH and concentration of various ions (Na^+, K^+, Ca^+, Cl^-, *etc*.) using ion-selective electrodes [6,7]. Amperometry and voltammetry apply a potential signal and record the current response. Depending on the waveform of the applied potential, the electrochemical analysis can be in time (chrono methods) [8,9], frequency (AC methods) [8,10] or potential (cyclic voltammetry) domain [11–13]. Pulse or square wave voltammetry is often used to improve the sensitivity of such dynamic methods of electroanalysis [9,13–15]. Needless to say, electrochemical analysis has been widely applied in environmental analysis and biosensing [15–17].

Nevertheless, electrochemical analysis is often regarded as a cheap alternative of competing analytical methods, notably chromatography and mass spectrometry. The highlight is usually on the cost and ease of operation, rather than analytical aspects of sensitivity, selectivity, and reproducibility. A typical example is household glucose sensor [18], which is perhaps the most successful (bio)electrochemical sensor in the market [19] even though it may never provide the same information and accuracy as professional blood analysis in laboratories [20].

In most electroanalysis research, one cares only about the reactions on the working electrode (WE), presumably considering that the counter electrode (CE) side is negligible. This requires that the CE is stable, active and sufficiently distant from the WE with a large active surface area. However, these criteria are not always fulfilled in the design of electroanalytical devices due to practical restrictions such as size, space, sample volume and waste management. Therefore, improving the application of CE according to the design of electroanalytical devices is meaningful for solving some practical questions.

In this work, we are attempting to obtain the electrochemical information on CE instead of WE. We mainly focus on two study aspects: (1) concentration analysis, by analyzing copper stripping signal on micro-CE to indirectly determine the analytes concentration that can't be preconcentrated on the WE surface. (2) local surface reactivity analysis, by mapping the electrochromic on the CE to measure local electrochemical reactivity on the WE. Herein, the main goal of this chapter is to provide overview of related information about research aims, the related background will be introduced at here. The general role of CE is introduced in **Section 1.1**. The stripping voltammetry analysis is discussed in **Section 1.2**. State-of-the-art electrochemical imaging tools are briefly introduced in **Section 1.3**. The study of electrochromic material is presented in **Section 1.4**.

1.1 Counter electrode in electrochemistry

1.1.1 Introduction to the general role of counter electrode

In electrochemical analysis, the CE are mainly used to complete the circuit and allow current flow in electrochemical system[21,22]. In general, CEs often have a large surface area compared to WEs due to several concerns (**Figure 1.1A**). Firstly, this minimizes CE polarization due to a low current density on a large electrode and, consequently, reduces the overall cell voltage required from the power source[23,24]. Secondly, a large CE may homogenize the current distribution in the cell, especially near the WE. This is important for weakly supported electrolyte or at high current, where the potential drop in the solution is not negligible. Moreover, if possible, CE is positioned far from WE. This is because the electroanalysis based on WE implicitly requires no cross-interference between WE and CE. However, the electrochemical potential of CE cannot be controlled, thus there is always doubt about the possible reactions on it that may locally change the electrolyte, even with a large surface area and low polarization. In this sense, inert materials such as platinum, stainless steel, and graphite are often used as CE [25,26], yet none of them is perfect. Platinum is a good electrocatalyst. This may lead to the production of gas (O_2 or H_2, or even Cl_2 when using Cl^- as supporting electrolyte) and significant local pH change in aqueous media. Stainless steel and graphite are stable under cathodic polarization, but under anodic polarization they may oxidize, causing contamination to the working electrolyte. In

some circumstances, the electrochemical cell is divided in two compartments that are separated by ion exchange membrane or glass frit, as illustrated in **Figure 1.1B**. This could reduce the cross-contamination, although would increase the resistance of the cell.

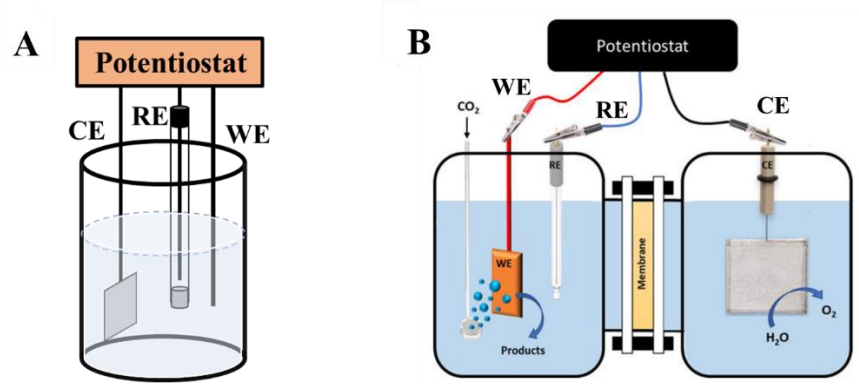

Figure 1.1 Schematic diagram of the electrochemical cell. (A) Three electrodes in single cell. (B) Three electrodes in separate cell.

1.1.2 Application of counter electrode in electroanalysis

CE is an indispensable part of an electrochemical system even for the simplest two-electrode configurations[27–29]. As current flows through it, non-Faradaic or Faradaic processes always occur at CE interface with the electrolyte. In some circumstances, people may take this advantage to complement the reactions on the CE. For example, the CE based on different designs for materials has been applied in the dye-sensitized solar cells (DSSCs) by catalyzing the reduction of I_3^- to I^- ions (**Figure 1.2A**) to achieve a high the photoelectric conversion efficiency[30]. In electrochromic devices, CE is sometimes also modified with an electrochromic material that has the same color change as WE but under opposite polarization[31]. Ruiner Engels and his co-worker synthesized organic molecules at the CE under apoptotic conditions in one-compartment cells[32]. To enhance the electrode materials catalytic activity toward the hydrogen evolution reaction (HER), Ji *et al.*[33] provided a new approach by anodic dissolving of Pt CE to cathodically activate the WE material. It differs from the general requirement that CE should not cause contamination of WE. The dissolved Pt from CE diffused and deposited on the WE material surface, enabling WE material to behave good catalysis performance, although the Pt loading on the WE material is lower. Moreover, the microelectrode has been used as CE which can improve the

electrochemical polarization and current density distribution on the CE. A few attempts have also been made to use CE for electroanalysis. Rabia Djoumer developed a new method to covert faradic current generated on the WE to remote fluorescence signal on micro-CE (microelectrode as CE)[29] (**Figure 1.2B**). The fluorescence signal recorded on the CE as a function of current recorded on the WE is plotted, which behaves a perfect linear correlation. The advantage of this method is that fluorescence-coupled electrochemical methodologies provide an intrinsic amplification mechanism due to the fact that one electron transfer can be correlated with thousands of easily detectable photons in a fluorescence event. Moreover, interdigitated electrodes arrays (IDEA) may increase the current response in amperometric analysis due to the redox cycle where the reactant for WE reactions is regenerated on the CE by the reversed reaction[34,35] (**Figure 1.2C**).

Furthermore, while CE is usually designed not to interfere with WE, in some cases it may also purposely regulate the electric field distribution by controlling its size and position relative to the WE [36,37]. A typical example is direct mode SECM, where a microelectrode serving as CE is positioned close to macro-sized WE sample. This spatially localizes the electrochemical reactions in the vicinity under the micro-CE by regulating the current flux (**Figure 1.2D**). It is widely used for patterning surfaces by local electrochemical deposition or etching, and the shape of pattern almost replicates that of the micro-CE when the distance between the sample (WE) and the microelectrode (CE) is comparable to the radius of the micro-CE [38–40]. Similarly, by placing a planar CE in parallel with a planar WE at short distance, the current distribution on WE which reflects the local electrochemical reactivity, would also cause inhomogeneous current distribution on CE. Owen *et al.*[41] reported that the color of WO_3 electrochromic CE locally changes following the exposed area of WE, and the absorption corresponds to the catalytic reactivity of the WE. They used WE array, in which each electrode had 1 mm diameter and the gap was 3 mm between adjacent electrodes. Despite a few reports, the use of CE in the domain of electroanalysis remains rare, both for analyzing the concentration of electrolyte and for analyzing the reactivity of surfaces.

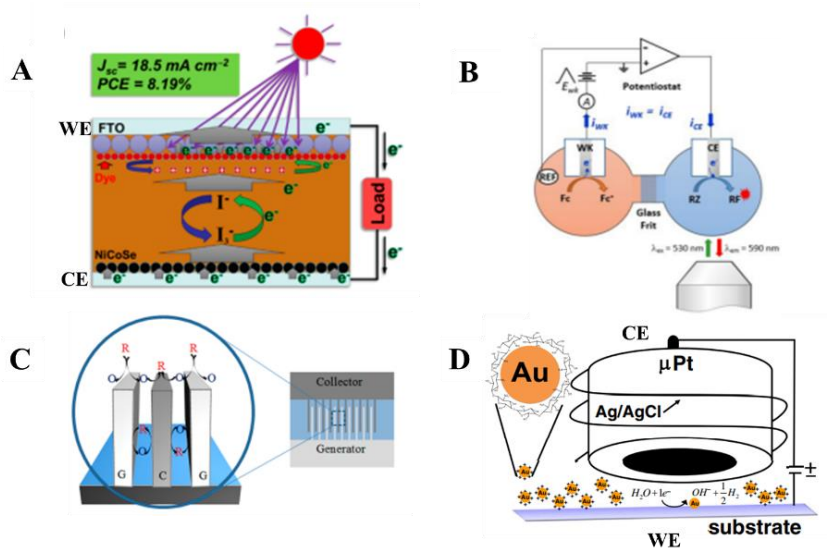

Figure 1.2 (A) Schematic diagram of the photoelectric conversion process for the ternary selenide DSSC[30]. (B) Principle of the faradaic current-to-fluorescence converter setup (the faradaic current: $i_{WE} = i_{CE}$) [29]. (C) Schematic view of principle of redox cycling in a 3D IDEA. G: Generator; C: Collector[35]. (D) Schematic presentation of local NPs deposition by the direct mode of SECM[39].

1.2 Stripping voltammetry

Stripping voltammetry (SV) was firstly reported by Zbinden in 1931. He found that the stripping current is related to the amount of copper deposited on the surface of electrode during the oxidation of copper. After decades, the development of hanging mercury drop electrode (HMDE) arised the wide application of SV techniques in natural waters and other samples [42–44]. Until today, it has been extended to measure multicomponent metal ions, non-metal ions and organic molecules in conjuction with different kinds of electrodes, showing extremely low limit of detection, high sensitivity [45–47]. It includes two steps for eletrochemical analysis: (1) the analytes are accumulated on the WE at a constant potential, called preconcentration step; (2) the analytes preconcentrated on the WE are stripped into the solution when scanning the potential at a certain range, giving rise to the occurrence of peak, called stripping step [48]. By plotting the voltammogram (current-potential), the peak current or area is proportional to the concentration of analytes at the same potential scan rate. Moreover, the peak potential could reflect the characteristic of analytes. For couducting SV analysis, some attention should be paid: (1) the test solution, to ensure the stripping

process controlled by diffusion at the condition of without stirring, the electrolyte is required to have lower resistance and migration effect. The dissolved oxygen is driven off by passing the inert gas, usually nitrogen before pre-concentration. (2) rotating the WE or stirring the sample solution at a reproducible rate to generate forced convective transport will increase the mass transfer to the WE during preconcentration. (3) generally, the stripping step is performed in the quiescent solution, moreover, the medium exchange procedure may be used if the matrix components interfere with the analysis. In this case, the sample solution is exchanged with a "clean" electrolyte solution. According to the difference of preconcentration method as well as measure step, the SV could be classfied to three types: anodic stripping voltammetry (ASV), cathodic stripping voltammetry (CSV), adsorptive stripping voltammetry (AdSV) [49–51]. Each of these is further introduced below.

Anodic stripping voltammetry: ASV is commonly used for trace or ultra-trace level detection of heavy metal ions (Cd, Hg, Pb, Cu, *etc*.) in the fields of enviroment and food. It includes the deposition of metal ions to the surface of WE at a constant potential. Usually, the deposition potential should be more negative than the reduction potential of metal ions to obtain efficient deposition. The deposition products are amalgam or metal based on the WE (mercury electrode or solid eletrode), The reaction is as follows:

$$M^{n+}+ne^{-}\rightarrow M(Hg) \quad \text{(mercury electrode)} \tag{1.1}$$

or

$$M^{n+}+ne^{-}\rightarrow M^{0} \quad \text{(mercury-free solid electrode)} \tag{1.2}$$

The time and rate of deposition as well as the WE area make an important impact to the sensitive of this method. The sensitivity is seriously influenced by the WE rotation rate or stirring solution rate under a fixed WE area. Besides, it also limited by the solubility of the metal ions in mercury eletrode. Some scientists had investigated the solubility of various metal ions in mercury by employing different study methods such as amalgam polarography, voltammetry[52,53]. It was found that the greater the solubility of the metal ions in mercury, the higher the sensitivity.

After preconcentration, the amalgam is allowed to keep several seconds at a lower potential than that of the preconcentration to enable uniform distribution of the deposited material on the mercury eletrode. But for the solid eletrode, this step is unnecessary. Then the deposited materials are oxdized at a positive potential, the reaction is shown in below:

$$M(Hg) \rightarrow M^{n+} + ne^- \quad \text{(mercury electrode)} \tag{1.3}$$

or

$$M^0 \rightarrow M^{n+} + ne^- \quad \text{(mercury-free solid eletrode)} \tag{1.4}$$

As scanning the potential to more positive potential, the anodic peak current could be obtained when the depletion of deposited or absorbed material at the surface of WE. As illustrated in **Figure 1.3** for Cu(II) detection [54], the peak current increases with an increase of Cu ion concnetration, stripping voltammogram shows two key information: the peak current and peak potential, which is helpful for both quantitative analysis and qualitative analysis.

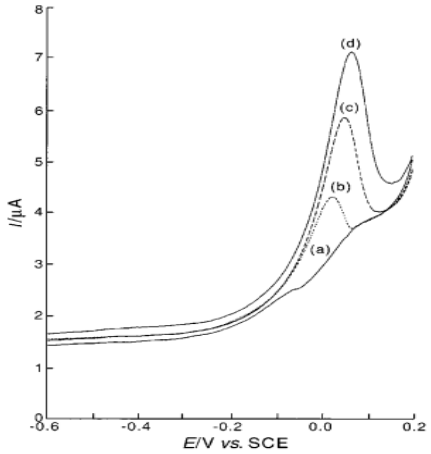

Figure 1.3 ASV responses of glassy-carbon based electrode for Cu(II) in beer sample (a) blank, and after addition of Cu(b) 507 mg L^{-1}, (c) 1522 mg L^{-1}, and (d) 2536 mg L^{-1}[54].

Cathodic Stripping Voltammetry: The CSV method could be used to detect various types of analytes including inorganic and organic substances with low solubility in the electrode. HMDE is commonly acted as WE in CSV. Different from ASV in which analytes are reduced on the surface of mercury (Hg) to form amalgam, CSV includes the formation of insoluble compound film on the WE at a more positive potential during preconcentration step. The Hg is firstly oxidized to Hg(I), the reaction is as follows:

$$2Hg \rightarrow Hg_2^{2+} + 2e^- \tag{1.5}$$

Then the Hg(I) immediately combine with analytes like halide ions and selenium (X^- = Cl^-, Br^-, I^-, Se) to form unsoluble compound on the surface of WE, according to the reaction:

$$Hg_2^{2+} + 2X^- \rightarrow Hg_2X_2 \tag{1.6}$$

At last, the unsoluble compound is stripped by scanning more cathodic potential than that of the pre-concentration step, as the reduction of Hg(I) to Hg, the X^- is released to solution and the cathodic current can be observed (**Figue1.4**), the reaction is as follows:

$$Hg_2X_2 + 2e^- \rightarrow 2Hg + 2X^- \quad (1.7)$$

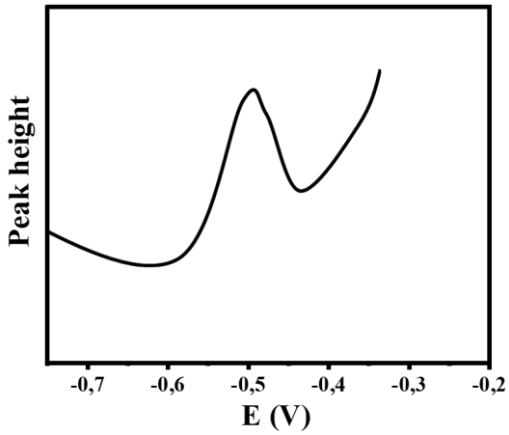

Figure 1.4 Stripping voltammograms for determination of selenium: 0.1 M HCl + 1.0 × 10^{-5} M SeO_3^{2-}, deposition time: 120 s, deposition potential: -0.2 V *vs*. SCE [55].

It has been reported that CSV is capable of detecting the halides (bromides, iodides, chlorides)[56,57], sulfides[58], thiol compounds (thiamine, cysteine, thiourea)[59], selenide[60], *etc*. By comparing ASV and CSV, it is possible to see that the stripping current in ASV is relating to the metal concentration in Hg, which means that a smaller volume could lead to improved sensitivity, whereas in CSV, the stripping current is linked to the mountings of insoluble compounds on the electrode surface, not based on the volume but on the area of the electrode. Moreover, due to the formation of insoluble thin films, the calibration curves in CSV usually exhibit nonlinear behavior at high concentrations originating from surface saturation. For low concentrations, the curves are reproducible, and can be used for analysis.

Adsorptive Cathodic Stripping Voltammetry: The AdSV is very sensitive technology for analyzing plentiful trace elements, especially for the metal ions that can not be determinated by convential stripping methods (*e.g.*,ASV). Normally, for detecting the analytes, the conventional AdSV includes three steps, the reaction principle is as follows (metal ions as example) [61]:

(1) Firstly, analytes (M^{n+}) and suitable ligands (AL^{m-}) bind together to form metal complex at an optimal pH:

$$yM^{n+} + zAL^{m-} \rightarrow M_y(AL)_z^{(y\cdot n-z\cdot m)} \quad (aq) \tag{1.8}$$

(2) Then the metal complex is accumulated onto the electrode surface by adsorption at suitable potential, as follows:

$$M_y(AL)_z^{(y\cdot n-z\cdot m)}\ (aq) \rightarrow M_y(AL)_z^{(y\cdot n-z\cdot m)}\ (ad) \tag{1.9}$$

Some factors that the ligand concentration, pH of sample solution, adsorption time, and adsorption potential need to be carefully optimized. The formation of metal complex extremely depends on the pH, so the pH of the sample solution need to be accurately controlled by pH buffer. The ligand concentration should exceed the concentration of the analytes to achieve complexation saturation. Moreover, to obtain better adsorption efficiency, the adsorption potential is slightly more positive than the reduction potential of metal complex to avoid causing the reduction of metal complex.

(3) Lastly, the metal complex adsorbed on the eletrode is reduced by scanning more negative potential, the stripping peak current could be acquired.

$$M_y(AL)_z^{(y\cdot n-z\cdot m)}(ad) + e^- \rightarrow yM^{(n-1)+} + zAL^{m-} \tag{1.10}$$

During scanning potential, stripping current is generated by the reduction of metal complex, either from the metal or from a reducible group on the ligand. Normally, some ligands include N/O donor groups (*e.g.*, salicylaldoxime, 8-hydroxyquinoline) have aromatic rings, which easily form chelation with metal ions (Ni, Co, V, Al, *etc*.)[62,63]. The ligands should be capable of complexing with metals and highly electroactive when adsorbed on the electrode. Furthermore, the sensitivity of AdSV can be greatly improved by including the catalytic effect. The reduction current of the adsorbed analyte complex is catalytically enhanced by adding an oxidant (*e.g.*, nitrate, bromate, chlorite, and hydrogen ions)[64,65]. The AdSV based on the generation of catalytic current has successfully achieved ultra-trace analysis of inorganic substances, including Co, Se, V, Sn, Se, *etc*[66,67].

1.2.1 Working electrodes for stripping analysis

Analysis result of ASV is highly dependent on chemical and physical properties of WE. Therefore, an enormous amount of effort has been contributed to extend the substance types of WE that can be applied to a wide range detection of metal ions with better sensitivity, and reproducibility.

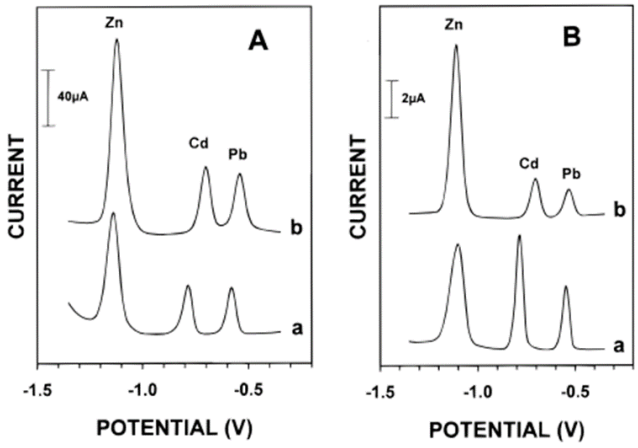

Figure 1.5 Stripping voltammograms of lead, cadmium, and zinc at glassy carbon (A) and carbon fiber (B) electrodes coated with bismuth (a) and mercury (b) films[74].

Bismuth film electrodes (BFEs): To meet the growing requirements for on-site enviromental and clinical trace metal ions analysis, different free-mercury bare electrodes have been developed for SV analysis contaning carbon[69], gold[70], platinum[71], silver[72], iridium[73], *etc*. Though these electrodes have provided useful stripping signal for several metal ions, their performance can't close to that of the Hg based electrodes because of the lower cathodic potantial window, larger background, and easily poison by matrix components. In 2000, Wang's group[74] prepared a bismuth film coated carbon electrode (glassy carbon or carbon fiber as substrate.) that was used for the detection of trace cadmium, zinc and lead combining with ASV method. As shown in **Figure 1.5**, bismuth film coated glass carbon and carbon fiber both disply sharp and seperated peaks. The peak potential of zinc and lead is almost identical with the mercury electrodes, while the cadmium peak exhibits a more negative potential that is beneficial for an addition of a new selective dimension. Subsequent work by Morfobos [68] extended the bismuth film electrodes (BFE) to adsorptive stripping determination of Ni(II) and Co(II). The results indicated BFE have some unique advantages in comparison to MFE, such as greater tolerance for excess Zn interfering ions and insensitivity to dissolved oxygen. In addition, BFE also has other benefits such as a wide cathodic potential range, negligible toxicity compared to that of

the Hg electrodes, reproducible peaks, making it more attractive for a wide range of application. The design of BFE is essential to result of stripping performance. Normally, two methods have been developed for electroplating bismuth film on the substrate (normally glass carbon disk): (1) pre-plating or ex-situ plating, meaning that the Bi (III) ions are firstly electrodeposited on the substrate and then transferred into the sample solution for analysis. (2) in-situ plating, the Bi (III) ions are added in sample solution and then co-deposited with the target heavy metals. The deposition reactions are shown (1) and (2):

$$Bi^{3+}+3e^{-} \rightarrow Bi^{0} \quad (1.11)$$

$$M^{n+}+ne^{-} \rightarrow M(Bi) \quad (1.12)$$

For ex-situ plating, it should be carried out in acidic media to avoid the hydrolyzation of Bi (III) ions in high pH with the potential –0.5 to –1.2 V. Moreover, the convection condition (electrode rotation or stirring solution) is provided for deposition of Bi (III) ions to facilitate accumulation step. In stripping analysis, the BFE could be used for multiple batch measurements of sample. Therefore, to preclude some species remaining on the electrode surface, the electrode must be reactivated after each stripping by imposing an overpotential to decompose any remaining species. Pre-plating is very versatile because of independent control step for bismuth film deposition and sample analysis, but also causes complicated and time-consuming operation. For in-situ plating, the Bi (III) ions concentration is generally higher than the target analytes concentration to avert the saturation effects[75]. In comparison with pre-plating, it could simplify the experiment operation and shorten measurement time because it doesn't need separate bismuth plating step from a Bi (III) solution and electrode transfer from the plating solution to the sample solution. However, the bismuth film will be stripped off from the surface of substrate with target analytes after each stripping analysis at a more positive oxidation than that of bismuth[74,76]. Thus, the substrate surface needs to be redeposited with bismuth film after each stripping analysis for next bath use. In ASV analysis, some surface-active compounds are extremely easily to absorb on the surface of BFE resulting to the surface fouling. To alleviate this problem, different polymers have been modified on the BFT surface as a permselective membrane such as nafion, polypyrrole, poly-(3-methylthiophene), *etc*[77–79]. Overall, bismuth electrodes as an ideal substitute of mercury electrodes, behave attractive peak resolution and lower signal-to-background ratio. Coupling with different surface modifications, it is

attractive for application in a wide field such as clinical, environmental, and industrial applications.

Chemically modified electrodes: WEs surface are coated with a monomolecular, multi-molecular, ionic, or polymeric film, *etc.*, which could alter the properties of interface, called chemically modified electrodes (CME)[80,81]. The aims of CME are to improve selectivity, sensitivity, and stability of electroanalysis method, as well as eliminate interference of some surface-active compounds and expand usable potential window[82]. The popular modifiers on the electrodes include: biomolecules, polymer, ligands, n-Alkanethiols, *etc*. Normally, the methods of modifying the electrode surface are classified as: film–substrate attachment method (*e.g.*, physisorption, chemisorption, covalent attachment)[83–85], and film composition (*e.g.*, clays, sol-gels, polymer, and DNA)[86–89]. In SV analysis, the biomolecules (*e.g.*, microorganisms, cells or parts of cells, cell receptors, enzymes, nucleic acids, antibodies, peptides, *etc*.) are directly or indirectly modified on electrode surface as sensing element for recognizing target analytes, termed "biosensor"[90,91]. Normally, these biomolecules have strong binding affinity with specific metals or proteins. DNA modified electrodes are increasing used to construct electroanalytical sensors in various fields of application, some of their bases could mismatch with specific metal ions or proteins, such as thymine-Hg^{2+}-thymine (T-Hg^{2+}-T) mismatch, cytosine-Ag^{2+}-cytosine (C-Ag^{2+}-C) mismatch, Pb^{2+}-stabilized G-quadruplex, thrombin binding G-quartet conformation, enabling a specific determination of analytes[89,92].

In addition, the conducting polymers modified electrodes have also received an increasing attention due to their superior conductivity, easy for preparation and better adhesion properties[93,94]. Some unmodified conducting polymers such as polypyrrole (PPy), polythiophene, poly(3-methylthiophene) (P3MT), poly(3,4-ethylenedioxythiophene) (PEDOT), polyaniline (PANi), behave intrinsic affinity to metal ions. A lot reports have demonstrated that they could be directly modified on the electrodes surface for preconcentrating metal ions in ASV[95–98]. Besides, the conducting polymers are usually functionalized by doping ligands as ion recognition sites (*e.g.*, metallochromic indicators, neutral carrier, sulfonated macrocycles, charged carriers, *etc.*) to improve the ions selectivity and electron transfer in electrochemical sensors[99–101]. These ligands could be covalently bound with the conducting polymers or they may be entrapped in conducting polymers as doping ions.

The size and shape of working electrode: A conventional WE, the so-called macroelectrode, has a diameter of a few millimeters. Microelectrodes are referred to electrodes with very small dimensions (≤25 μm) in at least one dimension of the electrode geometry. To make a microelectrode, it only needs to be small enough in one dimension, so the electrode can be of various shapes, such as disk, spherical, hemispherical, column microelectrodes, *etc*[102]. Microelectrodes have attracted a great deal of attention in SV analysis, due to their excellent analytical features, such as high mass transport, lower ohmic drop, minimal charging current, *etc*[103–105]. The high mass transfer enhanced by the spherical diffusion reduces the need of convective transport, thus the stirring is unnecessary during the preconcentration step. The smaller charging current is as the result of the small electrode surface area, that significantly increases the ratio of faradic to non-faradic current, and improves the sensitivity of analysis, promoting measurement in microvolumes of sample[106–108]. Moreover, the lower current results in a negligible ohmic drop which is allowed to detect analytes in the high resistance medium without adding the supporting electrolyte. It is possible to detect metal ions in relatively low ionic strength media such as rivers, snows, rains, *etc*. A variety of modified microelectrodes have been widely used to analyze the trace metal ions or organic substances. For example, the bismuth coated on the micro-disk electrodes was applied in the determination of trace heavy metals (Pb, Cd) by ASV in food sample[109]. The gold nanoparticles were modified on the gold microelectrode to effectively reduce the effect of hydrogen overflow on stripping of Zn(II), shifting stripping potential to positive value. However, a drawback for using microelectrode is that the extremely low current values are problematic. An array of microelectrode is developed to address this issue. The microelectrode arrays (MEAs) could facilitate the increase of current magnitude and improvement of signal-to-noise[110,111]. Moreover, the distance and number, geometry of the electrode in MEAs are proved to influence the electrochemical signal in voltametric analysis. Generally, the electrochemical signal increases in proportion to the number of electrodes when MEAs (multiple parallel microelectrodes) have sufficient inter-electrode distance. The MEAs of iridium, gold, platinum, and carbon are commonly manufactured using photolithographic methods or thin film techniques originating in integrated circuit technology, which have been applied the analysis of trace metals in rain water, lake, or soil sample[112,113].

1.2.2 Potential wave forms

The voltametric response for stripping analytes in SV will depend on the selected type of scan, containing linear sweep voltammetry (LSV), differential pulse voltammetry (DPV) *etc*. Linear sweep voltammetry (LSV) is the simplest one of the electrochemical voltametric methods. In LSV, WE potential is swept linearly from one to other values at a fixed scan rate, and current is measured as a function of time. A voltammogram is obtained by plotting the current *vs.* potential from LSV experiment (**Figure1.6A and B**). LSV can be used to obtain the qualitative and quantitative information of electrochemical reaction and to study the electron transfer kinetics of analytes. For example, boron-doped diamond (BDD) electrodes were used by Dragoe group to detect trace levels of lead by linear-sweep anodic stripping voltammetry, which behaved a low limit of detection (2 nM) for lead ions in tap water[114]. Zhang *et al*. used the underpotential method to deposit arsenic (III) on macroelectrode or a Pt nanoparticle modified GCE, and followed by arsenic stripping by means of LSV[115]. The result indicated that this method has practical value for detection of arsenic (III) in drinking water. While it is beneficial for examining the voltammetric behavior of metal deposition and stripping on an electrode surface, the collected current includes faradaic current (from metal stripping) and non-faradaic current (capacitance) in the potential range. The non-faradaic current as a background signal would make interference to whole electrochemical signal, eventually causing the reduction in the sensitivity of analysis, especially for determination of lower concentration analytes.

The waveform in DPV is a series of pulses where a base potential is kept for a specified period before the application of a potential pulse. Current is sampled (time: τ') prior to applying the step pulse. The potential is then stepped by a small amount (10-100 mV) and current is sampled again at the end of the pulse (time: τ). The sampling period is chosen to allow sufficient time for non-faradaic currents to decay, so that the predominant current results from faradaic reactions. The potential of the electrode then steps back by a smaller value than during the forward pulse, so that the baseline potential of each pulse increases a same value throughout the sequence. The differential voltammogram is recorded as the difference between the two sampled currents, $\delta i = i(\tau) - i(\tau')$ plotted against the baseline potential (**Figure1.6C and D**). The differential pulse principle could be explained simply as follows:

$$O + e^- \rightarrow R \text{ (O is reduced in a one electron step)} \qquad (1.13)$$

At the beginning of the experiment, the base potential is much higher than the E' of O (formal potential), no faraday current flows before the pulse, and the potential change during the pulse is too small to stimulate the faraday process, so i(τ) - i(τ′) is actually 0. In the later stage of the experiment, the base potential moved to the diffusion limited current region, and O was reduced at the maximum possible speed during the waiting period, and the current could not be further increased by applying a pulse, and the difference between i(τ) - i(τ′) was very small. Significant differential currents are observed only around E' (for reversible systems).

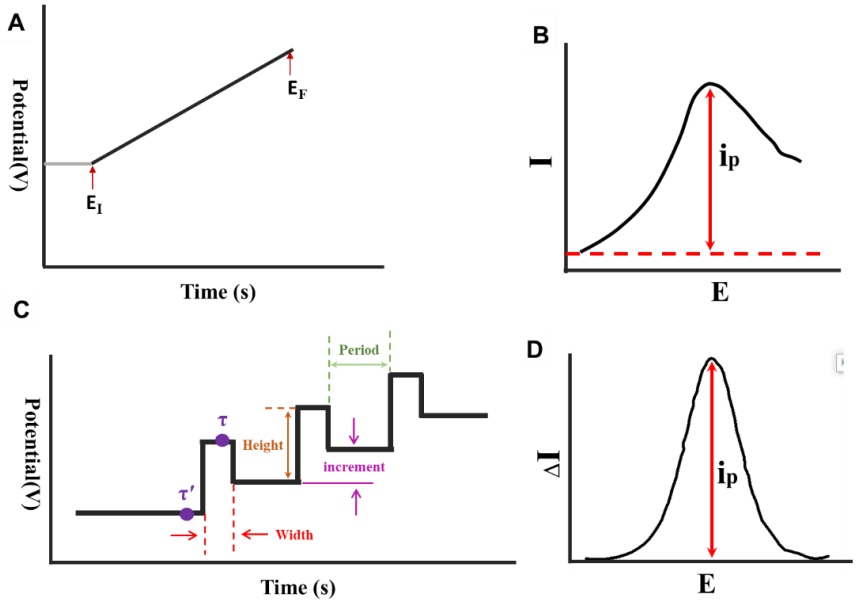

Figure 1.6 (A), (C) the change in potential over time for a digital LSV, DPV, respectively. (B), (D) the current peak for LSV, DPV, respectively. The peak current in D is typically larger than B.

Generally, it is convinced that the difference between the two-sampling current can help to reduce the non-faradaic current, and improve the sensitivity of analysis. Based on this favorable advantage, it is widely applied for determination of various ultra-trace analytes (heavy metal ions, organic molecules) in the environment, food, biomedicine [116–119].

1.2.3 Interferences

There are various interferences for determination of sample types in the SV, which seriously affect the accuracy, selectivity, and sensitivity of the analysis results. The formation of the intermetallic compound (*e.g.,* In−Cd, Cd−Tl) and overlap stripping peaks have made great impact to the determination of target element. For example, Cu(II) as a type of trace metal could be found in different kinds of analytical samples, which is easily co-deposited with other metals on the Hg electrode to form intermetallic compounds. Some reports have proved that the peak current for a fixed concentration of Zn deceased with the addiction of Cu, arising from the formation of intermetallic compound between Cu and Zn[120–122]. The stripping peak current of Cd has also been found to be suppressed due to the presence of Cu, and a significant enhancement for Cu peak. This is due to similar stripping potential between Cu–Cd intermetallic and Cu, which results in two poorly resolved peaks[123,124]. When detecting the Sb(III), the presence of the metal ions (Ag(I), Hg(II),Cu(II), Bi(III)) have gave rise to the overlap stripping with the Sb peak[125]. Some typical methods could eliminate the interference from intermetallic compounds: (1) an additional element is added to the sample solution, and formed a more stable intermetallic compound with non-target metal element. For instance, the addition of excess gallium (Ga) to the Zn solution containing Cu, the formation of intermetallic Cu-Ga could successfully circumvent the Cu-Zn problem[121]. (2) the sample solution could be diluted so that the concentration of interfering ions could be below the detection limit. (3) pre-treatment processes are executed by adding ion exchange resins or interfering ionic complexing agent before SV analysis. For example, the acidic cation-exchange resin (amberlite IR-120) have been used to separate the Pb from other heavy metal ions (Cd(II), Hg(II), Cu(II), Zn(II)) from pharmaceutical formulation[126]. In order to inhibit interference of Cu(II), ferrocyanide was used to form complexation with Cu(II) prior to the analysis of Cd(II) and Pb(II) in soil samples[127]. As well, the sodium oxalate was as a masking agent to mask the interfered metal ions (Cu(II), Bi(III), Pb(II) and As(III)), and the KSCN was used to remove the interferences from Ag(I) and Hg(II)[125]. Additionally, the application of chemically modified electrodes may lessen intermetallic interferences when stripping voltammetry is performed due to the selective interaction between the modifiers and metal of interest[128]. The processes of interaction generally include covalent binding, biomolecular specific recognition, complexation, *etc*.[129]. The overlap peaks of multiple analyte metals, in some cases, can be resolved by adding

suitable complexing agents to sample solution so that the stripping potential can be shifted according to how stable the complexes are.

When metal ions are detected in real samples, dissolved organic compounds such as proteins, surfactants, and bacteria are extremely easily absorbed on the electrode surface to create unpredictable errors in the analysis result of SV. The CSV and AdSV have often been adversely affected by organic compounds, due to the competition between the ligand and the organic compounds for complexing with target metals. In turn, besides the target metal, other interfered metals could compete with the ligand to form complexes. The surfactant such as Triton X-305 have been reported to interfere by hindering adsorption of the Cu–adenine complex on the electrode for determination of Cu(II) by ASV[130]. The presence of Ta(V), As(III), Pb(II) could depress the peak current of Sb due to the competitive accumulation with Poly(pyrogallol) film modified on the WE[125]. Therefore, great care must be paid in removing or destroying the organic compounds prior to the detection of target analytes in real sample. At present, the common methods to eliminate interference of organic compounds include acidification, microwave heating, and UV irradiation, *etc.*[131–133]. Moreover, the test samples containing low mounts of organic compounds, could be corrected by the standard addition method and thereby mitigating the interference of organic matters to analysis result[134]. Among them, UV digestion is one of the most convenient and efficient methods, and is widely used in the pretreatment of the acidified samples solution. UV-irradiated water can produce highly oxidative hydroxyl radicals (HO·), which can oxidize most organic compounds by destroying chemical bonds in compounds (the hydrogen peroxide acts as an oxidant to assist in the breakdown of organic matter), so that organic molecules eventually become CO_2 and H_2O, thereby eliminating the binding ability between organic compounds with heavy metals, and improving the sensitivity and accuracy of detection of analytes[135–137].The inorganic anions (Cl^-, Br^-, $C_2O_4^{2-}$, SCN^-, *etc.*) normally also complex with metal ions which cause interference for the determination of metal ions in SV analysis[138]. Additionally, some electroactive non-metallic species (dissolved oxygen, nitrates) could generate electrochemical signal that might interfere the stripping signal. Thus, it is essential to clearly know the solution composition before detecting metal ions in sample solution.

1.2.4 Summary of stripping voltammetry

The stripping voltammetry originates from the analysis of heavy metal ions, where a pre-concentration is achieved by electrodeposition on the WE and then the quantity of electrodeposited metal is analyzed by the charge in anodic dissolution and can be related to the metal ions concentration in solution [139–141]. The pre-concentration can also be carried out based on electrostatic interactions or chemical adsorption between the analyte and the WE, which extends the applications also to non-metal species[142,143]. As the key to the method is on the pre-concentration, enormous effort has been made to push the lower detection limit by chemically modifying the WE to enhance the interactions with the analyte (*e.g.,* via electrostatic interactions, complex formation, specific molecular recognition, or formation of sparingly-soluble species) [144–147]. A prerequisite to ensure high sensitivity is also that the accumulated species must be electrochemically accessible, in a fast and quantitative way, which might be intricate in some cases (electrode modifiers based on molecularly imprinted polymers, for instance)[148,149]. So far, anodic, cathodic and adsorptive/extractive stripping voltammetry remain among the analytical standards for the detection of trace elements and organic substances in the environment or in industrial samples belonging to food or pharmaceuticals sectors[25,32–35].

However, it is only applicable to the analytes that can be deposited or adsorbed onto, or have strong interactions with, the (modified) WE. A question then arises: How to extend the strategy (one uses longer time to cumulate analyte on the electrode and then analyzes in a striping step) of stripping to the analytes that do not pre-concentrate on WE?

1.3 The study of local reactivity based on imaging techniques

Apart from the concentration of analyte, another main target of electroanalytical chemistry is the reactivity of electrochemical interfaces. In general, the relationship between the applied potential and the current response on electrodes was used for studying the charge transfer kinetics, which could date back from Tafel. Various electrochemical measurements have been developed for this purpose, such as cyclic voltammetry and electrochemical impedance spectroscopy. These measurements may reveal the reactivity of electrodes.

Complement to the global reactivity of electrode, the local reactivity and its distribution over the electrode surface are also highly interesting, notably for studying electrode materials at micro- and nanoscale, as well as for their engineering at device level. The local reactivity of electrodes is generally measured through two strategies: scanning probe approaches and optical imaging. The former is based on scanning a probe that is in contact or close to the sample surface and measuring signals from the probe. This includes scanning electrochemical microscopy (SECM), scanning ion conductance microscopy (SICM) and scanning electrochemical cell microscopy (SECCM)[152–154]. These methods may reach high spatial resolution in nanometer range by scanning the probe from one point to another point. On the other hand, optical imaging may offer much higher throughput by directly mapping the surface[155]. A common way is to design reactions that may induce optical change of the WE, such as surface plasmon resonance[156], electrochemiluminescence[157], fluorescence and other imaging based on microscopy[158]. They may offer a balanced spatial and temporal resolution in mapping. In this section, both the two strategies are introduced.

1.3.1 Scanning electrochemical microscopy (SECM) and related techniques

SECM is a scanning probe technique in which a microelectrode is scanned across the substance from one point to another point to obtain the surface topography and local electrochemical activity of the sample substrate by recording the current response. Thus, by using a variety of operating modes, it is possible to characterize different substrates and experimental systems. This technique is capable of investigating the local electrochemical reactivity from a surface at a high spatial resolution [159–161].

Basically, SECM is equipped with a bipotentiostat that controls the potential of the probe and the substrate immersed in the electrolyte, a position controller that accurately controls the movement of the probe, a micro- or nanoscale probe, and a data acquisition system that synchronizes all the components (**Figure 1.7**). In SECM measurements, different operational modes have been developed for a variety of applications, including feedback mode, generation/collection modes, redox competition mode, direct mode, potentiometric mode[40,162–165]. In order to expand the scope of application of SECM, SECM instrumentation has been combined with several different techniques containing scanning force microscopy (SFM)[166], scanning probe lithography

(SPL)[167], surface plasmon resonance (SPR)[168], scanning ion conductance (SICM)[169], and fluorescence microscopy[170], *etc*. On the other hand, scanning electrochemical cell microscopy (SECCM) was also reported recently by Unwin et al. by fabricating a "quad probe" combined the SECM technique[171].

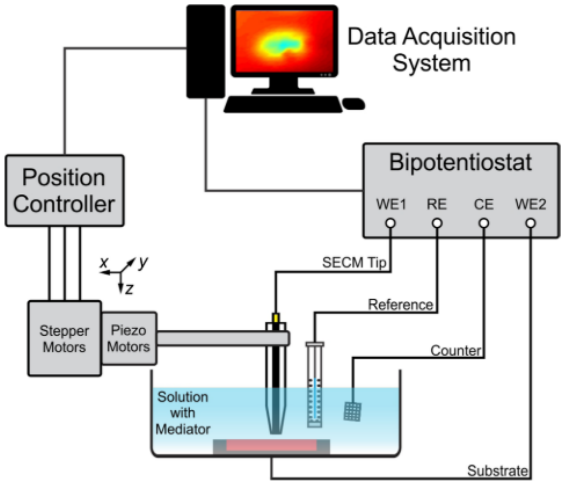

Figure 1.7 Schematic of a SECM instrument[40].

The probe plays an essential role in the SECM experiment, which directly determines spatial resolution of a SECM measurement[172–174]. It is usually a microdisk electrode, in which an electroactive core (*e.g.*, gold, silver, platinum, carbon) is covered by an insulating shield (*e.g.*, glass)[172–174] with different geometry [175–179]. Taking reduction reaction as example, the oxidant (*Ox*) in solution will be reduced at the microelectrode disk surface (**Figure 1.8A**).

$$Ox + ne \rightarrow Red \tag{1.14}$$

When the tip-to-substrate distance (d) of the probe is more than 10 times the radius (a) of the electroactive core ($d > 10a$), the probe has a steady-state current ($i_{T,\infty}$) which is controlled by the mass transfer of *Ox*:

$$i_{T,\infty} = 4nFCDa \tag{1.15}$$

where F is Faraday's constant, C is the concentration of *Ox* in solution, D is the diffusion coefficient, and a is the diameter of the microelectrode.

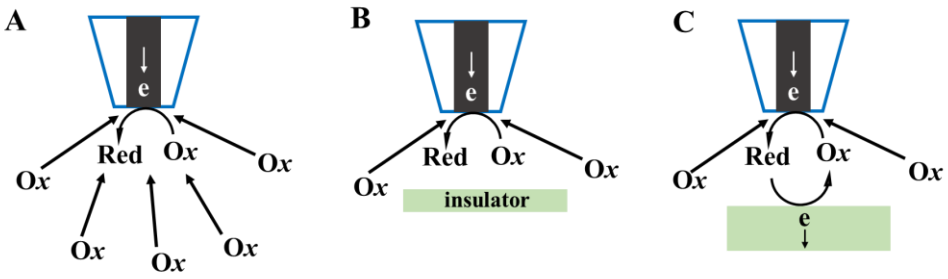

Figure 1.8 Schematic of SECM operational modes. (A) Steady-state behavior (diffusion-limited) in bulk solution. (B) Feedback mode over an insulator substrate (negative feedback). (C) Feedback mode over a conducting substrate (positive feedback)[180].

The difference comes when the probe gets close to a sample. Two scenarios can be envisaged: (1) The sample is inert to the redox reaction. The diffusion of *Ox* to the probe is then partially inhibited, resulting in a decrease in the current response $i_T < i_{T,\infty}$ (**Figure 1.8B**). This is called negative feedback, which applies to most of insulating samples without special redox functionalization. (2) The sample is active for the regeneration of *Ox* (**Figure 1.8C)**. This yields an increase in current $i_T > i_{T,\infty}$, which is called positive feedback. In positive feedback, the probe current is a function of tip-substrate distance *d* and the kinetics of regeneration of *Ox* on the substrate. Therefore, if *d* is known and controlled, the redox reactivity of the substrate can be determined. By scanning the probe in x-y plane and plotting i_T, the SECM image can be obtained. **Figure 1.9 A** illustrates imaging of a Pt interdigitated array electrode (IDA) by using the constant distance regulation of SECM/SICM[181]. The tip-substrate distance was controlled by SICM, and the SECM probe current increased as the probe was moved above the Pt IDA because of positive feedback. The SECM-AFM was used for elucidation of local electrochemical phenomena of the Li-S electrode with spatial resolution at nanoscale characterize[166]. As shown in **Figure 1.9B**, redox competition mode was used to determine the oxidation reaction of Li_2S_6 on Pt nanoparticles (NPs) modified carbon surface. In comparison to other areas of the surface, the tip current (at 2.6 V vs. Li/Li^+) over Pt nanoparticle decreased as applying a potential on the substrate due to the depletion of Li_2S_6 oxidation on the tip. The imaging may differentiate electrochemically active and inactive regions, although the sample is electrically conductive everywhere.

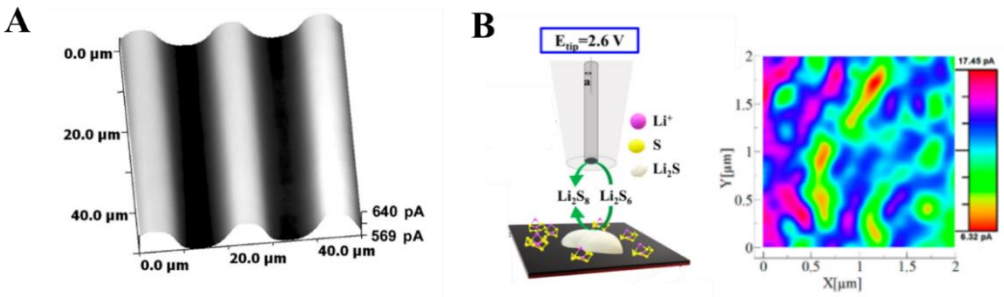

Figure 1.9 (A) SECM image of a Pt band microarray in 0.50 mM $FcCH_2OH$ + 0.1 M KCl[181]. (B) SECM current images recorded by the substrate at 2.6 V[166].

1.3.2 Surface plasmon resonance microscopy(SPRM)

The SPRM was originated from surface plasmon resonance (SPR) spectroscopy, which has been extensively used to study biomolecular binding kinetics. SPR phenomenon occurs when a beam of p-polarized light is irradiated on a metal film (*e.g.* Au, Ag, Cu) coated on the surface of the substrate at a certain angle through the prism, resulting in the collective oscillations of free electrons at the metal-dielectric interface. The surface electromagnetic waves (surface plasmon polaritons, SPP) generated by collective oscillations will propagate parallel to the metal-dielectric interface and form an evanescent wave, whose electric field intensity will decay exponentially. In the visible light range, the effective depth of the evanescent wave is generally 100-200 nm from the surface. As a result, the intensity of the reflected light is minimized due to the conversion of light energy into plasmon resonance at a certain SPR angle. This angle is very sensitive to the refractive index close to the metal-dielectric interface, and may differentiate small differences or changes. Based on this, the SPR have been commercialized and developed as a label-free optical detection technique that can be used to analyze binding interactions between two or more molecules in real time. Moreover, the highly flexibility and sensitivity of the SPR technique enables researchers to characterize biomolecular interactions in binding studies and is widely applicable to a variety of molecules such as ions, molecular fragments, small molecules, proteins, viruses, *etc.*[182,183]. SPR technology also been used to provide biophysical data such as affinity, kinetics, thermodynamics, *etc.*[184,185].

To achieve high throughput screening, a digital camera is applied to acquire image, which enables the SPR technique to have high spatial resolution or imaging capability. In addition, a high numerical aperture (NA) objective has been used in place of the

prism, which allows SPRM to detect objects with a high spatial resolution and prevent image distortion. In SPRM, the optical system includes a laser source, an inverted microscope, and a charge-coupled device (CCD) camera. A beam of p-polarized monochromatic light is focused by the oil emersion objective and stroked to a gold film coated substance (coverslip) to generate SPPs relying on a total internal reflection (**Figure 1.10A**), then the intensity of reflected light is captured by the CCD camera when the incident angle of the light is controlled. The incident angle or SPR angle is given by the equation[186,187]:

$$\mathrm{Sin}(\theta_R)=\sqrt{\frac{\varepsilon_m\varepsilon_s}{(\varepsilon_m+\varepsilon_s)\varepsilon_g}} \qquad (1.16)$$

Where θ_R is the incident angle to excite the surface plasmon resonance in Kretschmann configuration[187], ε_m, ε_s, ε_g is the dielectric constant of the metal film (real part), sample, and the objective, respectively.

A change in the dielectric permittivity of samples in touch with a metal film will affect the surface plasma. When the refractive index of a sample region happens to change, the θ_R will change, as the permittivity of the dielectric is proportional to the square of the refractive index of the sample. Scanning the incident angle of the light beam in a specific range will reveal a distinct minimum in reflectivity at a discrete angle (**Figure 1.10B**). As a result, the reflection attenuation from the metal film is at its maximum at a specific incident angle when given a specific set of dielectric constants. It can be clearly seen that the θ_R shift to a higher angle with increasing the refractive index of sample region[188].

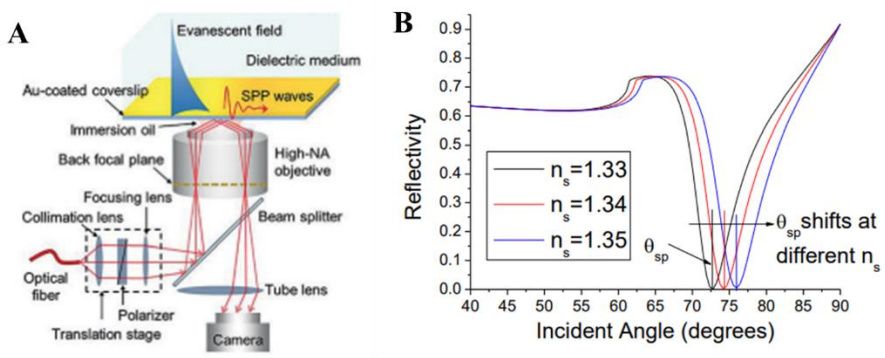

Figure 1.10 (A) Schematic of SPRM[187]. (B) SPR curves[188]. Different refractive index has different resonance angle.

The SPR change originated from adsorption of species on WE may also be induced and modulated by electrochemical reactions [189–193]. This compatibility is called

electrochemical surface plasmon resonance microscopy (EC-SPRM), which has been widely employed for studying local electrochemical reactions in the various fields such as energy storages[194], catalysis[195], biomolecules[196], *etc.* Note that EC-SPRM is also sometimes referred with different terminology, such as plasmonic-based electrochemical current microscopy (P-ECM) and plasmonic-based electrochemical impedance microscopy (P-EIM).

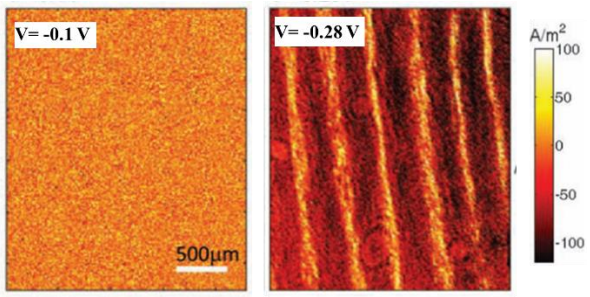

Figure 1.11 (A) Electrochemical current density images of a fingerprint at -0.1V and-0.28V, respectively[189].

The SPR signal change may reveal the surface concentration of redox active species, which can be linked to the local current density by the flux (Fick's First Law) [197]. Shan *et al.* [189]reported a new analysis method to image the variation of local current on the WE under voltammetry based on the SPRM. The current density, $i(t)$ could be calculated by the local SPR signal according to the equation (1.17)**:**

$$i(t)=bnFL^{-1}\left[s^{\frac{1}{2}}\Delta\theta_{SPR}(s)\right] \qquad (1.17)$$

Where $b= [B\ (a_R D_R^{-1/2} - a_o D_O^{-1/2})]$, n is the number of electrons involved in the redox reaction, F is the Faraday constant, L^{-1} is the inverse Laplace transform, and $\Delta\theta_{SPR}$ (s) is the Laplace transform of the SPR signal. The a_O and a_R are the changes in the local refractive indices per unit concentration for the oxidized and reduced molecules, D_O and D_R are the diffusion coefficients of the oxidized and reduced molecules, B is the calibration factor.

Technically, the fingerprint with secretions was touched on Au film electrode, and then the local current of the electrode was mapped by scanning the potential in 10 mM $Ru(NH_3)_6^{3+}$ solution. As shown in the **Figure 1.11**, the fingerprint could be seen clearly in regions without covering with secretions at -0.28V compared to that of -0.1V due to the reduction of $Ru(NH3)_6^{3+}$ at a maximum current.

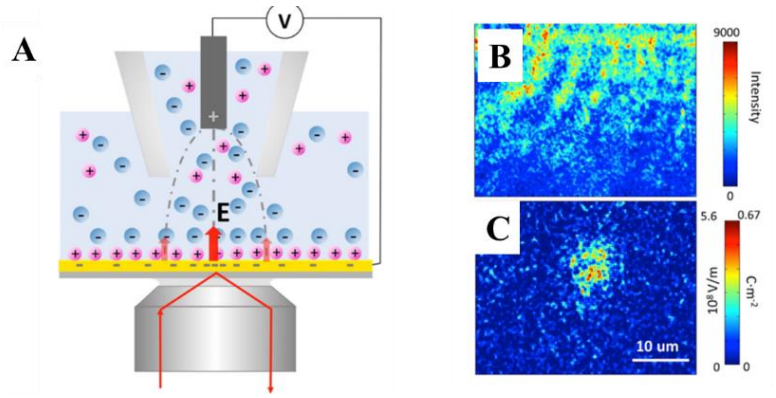

Figure 1.12 (A) Schematic of the setup for detecting local electric field by P-EIM. (B) dc and (C) ac amplitude images of a 6.3 μm-diameter pipet induced surface charge distribution on Au electrode[190].

The SPR signals may also be linked to other interfacial properties of the electrode/electrolyte interface, such as surface charge, electric field, and potential. The change of dielectric constant of the metal film (ε_m) is decided from the surface charge density according to the Drude model[198]:

$$\varepsilon_m(f)=1-\frac{n_e e^2}{\varepsilon_0 m_e 4\pi^2 f^2} \quad (1.18)$$

Where e, m_e, n_e are the charge, mass, electron density, respectively. $\varepsilon_0=8.85\times10^{-12}$ F/m (vacuum permittivity), f represents the surface plasmon frequency. Considering the thickness of gold film is d_m, the change of electron density leads to the surface charging ($\Delta\sigma$), given by the equation[199]:

$$\Delta\sigma= -ed_m\Delta n_e \quad (1.19)$$

Combining equation (1.18) with (1.19), the relationship between the change of dielectric constant and the surface charging could be calculated:

$$\Delta\sigma= -\frac{ed_m n_e}{\varepsilon_m-1}\Delta\varepsilon_m \quad (1.20)$$

Therefore, the relationship between the change in the surface charge ($\Delta\sigma$) and the resonance angle shift ($\Delta\theta_R$) can be found by combining equations (1.19), (1.20) and (1.16):

$$\Delta\sigma= \alpha\,\Delta\theta_R \quad (1.21)$$

Where α is constant that can be calculated theoretically or calibrated experimentally. According to the relationship above, Wang *et al*. demonstrated that the P-EIM could determine the distribution of surface charges and local electric fields on the electrode

surface in combination with a micro-pipet (**Figure 1.12A**)[190]. When the micro-pipet was placed near an electrode, an oscillating potential was applied, which induced charge on its surface, resulting in both dc and ac plasmonic images (**Figure1.12B and 1.12C**). By detecting the scattering of plasmonic waves by the micro-pipet, the former provides information about the position and size of the micro-pipet tip, while the latter offers information about the distribution of surface charges, from which the electric field (E_{ls}) on the gold surface could be calculated according to the equation:

$$E_{ls} = \frac{\sigma}{\varepsilon\, \varepsilon_0} \tag{1.22}$$

The results indicated that the distance between micro-pipet and gold electrode, as well as size of the orifice of the micro-pipet directly decide local charge density and electric field. In addition, considering that SPRM is sensitive to local electron density on the gold film electrode, which could be modulated by altering interfacial potential. It thus can also be used for studying distributions of interfacial potential and provides a way to image the distribution of interfacial potential of bipolar electrodes in non-faradaic conditions without using any additional active probes in the solution[200].

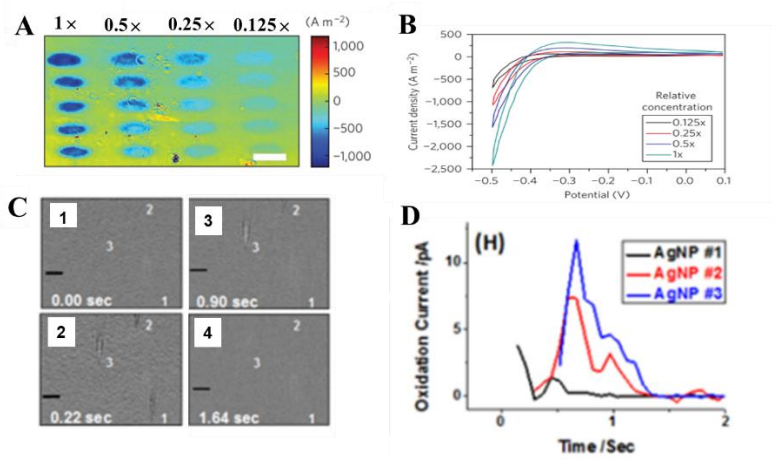

Figure 1.13 (A) P-ECM image of the platinum microarray with different surface densities, at V= -0.5 V. (B) CVs of four different surface densities shown in (A) [202]. (C) Snapshots of plasmonic images of three individual Ag nanoparticles during a typical collision-oxidation process. (D) Transient electrochemical current of the Ag nanoparticles obtained from the plasmonic image intensity, the Ag nanoparticles marked in Figure C[201].

It has been shown that each nanoparticle has different electrochemical properties based on its size, shape, composition, and surface states[201]. Conventional EC methods for

studying single entity is to measure the average value of a large number of particles. However, most actual systems usually contain heterogeneous components, for example, nanoparticles of different sizes and shapes. In order to investigate the electrochemical properties of various entity simultaneously, EC-SPRM has received great attention due to its high throughput and high spatial and temporal resolution and its potential to study the electrochemical process of a single entity. Shan *et al*.[202] studied the electrocatalytic activities of individual platinum nanoparticles by using the P-ECM technique. In this work, an array of platinum nanoparticles printed on gold film electrode surface as catalyst, which could catalyze the reduction of protons to hydrogen in the H_2SO_4 solution by scanning a negative potential. The refractive index near the electrode surface was decreased during the reduction process which resulted in the change of SPR signal. Therefore, electrochemical current of the multiple platinum nanoparticles could be simultaneously imaged corresponding to the applied potential. In order to demonstrate the capability of P-ECM for quantitative analysis of the local electrocatalysis reaction, platinum nanoparticles of varying densities were printed on the gold electrode to catalyze the proton reduction. The results exhibited the electrocatalytic current increases proportionately to the nanoparticle density at a given potential (**Figure 1.13A and 1.13B**). Moreover, the differences between single Au NWs and bulk Au electrodes also have been studied by P-ECM images and CVs. Discerning the composition, structure and size of single particle is very essential, especially the material applied in the lithium battery. The small size of the nanoparticle is capable of a faster charge rate and long cycle life in Li-ion batteries due to the acceleration of Li-ion diffusion and decreasing stress during phase transition[203,204]. Besides studying the electrochemical reaction of nanoparticles pre-immobilized on the electrode surface, the P-ECM can also be used to study the dynamic electrochemical activity of mobile single particles during collision on the electrode surface. The transient oxidation reaction deriving from the collision of single Ag nanoparticles with the gold electrode has been studied by Fang *et al*. based on P-ECM[201]. Different Ag NPs could occur to random collisions with gold electrode by applying a potential larger than the oxidation potential of Ag NPs, eventually causing the oxidation of Ag NPs (**Figure 1.13C**). The intensity of imaging decreased over time during the oxidation process due to the shrink of Ag NPs size, meaning the image intensity was directly associated with oxidation current. Thus, the oxidation current of individual Ag NPs could be mapped simultaneously by converting from the image intensity (**Figure 1.13**

D). By studying the collision and oxidation process of three different size of Ag NPs at a fixed potential, SPR image intensity clearly demonstrates that nanoparticle size information can be obtained from the image intensity of nanoparticles, thereby allowing analysis of size-dependent electrochemical activity of nanoparticles.

1.3.3 Electrochemiluminescence Microscopy(ECLM)

Electrochemiluminescence microscopy (ECLM) technique is an essential analysis method which has been applied to study electrochemical reaction kinetics at a micro-nano level due to its outstanding characteristics such as high spatial and temporal resolution, as well as high-throughput, *etc*.[205,206]. In contrast to other imaging microscopes, the imaging approach does not require an optical excitation, so there is no background noise involved, leading to a low detection limit and high sensitivity[207]. Consequently, in this section, the ECL system and mechanism, ECLM setup, and ECLM application will be discussed, respectively.

ECL occurs when excited states are formed by electron transfer of active intermediates resulting from electrochemical reactions. The basic mechanisms of ECL are annihilation and co-reactant pathways[208]. In the annihilation route, the oxidized and reduced species ($A^{\cdot+}$ and $B^{\cdot+}$) are produced on the electrode surface, then these species interact each other to generate excited of luminophore A*, which can emit light by relaxing to the ground state[209].

$$A - e \rightarrow A^{\cdot+} \quad (1.23)$$

$$B + e \rightarrow B^{\cdot-} \quad (1.24)$$

$$A^{\cdot+} + B^{\cdot-} \rightarrow A^{*} + B \quad (1.25)$$

$$A^{*} \rightarrow A + hv \quad (1.26)$$

The annihilation pathway emits photons by relying on simple reaction conditions containing electrochemiluminescent species, supporting electrolyte, and solvent, However, the narrow redox potential range of water makes it difficult for the luminophore reagent to be both reduced and oxidized, this makes it necessary to shift for non-aqueous solvents.

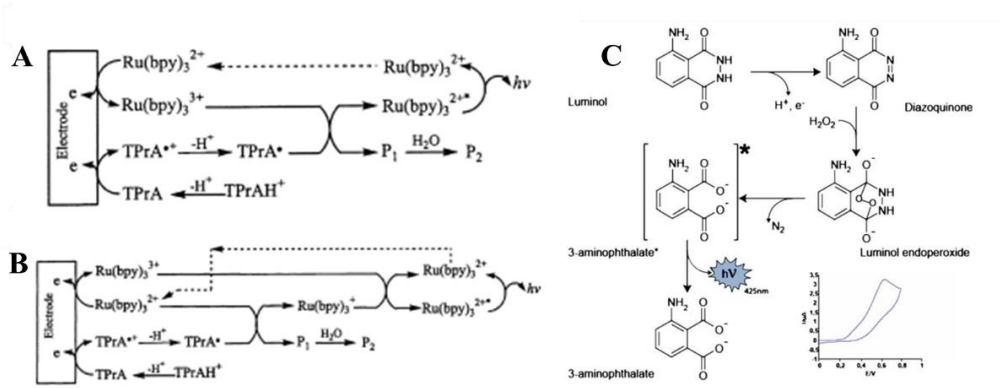

Figure 1.14 (A) and (B) Two main ECL mechanisms involved in $Ru(bpy)_3^{2+}$ /TPrA system[213]. (C) ECL generation by luminol and H_2O_2[214].

It is very easy to generate ECL by the co-reactant pathway, requiring just anodic or cathodic potential sweeps in a solution containing the luminophore and sacrificial co-reactant. The tris(2,2'-bipydidyl)ruthenium(II) ($Ru(bpy)_3^{2+}$), is commonly used as luminophores due to its extremely strong ECL in aqueous solution. The co-reactants need to undergo electrochemical oxidation or reduction to produce free radical ions with high redox ability, thus these radicals can react with the oxidation state or reduction state of the luminophore to form an excited state. Commonly used co-reactants include tri-n-propylamine (TPrA), 2-(dibutylamino)ethanol (DBAE), benzoyl peroxide (BPO) [210–212], *etc*. Then the light emission depends on how $Ru(bpy)_3^{2+}$ is oxidized. For example, $Ru(bpy)_3^{2+}$and TPrA are directly oxidized on the electrode surface to generate $Ru(bpy)_3^{3+}$ and radical cation ($TPrA^{\cdot+}$). The $TPrA^{\cdot+}$ is then deprotonated into the reductive radical ($TPrA^{\cdot}$), which is used to reduce $Ru(bpy)_3^{3+}$ to produce the excited state of $Ru(bpy)_3^{2+}$*, emitting light (**Figure 1.14A**). For the second revisited route (**Figure1.14B**), only TPrA is oxidized at lower potential to form $TPrA^{\cdot+}$, which can reduce the $Ru(bpy)_3^{2+}$ to generate $Ru(bpy)_3^{+}$ by diffusion after deprotonation. The $Ru(bpy)_3^{+}$ can react with $TPrA^{\cdot+}$ to form $Ru(bpy)_3^{2+}$*[213]. Besides electron-transfer reactions, bond-breaking reactions or atom transfers can produce excited states. For example, luminol or its derivatives via O-O bond cleavage to generate excited state in the presence of H_2O_2(**Figure1.14C**)[214].

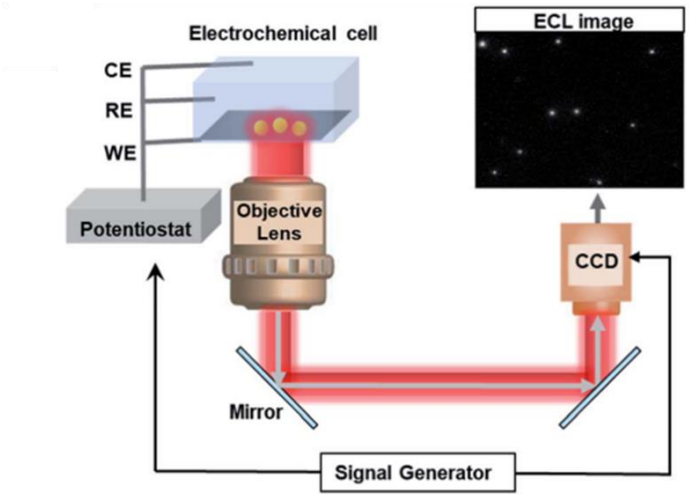

Figure 1.15 An ECL microscopy system for measurement of nanoparticles[215].

ECLM devices consist of electrochemical cell, an objective, potentiostat, and a charge-coupled device (CCD) camera (**Figure 1.15**)[215]. The potentiostat and CCD camera could be synchronized using a signal generator. An electrochemical reaction is triggered by applying a potential step or cyclic voltammetry in a dark box, while a CCD captures the ECL image in real-time. ECL imaging system mainly uses two types of structures: inverted microscope and upright microscope. For inverted microscope, a wide range of objectives (dry, water immersion and oil immersion objectives) can be used, and switching objectives of different magnifications and numerical apertures is straightforward due to the separation from the electrolyte. However, most ECL luminophores have low ECL efficiency. The result is that, when ECL emission passes through the electrode substrate, there will be a light loss due to light reflection at the two-phase interfaces. In comparison with the inverted microscopy, the upright microscopy could achieve high ECL collection efficiency by using water-immersed objective especially for most nano-emitters with weaker ECL emission.

Recently, there is growing interest in developing ECL imaging of single micro/nano entities (*e.g.*, nanoparticles, cell). The nanoparticles with diameters from tens to hundreds of nanometers, such as precious metals, semiconductors, polymer nanomaterials, can be traced simultaneously with high spatial resolution through ECL microscopic methods. In addition, local redox activities, catalytic reactions, cellular processes are all available from ECL measurements[216,217]. By studying how shape, size, and composition of individual nanoparticles influence electrochemical activity at the nanoscale, ECL microscopy can provide a rapid and robust method. Wilson *et al*.

imaged ECL generated from the single gold nanowires, which allows direct reading of electrochemical activity on individual nanoparticle electrodes in a massively parallel fashion without external illumination. The commercial nanowires covered a surfactant layer that hindered the generation of ECL. By removing the ligand, the ECL intensity could be significantly enhanced from exposed gold nanowires surface contrast to the ITO substrate[217]. However, the ECL signal gradually diminished due to formation of a gold surface oxide resulting to the electrochemically inactive of nanowires during scanning the successive cyclic voltammetry. To address this issue, the polymer film (PEDOT:PSS) was covered on the surface of nanowires by drop casting to avoid the oxidation or electrochemical damage of nanowires. Moreover, the anionic polymer PSS in the polymer film could interact with the cationic $Ru(bpy)_3^{2+}$ molecules by pre-loading, producing a brighter ECL emission of gold nanowires than without the polymer film.

Electrochemical reactions can be enhanced by using noble metal nanoparticle catalysts. Therefore, understanding the relationship between particle structure and reactivity is critical to achieving higher electrocatalysis efficiency. Zhu *et al*. used ECL imaging to explore the catalytic active of luminophore at Au-Pt Janus nanoparticles. In comparation with monumental, Janus particle structure exhibited enhanced ECL intensity and stability, demonstrating better catalytic efficiency. This was due to the difference of electron transfer rate constants in asymmetric bimetallic interface, resulting in the concentration gradient and a fluid slip around particles, which eventually enhanced the local redox reactions and reduced the formation of oxide layer at particles[218]. Furthermore, the catalytic active from different sub-particle regions of ZnO crystals had also been explored by Chen *et al*. via ECL imaging. In this work, the synthesized ZnO crystals with various exposed facet which was related to the electrocatalytic performance for degradation of luminol analogue. The theoretical computation and electrochemical experiments both confirmed that the ZnO (002) facet has superior catalytic performance contrast to the ZnO (100) facet, due to the more suitable adsorption energy of O_2, leading to the favorable ECL reaction in (002) facet[157](**Figure 1.16**).

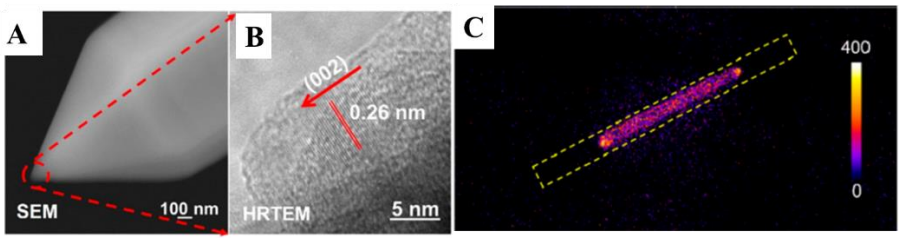

Figure 1.16 (A) SEM image of ZnO rod. (B) HRTEM images for the tip the ZnO rod. (C) ECL image of part ZnO rod[157].

1.3.4 Summary of different imaging techniques for local reactivity analysis

Measuring local electrochemical reactivity of electrodes is highly important for fundamental understanding of the materials as well as engineering of electrochemical devices[219–223]. This is usually achieved by scanning electrochemical probe techniques, such as SECM and SECCM. With the recent development of nanoelectrodes and nano-capillaries, the spatial resolution of SECM and SECCM could reach tens of nanometers. However, to generate a map of electrochemical signals, the probe has to scan over the sample surface, which is intrinsically slow. It may take minutes and even hours, making it impossible to map transient electrochemical processes at high temporal resolution.

On the other hand, optical imaging is much faster with modern cameras. Even without special camera, it typically takes tens of milliseconds to acquire a static image, which is already several orders of magnitude less as compared with scanning probe techniques. Moreover, one may easily achieve good spatial resolution up to the diffraction limit of the light (<1 μm) without special optics. Thus, optical imaging is ideal for high throughput measurements and is widely used in industry [158,224]. Nevertheless, most of the electrochemical reactions cannot be directly "seen". It is essential to quantitatively convert the electrochemical reactions to measurable optical signals. For example, Tao and co-workers have developed electrochemical Surface Plasmon Resonance Microscopy (SPRM), where they derived quantitative links between SPR intensity and local electrochemical signals, *i.e.* current density, double-layer capacitance and charge transfer resistance[225,226]. The technique has been used to monitor the electrocatalytical activity of single nanoparticles in real-time [201][191,192,227]. Note that SPRM is usually performed on thin gold film electrodes

for the sake of getting significant SPR signals. This would limit practical applications due to the potential interference from the oxidation of gold under anodic bias and/or the instability of gold films in acidic media. Another strategy is to “look” at reactions that involve photo-responsive molecules, such as electrochemiluminescence microscopy[231–233]. This is based on the excitation of luminophore that emits light[231]. In this case, the optical signal intensity is linked to the quantity of electrochemically generated photo-active species, which reflects the electrochemical reaction kinetics on the WE. Yet, it is limited to a few special reactions. To target more general “invisible” reactions, one needs to add luminophore and design special reaction routes. This would inevitably change the target system of interest. From the optical measurement aspect, all the approaches above focus on the WE sample, that is, capturing the image by directly “looking” at the optical change of WE as a result of electrochemical reactions. In that case, we need to ask: is there a generic method to in situ observe and record the electrochemical reactivity of any electrode without special design or modification of either the electrode or the electrolyte?

1.4 Electrochromic material

Electrochromism (EC) refers to color change of materials induced by reduction (gain of electrons) or oxidation (loss of electrons) following the current flow [232,233]. According to the process of color change, it can be divided into irreversible color-changing materials with unidirectional color change, and reversible color-changing materials with more application value that can change color in both directions. In terms of its application within a variety of technical systems, EC is of interest from both a scientific and technological standpoint, including for the creation of energy-efficient electronic devices, such as smart windows, displays, shutters, variable reflectors, and sensors[234–238].

The optical properties (transmittance, color) of EC materials change upon oxidation and/or reduction. As a result of switching between oxidation and reduction states, color is formed which leads to formation of new spectral peaks in the visible area. Most organic EC materials are composed of viologens, conjugated conductive polymers (CP) such as polypyrrole, polythiophene, polyaniline and their derivatives[239–241]. Inorganic electrochromic materials mainly refer to oxides, complexes, hydrates and heteropoly acids of certain transition metals[242,243]. Among common transition metal

oxide electrochromic materials, cathodic coloration is mainly found in group VI metal oxides, including tungsten oxide, molybdenum oxide, *etc*.[244,245]; the anodic discoloration is mainly found in VIII metal oxides, such as platinum, iridium, osmium, *etc*., among which tungsten and vanadium oxides are commonly used[246]. A detailed discussion of some commonly used EC follows.

1.4.1 Electrochromism in conjugated conductive polymers

The CPs normally behave deeply colored in the neutral state owing to their π-conjugation. The bleaching process occurs upon oxidizing by losing one or two electrons, which causes the absorption transfer from visible to near-infrared range. CPs have positive charge carriers and counter anions to maintain charge balance (p-type doping) in the conducting oxidation state. Reproduction of the neutral-colored state can be achieved by transferring ions into the electrolyte through reduction reaction, which called cathodically coloring eletrochromism[247]. The reversible coloration reaction is expressed in equation (1.27).

$$(\text{Pol})\ (\text{colored}) + (A^-)_s \leftrightarrow (Pol^+A^-)_{pol}\ (\text{colorless}) + e^- \quad (1.27)$$

When the CPs are colored from colorless along with oxidation reaction, this reaction is called anodically coloring electrochromism[247]. The colorless CPs in neutral state could absorb the UV range, as a result of oxidation, they redshift to the visible spectrum, resulting in coloring, as shown in equation (1.28).

$$(\text{Pol})\ (\text{colorless}) + (A^-)_s \leftrightarrow (Pol^+A^-)_{pol}\ (\text{colored}) + e^- \quad (1.28)$$

Due to the fact that the color of a CP is determined by the optical bandgap (E_g), that is, by the energy difference between the highest-occupied and lowest-unoccupied molecular orbitals (HOMO and LUMO). The E_g is therefore one of the most important parameters for color switching. Any modification to the CPs will affect the electrical potential, the MO levels, charge transport and the E_g, which eventually leads to the change of EC properties. According to Equation(1.29), the optical band gap can be determined using the Tauc relation[248]:

$$(\alpha h\nu) = A\ (h\nu - E_g)^n \quad (1.29)$$

where α, h, v, and A represents the absorption coefficient, Planck constant, light frequency, and proportionality constant, respectively. E_g is the optical band gap. If n is 0.5, it means a direct conduction band semiconductor, and if n is 2, it means an indirect conduction semiconductor.

Organic ECs have one main advantage of fast color switching. This makes them ideal candidates for electrochemical imaging, as a direct link could be established between the electrode potential and the redox ratio by Nernst Equation. Nevertheless, the long-term stability of organic ECs is usually unsatisfied. This could sometimes be enhanced by forming composite with inorganic electrochromic materials [249], which will be introduced in the following section[250].

1.4.2 Electrochromism in transition metal oxides

In terms of EC applications, tungsten oxide (WO_3) is the most studied transition metal oxide (TMO). It has high staining efficiency, high contrast, and highly chemical stability, making it an ideal material for practice. As an indirect bandgap semiconductor, its EC response is achieved by intercalation and deintercalation of H^+, Li^+, Na^+, and K^+ under potential bias[251]. As shown in the following reaction, WO_3 has reversible EC properties due to the formation of tungsten bronze (M_xWO_3).

$$WO_3\,(\text{transparent}) + xM^+ + xe^- \leftrightarrow M_xWO_3\,(\text{blue}) \tag{1.30}$$

where M represents H, Na, Li, *etc*. As ion insertion and electron injection under cathodic polarization, WO_3 films become the blue color. Through these processes, the band gap of WO_3 is altered, which affects light transmission. With the insertion of metal ions or H^+ into the lattice, the internal electromotive force increases, producing a colored state; similarly, electrons and metal cation (protons) are obtained by reversing the potential bias, resulting in bleaching.

In general, TMOs have band gaps between 1 and 5 eV (**Figure 1.17**) and thus occupy a position between semiconductors and dielectrics[252]. TMO structure influences EC behavior. The properties especially the physicochemical properties of the EC are directly impacted by structural and impurity defects. The E_g of WO_3 films decreases with increasing annealing temperature from 3.62 eV to 3.30 eV. Furthermore, colored WO_3 films have a lower E_g than bleached WO_3 films[253]. According to different E_g, it is illustrated that the conductivity of the WO_3 film increases with decreasing E_g, while the response time of the film increases with high conductivity.

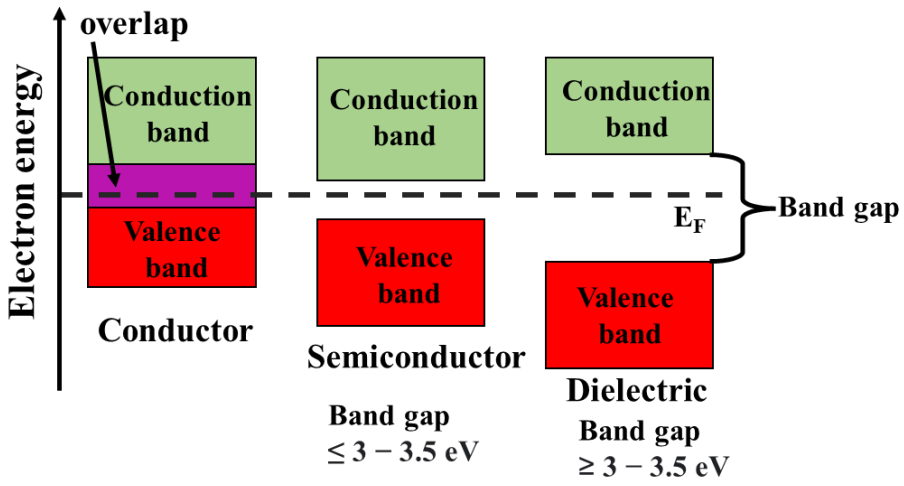

Figure 1.17 Classification of materials by conductivity[252].

The various structures of WO_3 films such as crystalline, poly-crystalline, amorphous or hybrid, determine their optical properties. Polycrystalline WO_3 films exhibit reflective properties as they transit from transparent to colored states, while WO_3 films with amorphous structures exhibit absorption properties. Switching time is determined by the density of the WO_3 film. The fastest switching speed can be achieved by low-density films with high concentration of electrolyte in the film.

The properties of inorganic ECs are just in complement with those of organic ECs. The long-term stability, especially for WO_3, is excellent. The electrochromic performance almost does not degrade even after thousands of coloring-bleaching cycles. Nevertheless, the coloration efficiency and the color switching speed are relatively low. The latter could be improved by using amorphous structure, or forming composite with organic ECs that change color at the same potential range.

1.4.3 Research aims in this thesis

The thesis work was carried out around the main concept of measuring signals from CE for electroanalysis. This includes the analysis of concentration from a micro-CE in **Chapter II**, and the visualization of local reactivity from an electrochromic CE in **Chapter III**.

Stripping voltammetry is very important analysis method for detecting ultra-low concentration of analyte. To achieve the detection for those kinds of analyte that can't pre-concentrated on the WE, the CE combine with stripping voltammetry is studied in

Chapter II. Some factors (size of CE, concentration, potential, time, *etc*.) affecting detection limit and sensitivity are evaluated. The practical application is also carried out by this CE analysis method and the result is compared with the conventional electrochemical method.

After getting familiar with the electrochemical cell design and the general concepts of CE electroanalysis, we will shift the target from concentration analysis to an unconventional "analyte", that is, the surface reactivity of electrodes. To solve some limitations (time-consuming, complicated design for WE, harsh requirement for electrolyte) by some traditional techniques (SECM, SPRM, ECLM, *etc*.) for analyzing surface reactivity of electrodes, we have developed a method by mapping the local optical change of CE to indirectly analyze the WE surface reactivity in **Chapter III.** To improve the resolution, the distance between WE and CE, voltage, time, electrolyte type is explored. Moreover, different kinds of WE substrates are studied to verify this method with wide application value.

Chapter II

Electrochemical stripping analysis from micro-counter electrode

2.1 Principle of the method

The WE is defined as the electrode at which the electrochemical reactions of interest occur[257]. It is often employed to study electrochemical reaction mechanisms, concentration measurement[259,260], and local reaction activity[261–263] in conjunction with a variety of electrochemical methods including cyclic voltammetry[13,261,262], chronoamperometry[8,263], differential pulse voltammetry[17,264,265]. However, the CE in electrochemical systems is often neglected as it just serves to flow current generated at WE for controlling its potential *versus* the reference electrode. Opening an electrochemistry textbook[266,267], most of the theories and analysis (if not all) are built around the WE, and the CE is supposed not to interfere the WE by having sufficiently large active area, distance from WE, low polarization, homogeneous current distribution, *etc.*

In this chapter, we attempt to carry out electrochemical stripping analysis not based on directly pre-concentrating the analyte on WE, but indirectly extracting signals from CE. The concept is illustrated in **Figure 2.1**. The electrochemical cell 1 consists of two compartments, which are denoted as Cell 1a and Cell 1b. The WE1 and the reference electrode (RE1) are placed in Cell 1a, whereas the CE1 is placed in Cell 1b. The two compartments are connected with a "bridge", which can be a salt bridge as in classical voltaic cells, or an electron conductor such as metal wire or plate. In the former case, compartments 1a and 1b are half-cells, while in the latter case they are independent electrochemical cells connected in series. The latter is often used as closed bipolar system for studying the reactions at the "bridge", but here we focus on the reactions on WE1 and CE1 (denoted as source electrodes in bipolar systems [42]) instead. A model analyte ($Fc(MeOH)_2$) is added in Cell 1a, while a suitable model metal ion (Cu^{2+}) is introduced in Cell 1b. By oxidizing the analyte on WE1 during the measurement, Cu^{2+} may be simultaneously reduced on CE1. The corresponding reactions are:

at WE1: $Fc(MeOH)_2 - 1\ e^- \rightarrow [Fc(MeOH)_2]^+$

at CE1: $Cu^{2+} + 2\ e^- \rightarrow Cu^{(0)}$

Consequently, the CE1 is taken out from Cell 1b, cleaned, and transferred to another electrochemical cell (Cell 2) for stripping analysis of Cu:

at WE2 (*i.e.*, CE1 coming from cell 1): $Cu^{(0)} - 2\ e^- \rightarrow Cu^{2+}$

Cell 2 is a classical three-electrode cell, with CE1 connected as WE2, and another pair of RE2 and CE2. The solution in Cell 2 only contains supporting electrolyte, with the pH adjusted to be favourable for Cu stripping. In this way, the charge corresponding to the oxidation of the analyte on WE1, which is related to the analyte concentration, is linked to the charge of Cu deposition on CE1. The latter can be analyzed by the stripping signals from Cell 2. Thus, the concentration of analyte can be indirectly determined by analysing the stripping signals from the CE. Like in classical stripping analysis, by increasing the oxidation of analyte on WE1, the charge of Cu deposition on CE1 is also expected to increase, leading to an increase in the stripping signal intensity which may improve the sensitivity of the analysis. This work explores a new access to electrochemical analysis through signals from CE, which may extend the applications of stripping to analytes that do not deposit or adsorb on the WE.

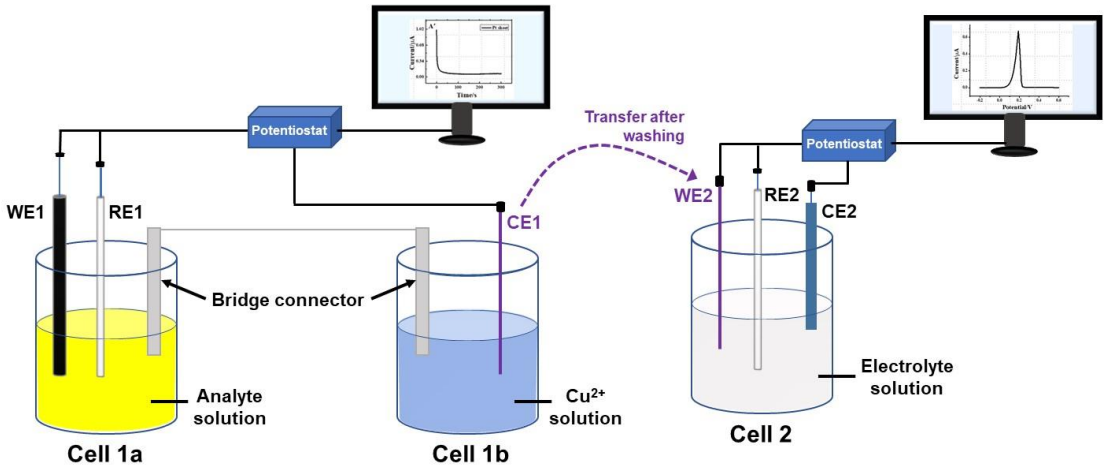

Figure 2.1 (A) Schematic diagram illustrating the indirect detection of $Fc(MeOH)_2$, via copper deposition and stripping in two separate setups, with cells composition as follow. Cell1a: various concentrations of $Fc(MeOH)_2$ +0.1M $NaNO_3$ (pH=5.58); Cell1b: 0.2 M $CuSO_4$ +0.1M $NaNO_3$ (pH=2); Cell2: 0.1M $NaNO_3$ (pH=2). WE1: glassy carbon electrode (GCE); RE1 and RE2: Ag/AgCl reference electrodes; CE1: Pt microelectrode (transferred to Cell 2 and connected as WE2 for anodic stripping); CE2: Pt sheet.

2.2 Experimental section

2.2.1 Configuration of the electrochemical cell

Components of the electrochemical cells. The custom-made electrochemical cells used to study the CE stripping voltammetry are different from the classical three electrode systems, which consist of two half cells. As shown in **Figure 2.1**, in a first compartment (cell 1a), a glassy carbon electrode (GCE) of 3 mm diameter (CHI 104) was connected as WE1, and a commercial Ag/AgCl (1 M KCl) reference electrode (CHI 111) was connected as RE1. In the second compartment (cell 1b), platinum electrodes of different size were used as CE1, including Pt sheet (2 mm × 0.5 mm, ChemPur, Germany), Pt disk electrode of 2 mm diameter (CHI 102), and Pt micro-disk electrode of 25 µm−300 µm diameter.

The types of bridge. Several types of "bridge" connecting cells 1a and 1b were studied (**Figure 2.2**): (1) ionic salt bridge prepared by agar and saturated potassium chloride solution filled in a glass U-tube; (2) Pt sheets of 0.5 cm width and 1 or 2 cm immersed length; (3) Cu wire of 0.5 mm diameter and 2.5 cm immersed length.

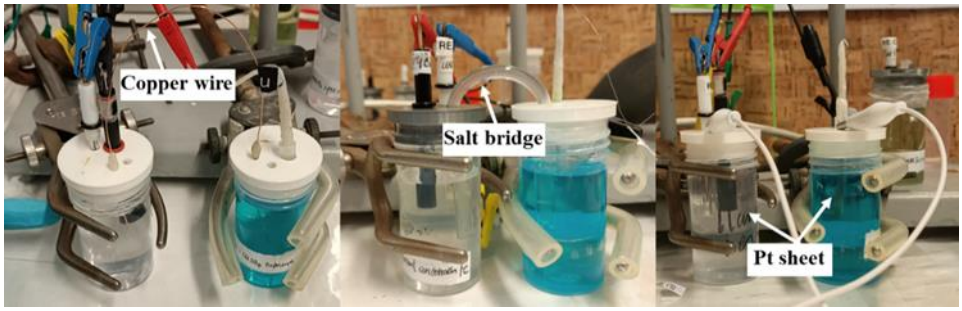

Figure 2.2 Three types of "bridge" connecting cells 1a and 1b.

2.2.2 Preparation of micro-counter electrode

Pre-treatment of glass capillary. Borosilicate glass capillary was pulled by micropipette puller (**Figure 2.3A**) to make a slim capillary end (**Figure 2.3B**). Afterward, the slim capillary end was sealed by CH_4 fire to load the gold wire. Next, the small fragments of Pt wire with various diameter (25 µm, 50 µm, 100 µm, 200 µm) were packed into sharp capillary, respectively.

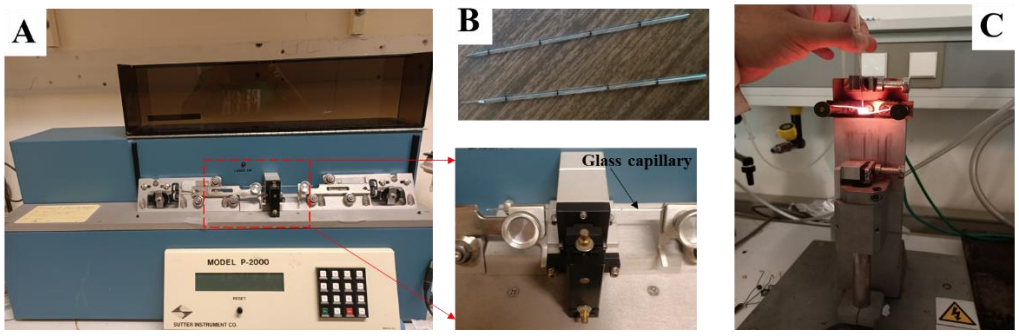

Figure 2.3 (A)The borosilicate glass capillary was pulled by micropipette puller. (B) The picture for obtained slim capillary tip. (C) The capillary end with Pt wire was sealed by the vertical capillaries' puller with current passing through the several scrolls wire.

Sealing of gold wire in glass capillary. The glass capillary with Pt wire was placed vertically with the opened end directed up wards so that another end including Pt wire was placed in the middle of the ring made from several scrolls of the nickel/chrome 80/20 wire (**Figure 2.3C**). Then, the pump was attached to the top of the capillary and current was passed through the wire and increased the temperature around the capillaries when an external power supply was used. Note: to ensure even heating for the glass around Pt wire, the heating temperature should be gradually increased and keep a suitable temperature for about 1 minutes until the glass wall around Pt wire collapsed, soldering the Pt wire. Afterward, copper wire (length: *ca.* 15 cm) with the conductive resin was inserted inside the capillary to connect with Pt wire, then left in the oven at 60°C for a few hours to dry. The length of the copper wire needs to be longer than that of the capillary as a few centimetres needs to extend out for electrical contact.

Polishing of sealed micro-CE. The sealed microelectrode was polished by the rough sandpaper to expose the Pt tip. Then the microelectrode was polished by smooth sandpaper (0.3 um) to get smoothy surface. Finally, the prepared microelectrode was

sonicated and rinsed thoroughly by deionized (DI) water, acetone and ethanol successively to remove the residue on the surface of microelectrode. Note: before use, the microelectrode should be polished gently with 0.05 um alumina powder on the soft cloth and sonicated by the deionized water, ethanol and water successively.

2.2.3 Characterization of microelectrode performance

To ensure that there is no infiltration between the Pt wire and capillary insulation in solution, and to measure the electrical contact between copper wires and Pt wire. The four sizes of microelectrodes were scanned from -0.2 V to 0.6 V in classical three-electrode cell with 1 mM $Fc(MeOH)_2$ solution at scan rate of 0.02 V/s. The obtained cyclic voltammetry curves of different size Pt microelectrode are shown in **Figure 2.4A and 2.4B.** The sigmoidal-shaped responses validated the better quality of the microelectrodes, and characterized the steady-state mass transfer. Note that the peaked response of microelectrode with a size of 200 μm is similar to those observed at conventional macroelectrode.

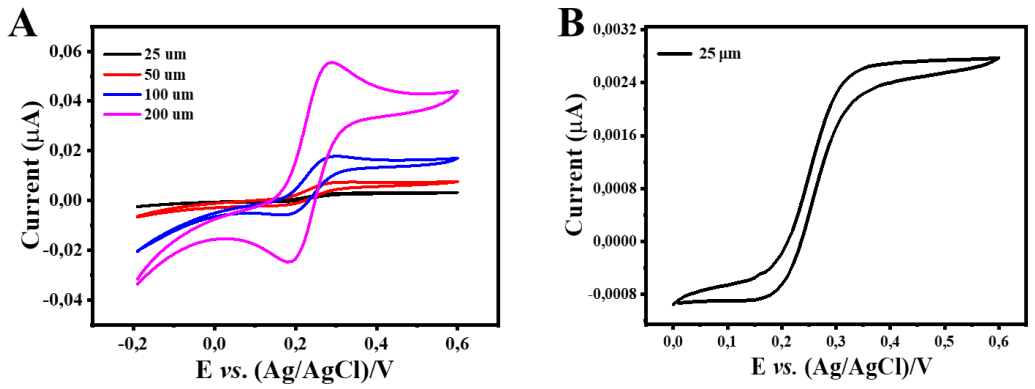

Figure 2.4 The cyclic voltammogram in 1 mM $Fc(MeOH)_2$ + 0.1 M $NaNO_3$ (pH 5.8) solution: (A) the four sizes of Pt microelectrodes as WE, respectively, Ag/AgCl as RE, and Pt sheet as CE.(B) The CV of a micro-electrode of 25 μm in an enlarged view.

The steady-state mass transfer on microelectrode can be explained as follows: firstly, at sufficient short time, the δ (diffusion layer) < r^0, this diffusion layer appears planar to a molecule at the edge of the spherical electrode. nder this condition, the electrode behaves like a macroelectrode and mass transport is dominated by linear diffusion to

the electrode surface as illustrated in **Figure 2.5A**. Therefore, at short time, the current is given by the Cottrell equation:

$$i(t)= \frac{nFAD_O^{1/2}C_O^*}{\pi^{1/2}t^{1/2}} \quad (2.1)$$

Where D_o is the diffusion coefficient for the active species, n is the number of electrons transferred in the redox reaction, F is Faraday's constant, A is the geometric electrode area, t is reaction time, C* is redox-active species of concentration. r^0 is the microelectrode radius.

At long times, the $\delta >> r^0$, the radial character of the electrode becomes important and the mass transport process is dominated by radial diffusion as illustrated in **Figure 2.5B**. The current is a time independent steady-state value given by the equation:

$$i_{ss}= \frac{nFAD_OC_O^*}{r^0} \quad (2.2)$$

The steady-state response occurs because the electrolysis rate equals the diffusion rate of molecules to the electrode surface.

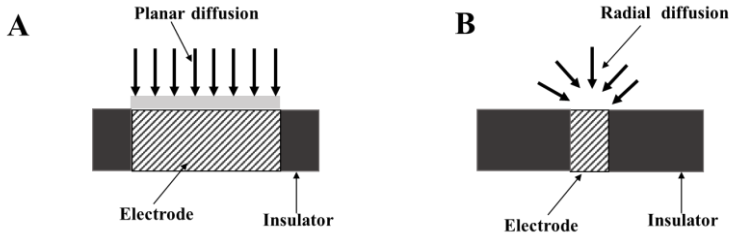

Figure 2.5 Diffusion fields observed at microelectrode: (A) Linear diffusion observed at short times. (B) Radial diffusion observed at long times.

2.3 The protocol of analysis

All electrochemical experiments were carried out on a PalmSens 4 potentiostat (PalmSens, Netherland). Before each measurement, CE1 was polished with 0.3 µm abrasive discs (Buehler, USA), and both WE1 and CE1 were then polished with 0.05 µm alumina paste on cloth. The electrodes were sonicated in water, EtOH and water consecutively. This procedure ensured thorough regeneration of both WE1 and CE1 before quantitative analysis. The first step of measurement was connecting Cell 1 for the oxidation of $Fc(MeOH)_2$. Linear scan voltammetry (LSV) or chronoamperometry

(CA) were performed, respectively by scanning potentials (from -0.2 to 0.6 V at 0.05 mV/s) or applying a constant potential (+0.3 V, typically for 300 s if not stated otherwise) at WE1. The current response as well as the cell voltage between WE1 and CE1 were recorded. Afterwards, the electrodes were disconnected, and CE1 was removed from Cell 1b, thoroughly rinsed with water and transferred to Cell 2. It was then connected as WE2, along with RE2 and CE2. The stripping analysis was performed by scanning the potential of WE2 from -0.2 to 0.6 V (*vs.* Ag/AgCl) at a scan rate of 50 mV/s. Most of the stripping experiments were carried out by LSV, while differential pulse voltammetry (DPV) was also applied in attempting to increase the sensitivity of the method. After each series of measurement, WE2 and WE1 were regenerated by polishing and sonication for the next one as described above. As each cell contains a different solution, we recommend to minimize cross-contamination by transferring only CE1/WE2 while keeping all other electrodes separate and always in their own cells. Note that both the classical three-electrode cell and the two separate compartments connected with either salt or metallic bridges gave exactly the same voltammetric signals (**Figure 2.6**). This indicates that the potentiostat functions normally under the experimental conditions.

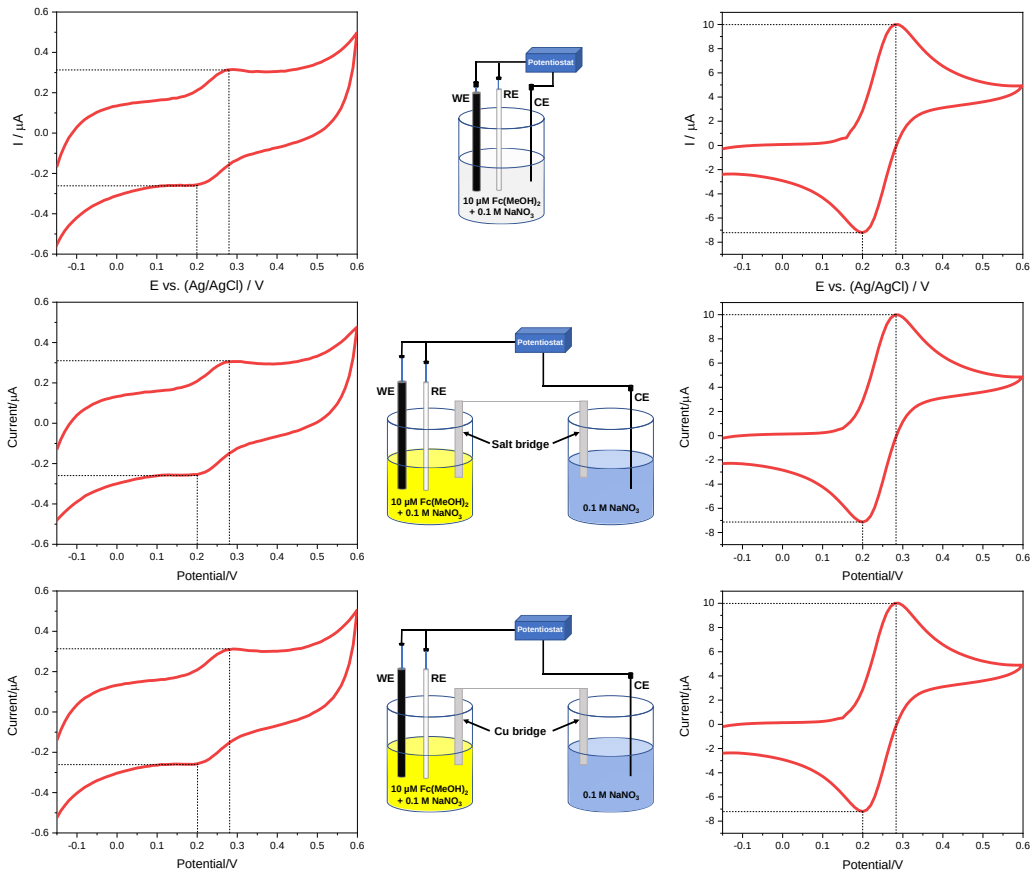

Figure 2.6 Voltammetric response of 10 µM (left) and 1 mM (right) $Fc(MeOH)_2$ in 0.1 M $NaNO_3$ using various configurations: classical three-electrode cell (top) and two half-cells connected with salt bridge (middle) or Cu bridge (bottom), showing peak potentials and currents at the same positions in all cases.

2.4 Results and Discussion

2.4.1 Proof-of-concept: Establishment of the method

As the concept is based on analyzing signals from CE, its choice is the first step to explore. Three Pt electrodes of different size are tested as CE1 for carrying out the same LSV analysis of $Fc(MeOH)_2$ in Cell 1: a Pt sheet of much larger area than WE1, a Pt disk electrode of comparable area as WE1, and Pt ultramicroelectrode of much smaller area than WE1. **Figure 2.7A** shows the current response as a function of scanning potential using the system made of the two compartments 1a&1b. The voltammogram is similar as that measured from classical three-electrode single cell, showing an oxidation peak for $Fc(MeOH)_2$ at *ca.* +0.22 V (*vs.* Ag/AgCl). The current recorded with different CE1 almost overlap, indicating that the size of CE does not change neither the peak potential not its intensity under these experimental conditions. During the measurement, the cell voltage, that is, the potential E_{WE1} *vs.* E_{CE1}, is also monitored, as shown in **Figure 2.7B.** Here, a clear difference is seen from different CE1. For the macroscopic Pt sheet and Pt disk, the cell voltage changes almost linearly as the potential of WE1 is scanned from -0.2 to +0.6 V (*vs.* Ag/AgCl). The slope as a function of time is almost the same as the scan rate of E_{WE1}. This suggests that the potential drop at the bridge (two electrochemical interfaces with the solutions in Cell 1a and 1b) and CE1 is stable, which fulfils the criteria for selecting CE [267]. However, when a Pt ultramicroelectrode is used as CE1, the cell voltage rapidly varies from -2.0 to 0 V in the first 1 s, and then slightly increases to *ca.* 0.8 V with similar slope as E_{WE1}. With the same current flowing through CE1 as seen from **Figure 2.7A**, the current density on Pt microelectrode is much higher than that on Pt sheet or disk. This leads to the polarization of the electrode and may explain the phenomenon. As the potential of E_{WE1} is controlled, the more positive E_{WE1} *vs.* E_{CE1} qualitatively suggests that the potential of E_{CE1} is more negative, which drives the reduction of Cu^{2+} in Cell 1b to form $Cu^{(0)}$ deposit on CE1. This is examined by transferring CE1 to Cell 2 (as WE2) for anodic

stripping. **Figure 2.7C** shows a clear stripping peak of $Cu^{(0)}$ at *ca.* 0.18 V (vs. Ag/Cl) for Pt ultramicroelectrode, which cannot be detected when using Pt sheet and disk electrodes (see inset). The deposition of Cu on micro-Pt CE1 is further confirmed with optical microscopy observation (**Figure 2.8**). This suggests the possibility to capture potentially useful signals from microelectrode CE, supporting the feasibility of the concept. Note that the quantitative analysis of the potential E_{CE1} *vs.* E_{RE1} would be difficult due to the two electrochemical interfaces of the "bridge" with the solutions in Cell 1a and 1b.

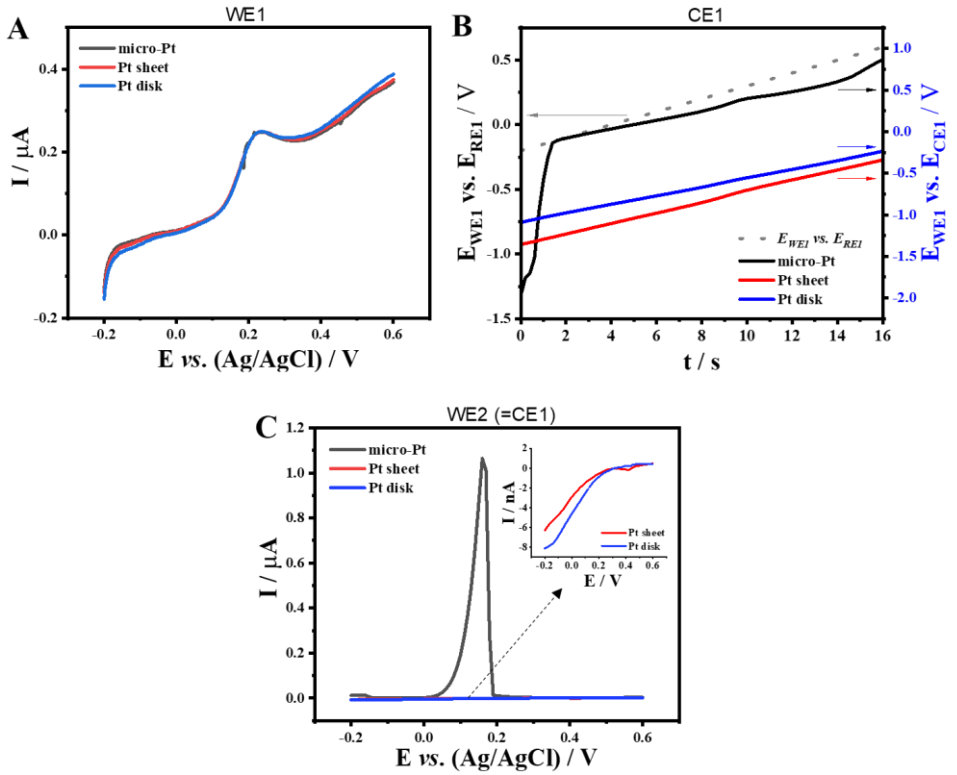

Figure 2.7 Linear sweep voltammetry in Cell 1 with GCE as WE1, Ag/AgCl as RE1, and Pt sheet, disk or ultramicroelectrode as CE1: (A) current response at WE1. (B) variation of cell voltage with time. Solution in Cell 1a: 10 µM $Fc(MeOH)_2$ + 0.1 M $NaNO_3$ (pH 5.8); solution in Cell 1b: 0.2 M $CuSO_4$ + 0.1 M $NaNO_3$ (pH 2); "bridge": Cu wire; scan rate: 50 mV/s. (C) Anodic stripping voltammetry of CE1 transferred as WE2 in Cell 2. Solution: 0.1 M $NaNO_3$ (pH 2); scan rate: 50 mV/s. Inset graph: enlarged views of current at Pt sheet and disk electrodes.

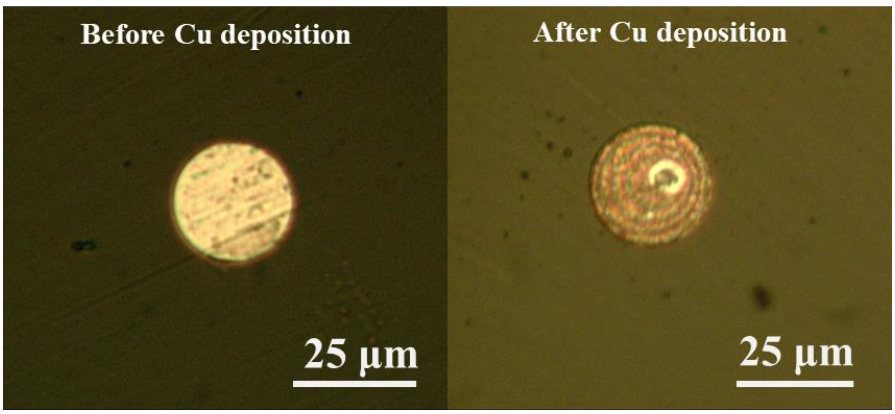

Figure 2.8 Optical microscope images of CE1 before (A) and after (B) $Cu^{(0)}$ deposition at counter electrode during linear scan voltammetry in Cell 1 in conditions of **Fig. 2.7**.

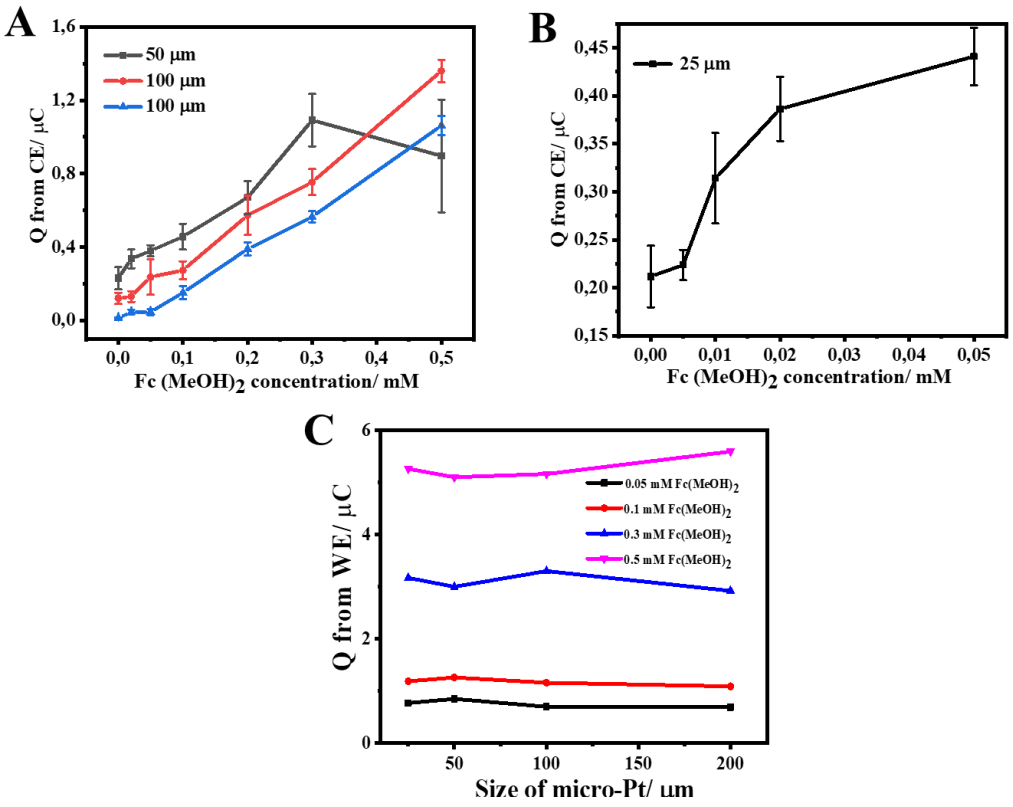

Figure 2.9 The analysis of $Cu^{(0)}$ deposition amounts for four different sizes of micro-CE (25 µm, 50 µm, 100 µm, 200 µm): (A,B) variation of the charge recorded during the anodic redissolution of the deposited $Cu^{(0)}$ as a function of $Fc(MeOH)_2$ concentration in cell 1a (in 0.1 M $NaNO_3$ at pH 5.8). (C) currents recorded at WE1 in Cell 1. Solution in Cell 1b: 0.2 M $CuSO_4$ + 0.1 M $NaNO_3$ (pH 2); "bridge": Cu wire; scan rate: 50 mV/s. Error bars indicate the standard deviation of 5 repetitive measurements.

To study the effect of size of micro-CEs on the amount of deposited $Cu^{(0)}$, the four sizes of Pt microelectrodes (25 μm, 50 μm, 100 μm, 200 μm) were used as CE, respectively. The experiment was carried out by scanning the LSV from 0 to 0.6 V with scan rate of 0.05 V/s to oxidize different concentration of $Fc(MeOH)_2$ solution at the surface of GCE in cell 1 a, and at the same time the different size of microelectrodes as CE in the cell 1b with 0.2 M $CuSO_4$+0.1 M $NaNO_3$(pH=2) to deposit $Cu^{(0)}$, respectively. The amount of $Cu^{(0)}$ deposited on the micro-CEs can be obtained by transferring them to the cell 2 for $Cu^{(0)}$ stripping analysis. As shown in **Figure 2.9A**, as the concentration of $Fc(MeOH)_2$ increases, the $Cu^{(0)}$ deposition amounts also increases on the micro-CEs, but the size for 50 μm of micro-CE decreases after detecting 0.3 mM of $Fc(MeOH)_2$, which might be due to excessive $Cu^{(0)}$ shedding due to small area electrode size. In addition, the amount of $Cu^{(0)}$ deposited on the different sizes of micro-CEs for detecting same concentration of $Fc(MeOH)_2$ follows the trend: 50 μm >100 μm > 200 μm. This is due to the fact that under the same current conditions, the smaller the micro-CE size, the higher the current density, and the easier it is to polarize the micro-CE and deposit more $Cu^{(0)}$. Based on this, we further used 25 μm microelectrode as CE to study the $Cu^{(0)}$ deposition amounts when detecting lower concentration range of $Fc(MeOH)_2$. The $Cu^{(0)}$ deposition amounts for 25 μm micro-CE is higher than that of the 50 μm micro-CE when detecting the concentration of $Fc(MeOH)_2$ from 0.02 mM to 0.1 mM (**Figure 2.9B**). Moreover, further extending the concentration of $Fc(MeOH)_2$ below 0.02 mM, there is still Cu(0) deposition on the micro-CE, so reducing the micro-CE size would improve the lower detection limit of this analysis method. **Figure 2.9C** shows that the charge from oxidation of four different concentrations of $Fc(MeOH)_2$ on WE hardly changes with the increase of micro-CE size, indicating that the effect of size change in cell1b on the oxidation of $Fc(MeOH)_2$ in cell1a can be neglected.

After choosing micro-Pt as the most suitable CE1 electrode, the next step is to investigate the measurement method for quantification. **Figure 2.10A** compares the LSV of 10 μM $Fc(MeOH)_2$ with that of the blank solution (*i.e.,* electrolyte without $Fc(MeOH)_2$) in Cell 1a. It is seen that the oxidation peak may clearly differentiate the two solutions, with evidently no peak observed in the absence of the redox probe. Nevertheless, in both solutions $Cu^{(0)}$ deposition is occurring on CE1 as evidenced by stripping peaks recorded in Cell 2, yet with higher current in $Fc(MeOH)_2$ solution than in the blank (**Figure 2.10B**). The quantity of $Cu^{(0)}$ deposited on CE1 is slightly more

than two times larger (as seen from the stripping current/charge in Cell 2) when $Fc(MeOH)_2$ is present in Cell 1a, further confirming the feasibility for indirect analysis, yet still unfavourable for quantification due to the presence of quite high signal from the analyte-free blank solution. This is because the deposition of $Cu^{(0)}$ on CE1 is affected by the polarization, which depends on the current flow through the cell (WE1 and CE1) but cannot differentiate the nature of the current (Faradic and residual/capacitive) [44]. That is to say, as long as the potential of CE1 allows, both non-Faradaic and Faradaic current for WE1 may contribute to $Cu^{(0)}$ deposition on CE1. In LSV, non-Faradaic current is always present due to the scanning potential, thus it may complicate the quantification analysis from CE1 stripping signals. Therefore, chronoamperometry (CA) is used to reduce the interference of non-Faradaic current by fixing the potential applied on WE1 at a value enabling the oxidation of the probe. **Figure 2.10C** shows the current variation with time by applying a potential of +0.3 V (*vs.* Ag/AgCl). The current also consists of non-Faradaic and Faradaic components but the former, I_{nF}, depending on the solution resistance and the double-layer capacitance of the electrode, decreases rapidly with time (equation 2.3) [103].

$$\boldsymbol{I_{nF}(t) = \frac{E}{R_s} e^{(-t/R_s C_{dl})}} \tag{2.3}$$

with R_s the solution resistance and C_{dl} the double layer capacitance. Normally, the range R_s is 10-100 Ω and C_{dl} is 10-100 µF, so that the double layer charging current becomes negligible rapidly after applying the potential step (*ca.* after 50 ms), which is much less than the time window of the experiments performed here. Therefore, the charge flowing through the cell 1 mainly depends on the Faradaic current, I_F, which in this case approximately follows Cottrell equation (equation. 2.4) [103] and it is proportional to the concentration of the analyte $Fc(MeOH)_2$ and to the inverse of square root of time.

$$\boldsymbol{I_F(t) = \frac{nFAD^{1/2}C}{(\pi t)^{1/2}}} \tag{2.4}$$

with n the number of exchanged electrons, F the Faraday constant, A the electrode surface area, D the diffusion coefficient of the probe and C its concentration in solution. It means that I_F still keeps 10% of its value when passing from 1 to 100 s of CA experiment. Note that when the concentration of $Fc(MeOH)_2$ near WE1 is very low due to the diffusion limit, the kinetics of its oxidation cannot be negligible. This may explain the current "plateau" at a very low value (order of magnitude lower than the initial current) instead of decreasing to zero. Nevertheless, the kinetics also depend on the

concentration of $Fc(MeOH)_2$ thus the linear relationship between Faradaic current and $Fc(MeOH)_2$ concentration is still valid. It also explains the higher current "plateau" for $Fc(MeOH)_2$ solution as compared with that for the blank one. As a consequence, the quantity of $Cu^{(0)}$ deposited on CE1 is also much higher after measurement in $Fc(MeOH)_2$ than in the blank solution, as seen from the stripping signal in Cell 2 (**Figure 2.10D**). It is interesting to see that $Cu^{(0)}$ deposition is invisible after chronoamperometry in the blank solution, even though the current is not zero due to the non-Faradaic contribution. This is perhaps due to the charging of CE1 that compensates (at least partially) the non-Faradaic charge on WE1. Although the area of CE1 is much smaller than that of WE1, the potential step induced by the flown current can be much steeper thus the non-Faradaic charge may also not be negligible. From the analytical point of view, **Figure 2.10D** eliminates the blank signal as compared with **Figure 2.10B**. It also offers more significant difference in $Cu^{(0)}$ deposition charge for analysing the same concentration of $Fc(MeOH)_2$ (**Figure 2.11**). Thus, chronoamperometry is more preferable and was chosen for further quantitative analysis.

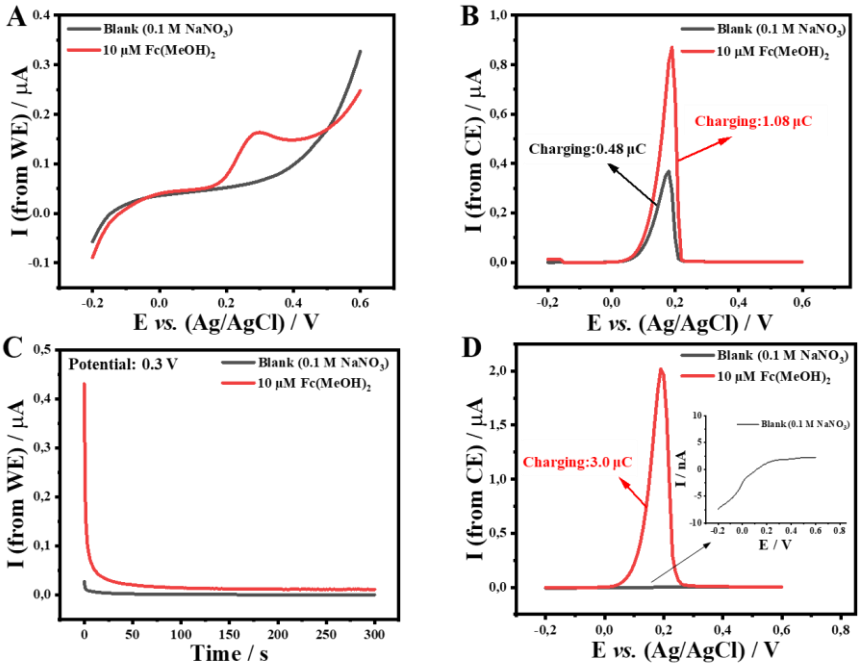

Figure 2.10 (A) LSV of GCE in 10 µM Fc(MeOH)$_2$ (red line) and the blank solution (black line) in Cell 1a. (B) Corresponding anodic stripping of $Cu^{(0)}$ deposited on CE1, as measured by LSV in Cell 2 after treatment as in (A). (C) chronoamperometry of GCE in 10 µM Fc(MeOH)$_2$ (red line) and the blank solution (black line) in Cell 1a at an applied potential of +0.3 V (*vs.* Ag/AgCl). (D) Corresponding anodic stripping of $Cu^{(0)}$ deposited on CE1 after treatment as in (C). Scan rate in (A), (B) and (D): 50 mV/s; Cu^{2+} concentration in Cell 1b: 0.02 M; "bridge" connector: copper wire.

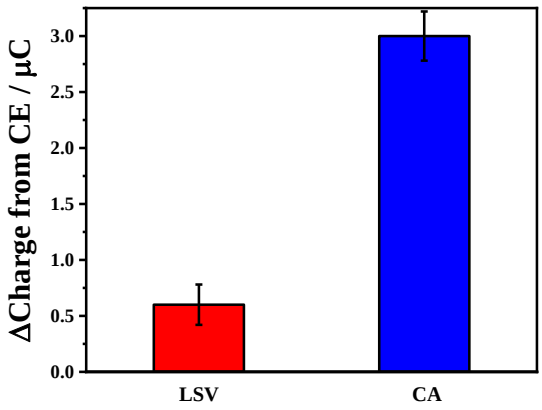

Figure 2.11 The difference of Cu stripping charge recorded from CE1 for experiments performed either by LSV or by CA from solutions containing 10 μM $Fc(MeOH)_2$ and no redox probe (blank), in the same conditions as in **Fig. 2.10**. Error bars indicate the standard deviation of 5 repetitive measurements.

2.4.2 The effect of CE size on the copper deposition

The choice of CE has been discussed in **Figure 2.7** by applying LSV on the cell1. Here, the chronoamperometry is chosen to oxidize $Fc(MeOH)_2$ on the cell1 to further explore the CE size effect. **Figure 2.12A** shows the current response curve with applying 0.3V for the oxidation of $Fc(MeOH)_2$ by extending time to 300 s on the WE. The chronoamperometry curves behave extremely similar when micro-Pt and Pt sheet are used as CE in cell1b with 0.2 M $CuSO_4$ solution (pH=2) respectively. However, the CE potential between the micro-Pt and Pt sheet is completely different (**Figure 2.12B**). Micro-Pt has more negative potential range than that of Pt sheet, potential range of the latter tends to be positive. Consequently, the Cu stripping signal (high peak) of micro-Pt in cell2 is obvious while there is no stripping peak to be observed from Pt sheet (**Figure 2.12C**). The result demonstrate the micro-Pt is optimal choice as CE in this system which is consistent with the conclusion from **Figure 2.7**.

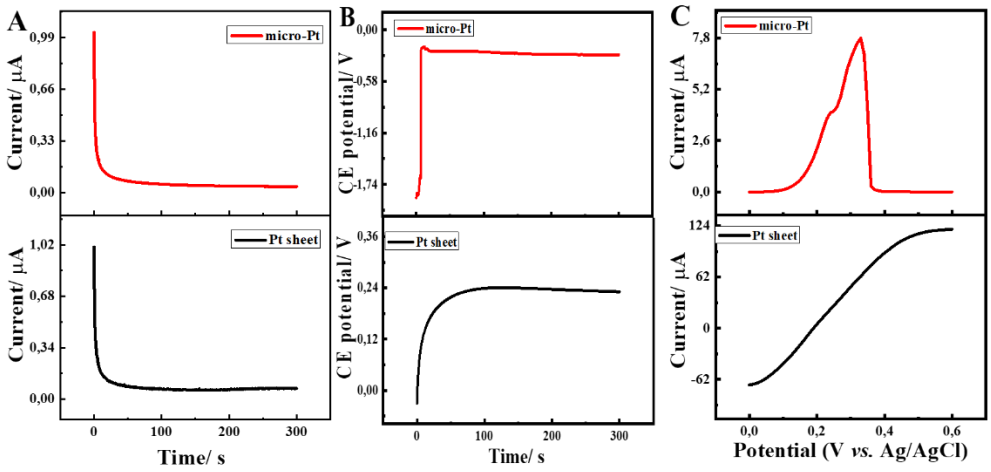

Figure 2.12 Chronoamperometry in Cell 1 with GCE as WE1, Ag/AgCl as RE1, and disk or microelectrode as CE1: (A) Current response. (B) Potential of CE1 *vs.* RE1. Solution in Cell 1a: 0.05 mM $Fc(MeOH)_2$ + 0.1 M $NaNO_3$ (pH 5.8); Solution in Cell 1b: 0.2 M $CuSO_4$ + 0.1 M $NaNO_3$ (pH 2). "Bridge": Cu wire. Applied potential: 0.3 V. (C) Anodic stripping analysis of CE1 in Cell 2. Solution: 0.1 M $NaNO_3$ (pH 2). Scan rate: 50 mV/s.

2.4.3 The effect of the position of CE on the electrochemical reaction on WE

Because the device is designed to separate the WE from the CE by using two compartments in this experiment (**Figure 2.1**), it is necessarily to study the effect of position of the CE on charge from current integration on the WE. Herein, the CE is placed in same cell with WE (**Figure 2.13C**), the signal from WE can be obtained by the application of chronoamperometry at the absence and presence of 0.006 mM $Fc(MeOH)_2$ for 300 s. By contrast, the same conditions are used on the device in **Figure 2.13A,** it is clearly seen that the charge from current integrate on WE for detection of blank solution and $Fc(MeOH)_2$ is extremely similar (**Figure 2.13 B**)when the CE is placed in double device (**Figure 2.13A**) and single device (**Figure 2.13C**). The results demonstrate that the oxidation reaction of $Fc(MeOH)_2$ is not affected by the position of CE (either in cell 1a or cell 1b), confirming further the proper use of the bridges.

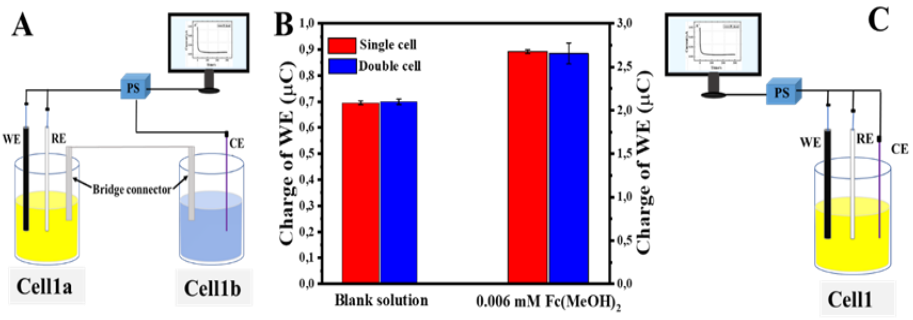

Figure 2.13 Schematic diagram for the detection of $Fc(MeOH)_2$: (A) the WE and CE in different cell and (C) the WE and CE in same cell. (B) Charge from current integration on WE at the absence and presence of $Fc(MeOH)_2$. Error bars indicate the standard deviation of 5 repetitive measures. Applied potential:0.3V. Cell1a and Cell1: different concentration $Fc(MeOH)_2$+0.1M $NaNO_3$(PH=5.58); Cell1b: 0.2 M $CuSO_4$+0.1M $NaNO_3$(PH=2).

2.4.4 Factors affecting the analysis

Based on the results above, one can conclude that chronoamperometry is suitable for the stripping analysis of non-adsorbing $Fc(MeOH)_2$ model analyte, indirectly from the stripping of $Cu^{(0)}$ on the CE. To gain more insights into the analytical process, various factors that may affect the signals were systematically studied. These include the electrolysis duration and the potential applied on WE1 in Cell 1a, the Cu^{2+} concentration and pH of the electrolyte solution in Cell 1b, as well as the type of "bridge" connector.

A first parameter likely to influence the electrode response is the time afforded for the oxidation of the probe. Like in classical stripping voltammetry where the analyte is pre-concentrated on the working electrode by deposition for a period of time for enhancing the signals, the chronoamperometry on WE1 may also offer a possibility to increase the amount of $Cu^{(0)}$ deposited on CE1 by prolonging chronoamperometry in Cell 1 and consequently increase the stripping signal measured from Cell 2. **Figure 2.14A** shows the charge integrated from chronoamperometry curves at increasing electrolysis times for blank and analyte solutions. It is seen that the charge increases with time for all the

solutions, yet being more intense for those containing the $Fc(MeOH)_2$ probe, which agrees with the non-zero current in the measurements. In contrary, the variation of charge corresponding to the stripping of deposited $Cu^{(0)}$, as measured in Cell 2, shows a different behavior(**Figure 2.14B**). For the blank solution, no $Cu^{(0)}$ is detected even by extending the chronoamperometry duration time to 1000 s. This suggests that the low residual current in blank solution may not be sufficient to polarize CE1 to a potential favourable for Cu^{2+} reduction. It is ideal from the analytical aspect to have a zero blank signal. For 10 µM $Fc(MeOH)_2$ solution, the $Cu^{(0)}$ stripping charge increases as the potential is applied on WE1 for longer time, which is consistent with the oxidation of more $Fc(MeOH)_2$ on WE1 and concomitant Cu^{2+} reduction on CE1, similarly as in classical stripping analysis. However, when the $Fc(MeOH)_2$ concentration is 50 µM, the $Cu^{(0)}$ stripping charge increases with time only up to 600 s, and then decreases even though the integrated charge from chronoamperometry continues to increase (compare blue curves in **Figure 2.14**).

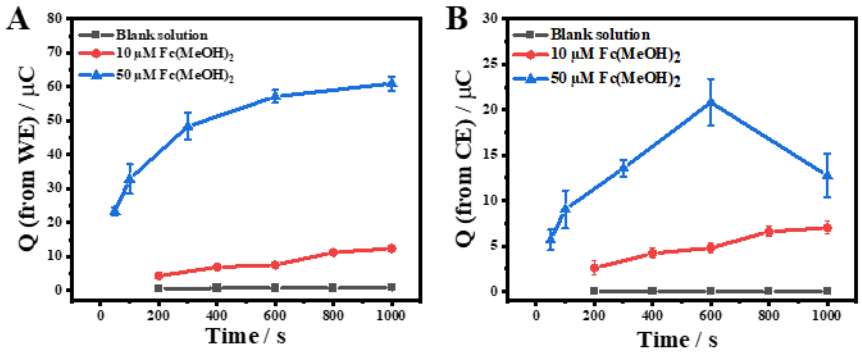

Figure 2.14 Variation of charge as a function of chronoamperometry duration (by applying +0.3 V to WE1 for various times in blank or 10 and 50 µM $Fc(MeOH)_2$ solutions in Cell 1a), respectively, measured from integration of (A) chronoamperometry currents recorded at WE1 in Cell 1 or (B) stripping signals obtained with WE2 (=CE1) in Cell 2. Error bars indicate the standard deviation of 5 repetitive measurements.

One possible explanation for this phenomenon is that the Pt micro-counter electrode is too small to carry large amounts of deposited $Cu^{(0)}$, so the excess of deposit might partially peel off from CE1 leading to the decrease in stripping charge of WE2. This is also supported by the shape of stripping curves that show multiple peaks of $Cu^{(0)}$ oxidation (an indication of multi-layer deposition, **Figure 2.15**). Overall, the above

results suggest that extending time may enhance the charge of $Cu^{(0)}$ stripping on WE2 for measuring low concentrations of analyte in Cell 1a, while it is unfavourable in the case of too high analyte concentrations due to excess deposition. The latter could potentially be solved by using CE1 of larger area. Nevertheless, as the analytical interest is naturally on low concentration, this is not further explored in this work. The relationship between time, $Fc(MeOH)_2$ concentration and copper deposition charge, paves the way for indirectly "stripping" $Fc(MeOH)_2$ from the CE, and constitutes the basis for further quantitative analysis.

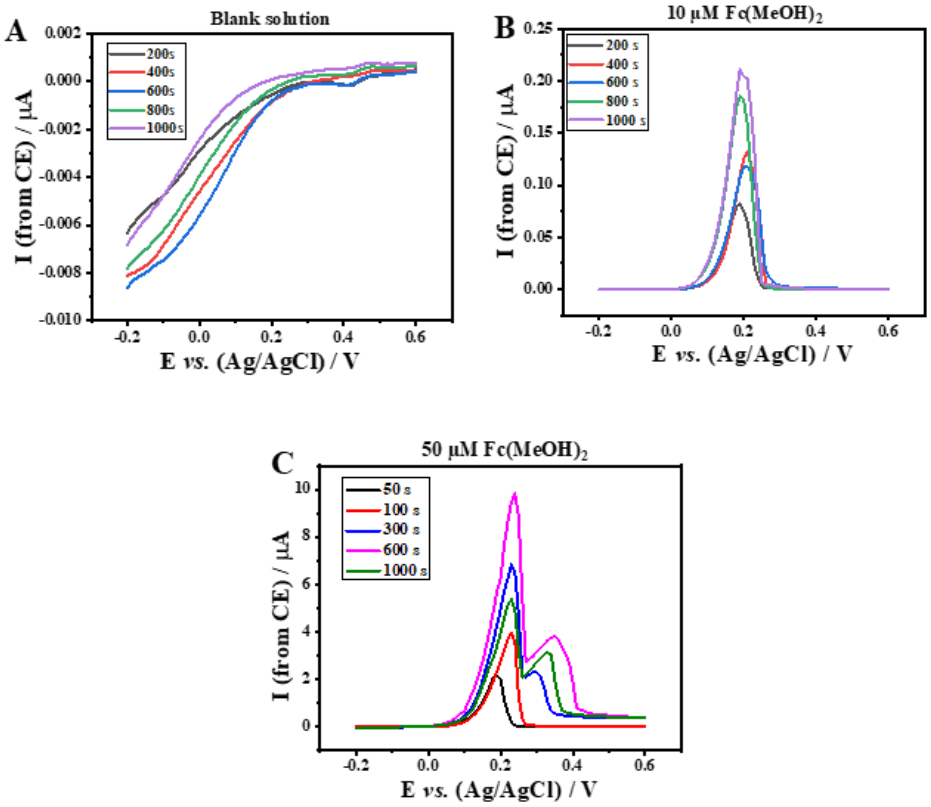

Figure 2.15 Cu stripping curves recorded from counter electrode in Cell 2 after various electrolysis times in Cell 1a containing (A) no (blank), (B) 10 µM and (C) 50 µM $Fc(MeOH)_2$. Conditions as in **Fig. 2.14B**.

Figures 2.16 and **2.17** show the effect of applied potential on the signals from WE1 and the WE2 (= CE1). It is seen from **Figure 2.16 A** that the charge integrated from current response in Cell 1 increases with applied potential for both blank and 30 µM $Fc(MeOH)_2$ solutions. The charge measured in the presence of $Fc(MeOH)_2$ is higher than that measured from the blank, which is evidently due to the Faradaic contribution from the oxidation of the redox probe. Moreover, the increase in charge tends to level

off above +0.3 V, a value approaching the formal redox potential of $Fc(MeOH)_2$. At high potential, the oxidation current is limited by diffusion, which tends to be independent of potential when the electrode surface concentration of $Fc(MeOH)_2$ is zero. In reality, a slight increase in current and charge is still observed when the potential increases beyond +0.3V (**Figure 2.17B**), as a result of slightly faster electron transfer kinetics at larger overpotentials. **Figure 2.16B** shows the variation of the charge corresponding to the deposited $Cu^{(0)}$ on CE1, which is measured from stripping of WE2 in Cell 2. In the presence of $Fc(MeOH)_2$, the general trend is similar to **Figure 2.16A**, confirming that the charge of $Cu^{(0)}$ stripping is correlated with the oxidation of the probe on WE1. At larger overpotentials, excess deposition of $Cu^{(0)}$ is seen from multiple peaks in stripping (**Figure 2.17 D**). It should be noted that for the blank solution, if copper deposition is not detectable when the potential is up to +0.3 V (consistent with above data (**Figure 2.14**) suggesting that stripping signal from counter-electrode may shield part of the blank signals), this is no more true when the potential increases beyond +0.3 V for which the blank solution also yields a visible $Cu^{(0)}$ stripping signal (due to greater polarization of the electrode). Therefore, we consider +0.3 V *vs.* Ag/AgCl as an optimal potential for the indirect determination of $Fc(MeOH)_2$ by stripping.

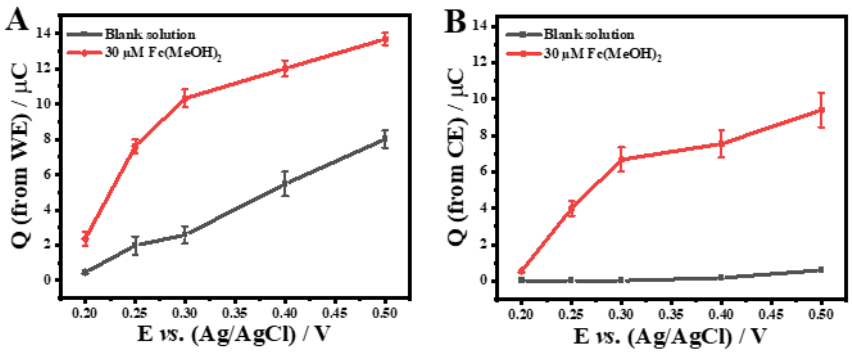

Figure 2.16 Effect of the potential applied to WE1 for 300 s in blank and 30 µM $Fc(MeOH)_2$ solutions in Cell 1a, on the charges measured from integration of (A) CA currents recorded at WE1 in Cell 1 or (B) stripping signals obtained with WE2 (= CE1) in Cell 2. Error bars indicate the standard deviation of 5 repetitive measurements.

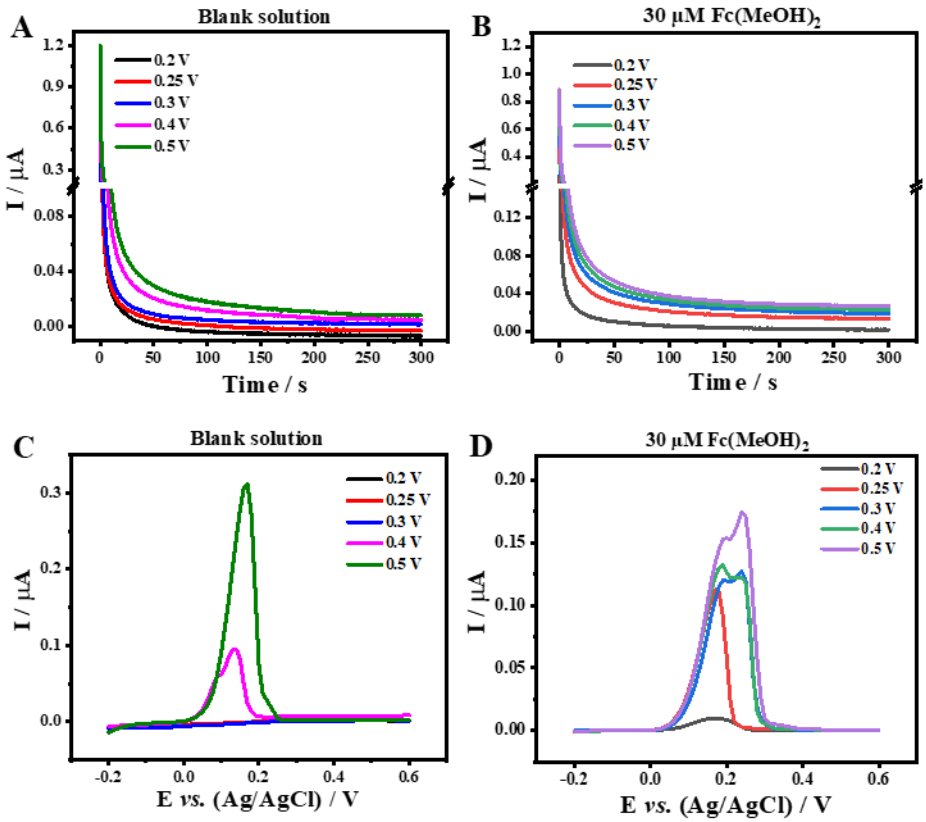

Figure 2.17 (A,B) Current-time response on the WE in Cell 1, and (C,D) anodic stripping curves recorded from CE in Cell 2, as obtained after applying various constant potentials at the WE in (A,C) blank solution or (B,D) in the presence of 30 µM $Fc(MeOH)_2$, respectively.

As the analysis is carried out indirectly from the signals obtained from CE1 (= WE2), the whole part of Cell 1b can be regarded as the sensing element. That being said, apart from the selection of CE (shown in **Figure 2.7**), the solution in Cell 1b is also likely to play an important role. As the stripping signals measured from WE2 in Cell 2 arise from copper reduction/deposition on CE1, the concentration of Cu^{2+} in Cell 1b would affect the deposition process and thus influence the whole analysis. **Figure 2.18A** shows that the charge from chronoamperometry current integration almost keeps unchanged with Cu^{2+} concentration in Cell 1b by applying +0.3 V *vs.* Ag/AgCl for 300 s on WE1 for any fixed $Fc(MeOH)_2$ concentration in Cell 1a. This is not really surprising as the composition of the compartment 1b comprising the counter-electrode is not expected to affect the response of WE1 in Cell 1a. The only variation of charge is that with increasing $Fc(MeOH)_2$ concentration, as expected by the oxidation of larger amounts $Fc(MeOH)_2$ (in agreement with the trend from previous figures). Nevertheless, with the

same charge passing through WE1 and CE1, the amount of $Cu^{(0)}$ deposited on CE1 is different when the concentration of Cu^{2+} in Cell 1b differs, as shown in **Figure 2.18B**. A general trend is that the $Cu^{(0)}$ stripping charge first increases and then decreases as the Cu^{2+} concentration in Cell 1b increases. With 0.002 M Cu^{2+} in Cell 1b, the deposition is likely diffusion-controlled as the solution is not stirred during the analysis. As a result, the deposition of $Cu^{(0)}$ is limited. This may also explain that at so low Cu^{2+} concentration in Cell 1b, different concentration of $Fc(MeOH)_2$ in Cell 1a results in almost insignificant difference in the $Cu^{(0)}$ stripping charge (**Figure 2.18B**) even though the charge flowing through Cell 1 significantly increases (**Figure 2.18A**). When Cu^{2+} concentration is in the range of 0.02 to 0.2 M, the kinetic contribution to $Cu^{(0)}$ deposition is dominant, thus the amount of reduced copper increases and becomes more dependent on the current or charge flowing through Cell 1. This notably affects the signals for relatively high concentration (30 µM) of $Fc(MeOH)_2$. However, when the Cell 1b contains 2 M Cu^{2+}, the charge measured from stripping decreases for all the three solutions of distinct $Fc(MeOH)_2$ concentration (with copper deposits less visible from optical microscopy, **Figure 2.19**), the reason for this phenomenon remaining unclear. The coulombic efficiency ((CE%) is ratio of charge of Cu striping from CE to charge on WE) is higher at 0.02 M Cu^{2+} compared to another concentration in cell 1b for three different concentration of $Fc(MeOH)_2$ in cell 1a (**Figure 2.18C**). From results of **Figure 2.18**, one can conclude that the Cu^{2+} concentration in Cell 1b may influence the stripping charge for analyzing the same $Fc(MeOH)_2$ solution under the same conditions, and that values in the range of 0.02 to 0.2 M Cu^{2+} would be the most suitable for quantitative analysis.

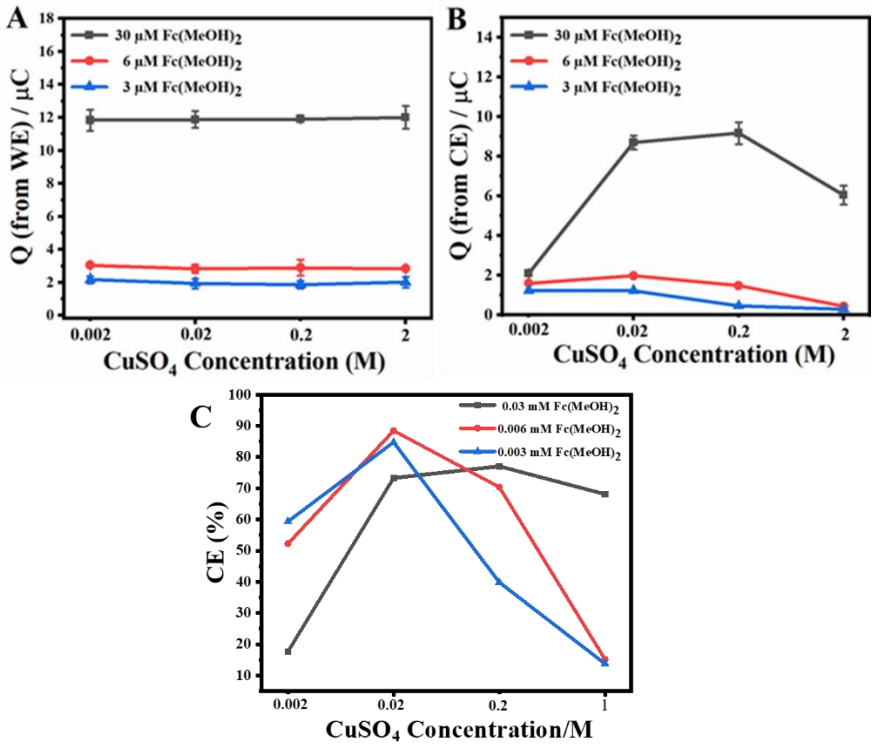

Figure 2.18 Effect of Cu^{2+} concentration in Cell 1b, on the charges measured from integration of (A) chronoamperometry currents recorded at WE1 in Cell 1 or (B) stripping signals obtained with WE2 (= CE1) in Cell 2. (C) The coulombic efficiency (CE%). The data correspond to chronoamperometry experiments performed by applying +0.3 V (*vs.* Ag/AgCl) to WE1 for 300 s, in solutions containing 3, 6 or 30 μM $Fc(MeOH)_2$ in Cell 1a. Error bars indicate the standard deviation of 5 repetitive measurements. The Cu^{2+} concentration axis is in logarithmic scale.

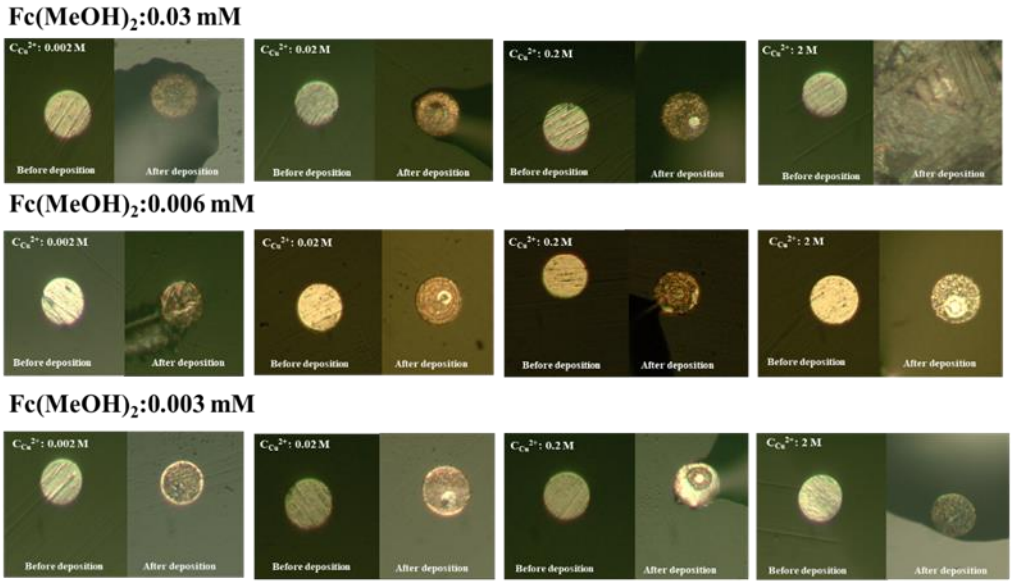

Figure.2.19 Optical microscope images (before and after copper deposition) corresponding to data presented in **Fig. 2.18** (various $Fc(MeOH)_2$ concentration in Cel1 1a and various Cu^{2+} concentrations in Cell 1b). The micro-Pt diameter is 25 µm.

Besides Cu^{2+} concentration, pH of the solution in Cell 1b may also influence the measurement. **Figure 2.20** compares the charge measured from integrating the current on WE1 and that from $Cu^{(0)}$ stripping on CE1 (=WE2), for the analysis of 10 µM $Fc(MeOH)_2$ in Cell 1a, and using 0.2 M Cu^{2+} at various pH in Cell 1b. It is clearly seen that the charge from current integration on WE1 almost keeps constant. This agrees with previous results (**Figure 2.18A**), indicating that the composition of Cell 1b does not affect the current measurement during oxidation of $Fc(MeOH)_2$. The charge calculated from $Cu^{(0)}$ stripping is always lower than that measured from current integration on WE1, which can be attributed to H_2 evolution (a competing reaction for Cu^{2+} reduction under cathodic polarization of CE1). This is especially significant at pH 1 while the H_2 evolution effect is less pronounced at pH 2, leading to an increase in the $Cu^{(0)}$ stripping charge. In less acidic solutions, especially at pH 4, the reduction of Cu^{2+} may get complicated by forming intermediates containing $Cu^{(I)}$ species. The stripping signal is also less clean with multiple peaks (**Figure 2.21**), which is not favorable for quantification.

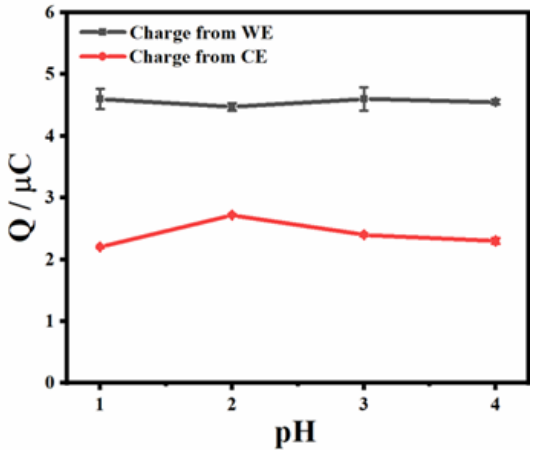

Figure 2.20 Effect of pH of the Cu^{2+} solution (0.2 M) in Cell 1b, on the charges measured from integration of chronoamperometry currents recorded at WE1 in Cell 1 (black) or stripping signals obtained with WE2 (=CE1) in Cell 2 (red). The data correspond to chronoamperometry experiments performed by applying +0.3 V (*vs.* Ag/AgCl) to WE1 for 300 s, in a solution containing 10 µM $Fc(MeOH)_2$ in Cell 1a. Error bars indicate the standard deviation of 5 repetitive measurements.

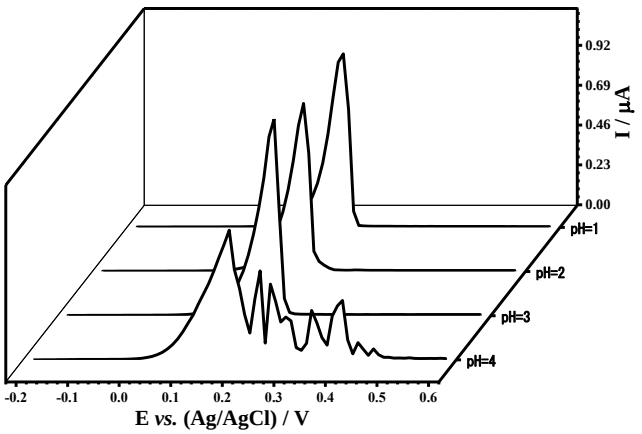

Figure 2.21 Typical curves of copper stripping recorded in Cell 2 for the same experiment performed in Cell 1, with Cell 1a containing 10 µM $Fc(MeOH)_2$ and Cell 1b 0.2 M $CuSO_4$ at distinct pH (from 1 to 4).

Another point likely to influence the analysis on CE is the type of "bridge" connector between Cell 1a and Cell 1b. Different materials were tested, including Pt sheet of different size, Cu wire and a classical salt bridge. As seen from **Figure 2.22**, there is no significant difference for both the charge from current integration on WE1 and that from

$Cu^{(0)}$ stripping from CE1, regardless of the material, the size and the conductor type (ionic or electronic). Therefore, we did not study the effect of "bridge" further in detail and used Cu wire for the entire work. Just to recall that a main consideration of the cell design is to reduce as much as possible the interfacial impedance between the "bridge" and the solutions to ensure that the cell voltage does not exceed the limit of the potentiostat, and that any cell configuration used here (three-electrode cell and two half-cells with either salt of metal bridges) gave exactly the same voltammetric response (**Figure 2.6**).

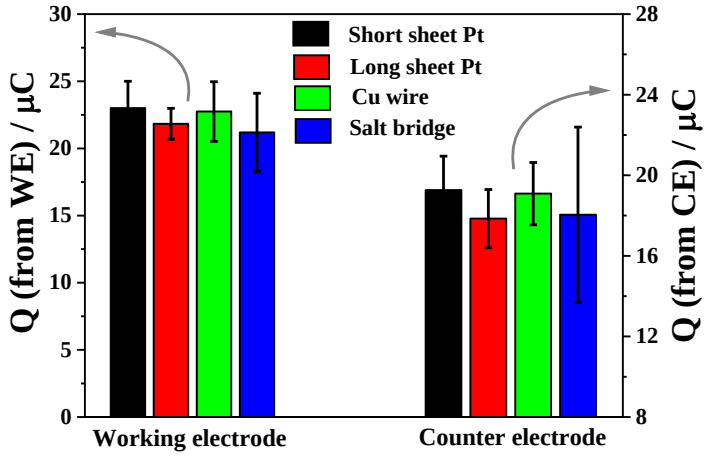

Figure 2.22 Charge from current integration on WE1 and Cu stripping from CE1 under the condition of different bridge connectors (short and long Pt sheets, Cu wire or salt bridge). Cell 1a: 50 µM $Fc(MeOH)_2$; Cell 1b: 0.2 M $CuSO_4$; Potential applied to WE1: +0.3 V (*vs.* Ag/AgCl); Time: 300 s. Error bars indicate the standard deviation of 5 repetitive measurements.

2.4.5 The analytical figures of merit

One already knows that prolonging the duration of applying the constant potential at WE1 leads to increasing overall charge passing through Cell 1, resulting also in increasing charges from CE1 (= WE2) stripping in Cell 2 (**Figure 2.14**). From the analytical point of view, it is now important to examine this "indirect preconcentration analysis" of $Fc(MeOH)_2$ in a lower concentration range. **Figure 2.23** shows that the charge from both current integration on WE1 and Cu stripping on CE1 (= WE2) increases with the electrolysis time at +0.3 V in Cell 1 in the presence of $Fc(MeOH)_2$

at 3, 6 and 10 µM, respectively, whereas the absence of probe (blank) leads to zero stripping charge as recorded from counter electrode (in comparison to significant background response for direct analysis at the working electrode). This confirms that $Fc(MeOH)_2$ can also be indirectly "pre-concentrated" with time, indirectly through the electrodeposition of Cu on CE1 during its oxidation. Therefore, the concept of stripping may also be applicable here, and one may eventually analyze lower concentration of analyte by increasing the time. It allows a trade-off between the time and sensitivity of analysis.

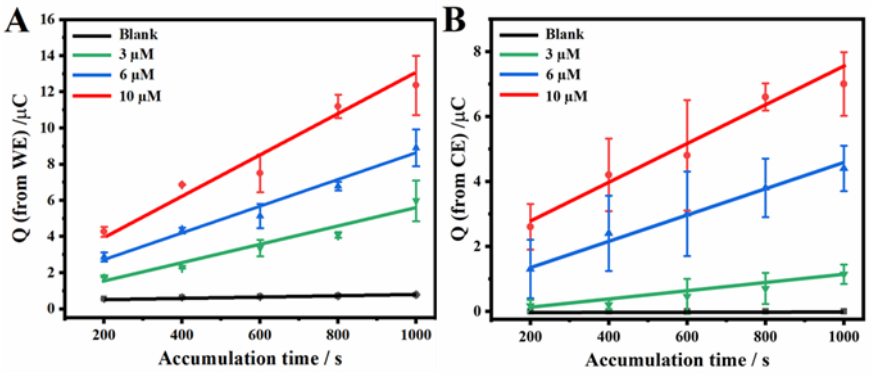

Figure 2.23 Variation of charge as a function of accumulation time (by applying +0.3 V to WE1 for increasing times in blank or 3, 6 or 10 µM $Fc(MeOH)_2$ solutions in Cell 1a), measured from current integration on WE1 in Cell 1 (A) and Cu stripping from CE1 (=WE2) in Cell 2. Error bars indicate the standard deviation of 5 repetitive measurements.

As an analytical method, it is important to establish a calibration curve for different concentration of analyte under fixed analytical conditions. Here, +0.3 V *vs.* Ag/AgCl was applied to WE1 for 800 s, with concentration of $Fc(MeOH)_2$ in Cell 1a from 0 to 10 µM, and 0.2 M $CuSO_4$ at pH 2 in Cell 1b. Two signals are considered for analysis: charge from current integration during the oxidation of $Fc(MeOH)_2$ in Cell 1a, and charge from Cu stripping of CE1 in Cell 2. **Figure 2.24A** shows clearly different slopes for low concentrations, up to 1 µM, and for the concentration range from 1 to 10 µM. The blank solution also shows a signal of *ca.* 1 µC, which is very close to the signals from 0.1 and 0.2 µM solutions. This blank signal arises from the non-Faradaic current, and is dominant in the solutions with low concentration of analyte, restricting the detection limit down to 0.4 µM for such direct detection. Meanwhile, **Figure 2.24B** shows better linearity over the whole concentration range. Even at low concentration,

the signals are still clearly distinguishable and analysable by fitting, with a limit of detection (LOD) estimated at 0.1 µM (LOD=3S_a/b, where S_a is the standard deviation of the response (n=5) and b is the slope of the calibration curve). With such optimal conditions, the blank signal is not detectable when measured by anodic stripping at the CE. These phenomena make the Cu stripping signals from CE1 more favourable for analysing low concentrations of $Fc(MeOH)_2$. This is likely because the CE may serve as a filter for non-Faradaic charge. Finally, we also tested stirring the solution in Cell 1a (in order to accelerate mass transport of $Fc(MeOH)_2$) and, besides noisier amperometric response, this resulted in an increase of sensitivity (stripping peaks almost 5 times larger than in quite solution, see **Figure 2.25**), but it does not contribute to lower LOD.

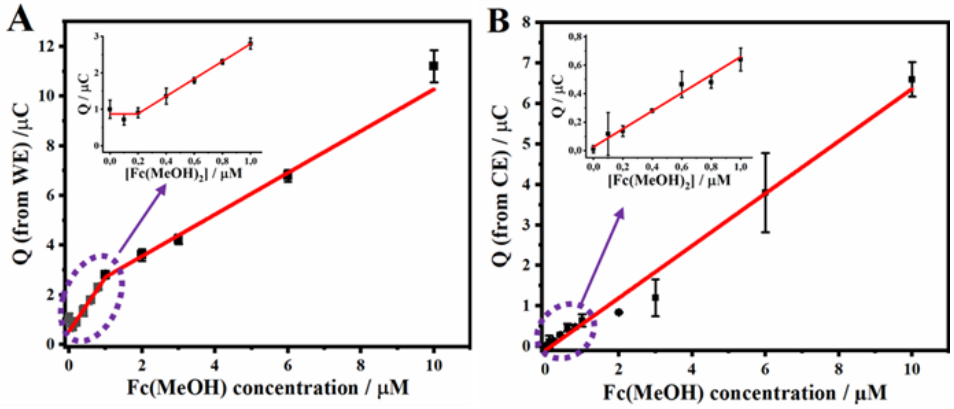

Figure 2.24 Calibration curves obtained from (A) working electrode and (B) counter electrode for detection of increasing concentrations of $Fc(MeOH)_2$ in Cell 1a; potential applied to WE1: +0.3 V vs. Ag/AgCl, for 800 s; solution in Cell 1b: 0.2 M $CuSO_4$ at pH 2; error bars indicate the standard deviation of 5 experiments. Inset graphs show the enlarged calibration curves of $Fc(MeOH)_2$ in the concentration range from 0 to 1µM.

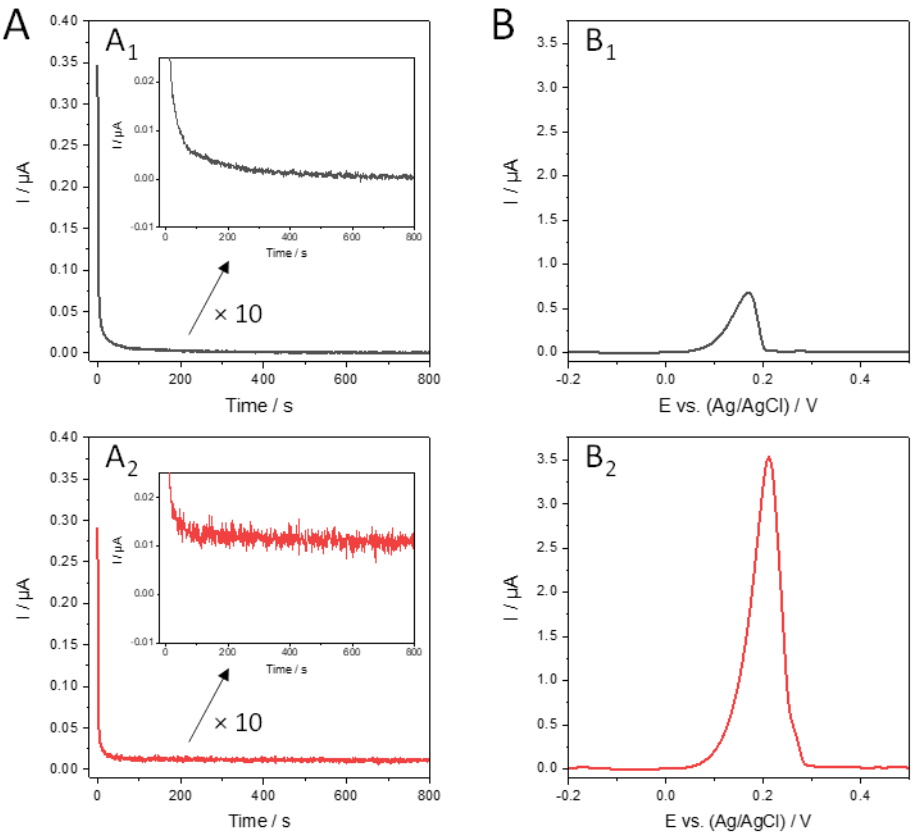

Figure 2.25 (A) chronoamperometry of GCE in 6 µM $Fc(MeOH)_2$ in cell 1a (without (A_1) or with (A_2) stirring) at an applied potential of +0.3 V; (B) Corresponding anodic stripping of $Cu^{(0)}$ deposited on CE1; Cu^{2+} concentration in Cell 1b: 0.02 M; "bridge" connector: Cu wire.

A major advantage of stripping analysis is that one may play with the "accumulation" time in finding a compromise between signal sensitivity and detection limit. In this work, from all the figures, it is seen that the charge from Cu stripping on CE1 (= WE2) is always lower than that from direct integration of current from WE1. This leads to a decrease in the apparent sensitivity fitted from **Figure 2.24**. Nevertheless, we would stress that the charge is already a processed signal, while the raw signal is the current. From **Figure 2.10**, it is clearly seen that the current from stripping is much higher in absolute value than that from either LSV or chronoamperometry. This makes the measurement more accurate, with the current signals more resolved from noise. It may explain the advantage in determining low concentrations as shown in **Figure 2.24**. Of course, for such reversible redox probe used here as model analyte, the method cannot

compete with classical differential pulse voltammetry (with LOD of 0.17 µM, **Figure 2.26**) in terms of analysis speed, but it might be of interest for electroanalytical schemes involving very slow recognition/detection events, such as those encountered with molecularly imprinted electrodes, for instance. This would also contribute to induce more selectivity to the detection, which is here only related to the oxidation potential applied in Cell 1a.

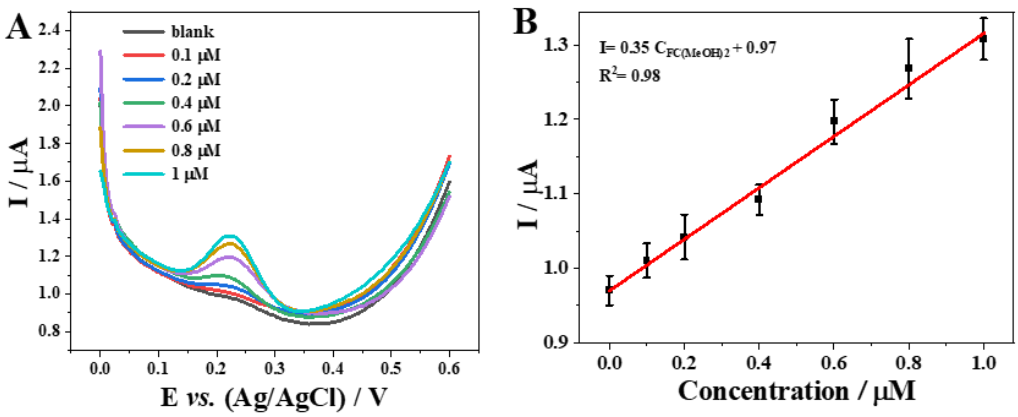

Figure 2.26 (A) Differential pulse voltammograms and (B) corresponding calibration curve for the direct determination of $Fc(MeOH)_2$ in a three-electrode cell.

In order to show that the method can be useful for determining other compounds, we tested it for another analyte (*i.e.*, gentisic acid, an antioxidant molecule used in pharmaceutical industry [45]) by performing preconcentration for 300 s, either in stirred or non-stirred media (**Figure 2.27 A**). The calibration curves obtained in the sub-µM concentration range (**Figure 2.27 B**) confirm the trends observed for $Fc(MeOH)_2$ redox probe, with a sensitivity improved by ca. 4 times when stirring the solution in Cell 1a containing the gentisic acid analyte. LOD values determined from measuring the stripping signals from CE1 were 0.03 µM and 0.04 µM, respectively with and without stirring; they are lower than for $Fc(MeOH)_2$, most probably because gentisic acid is likely to adsorb on electrode surfaces [46] thus contributing to more effective preconcentration.

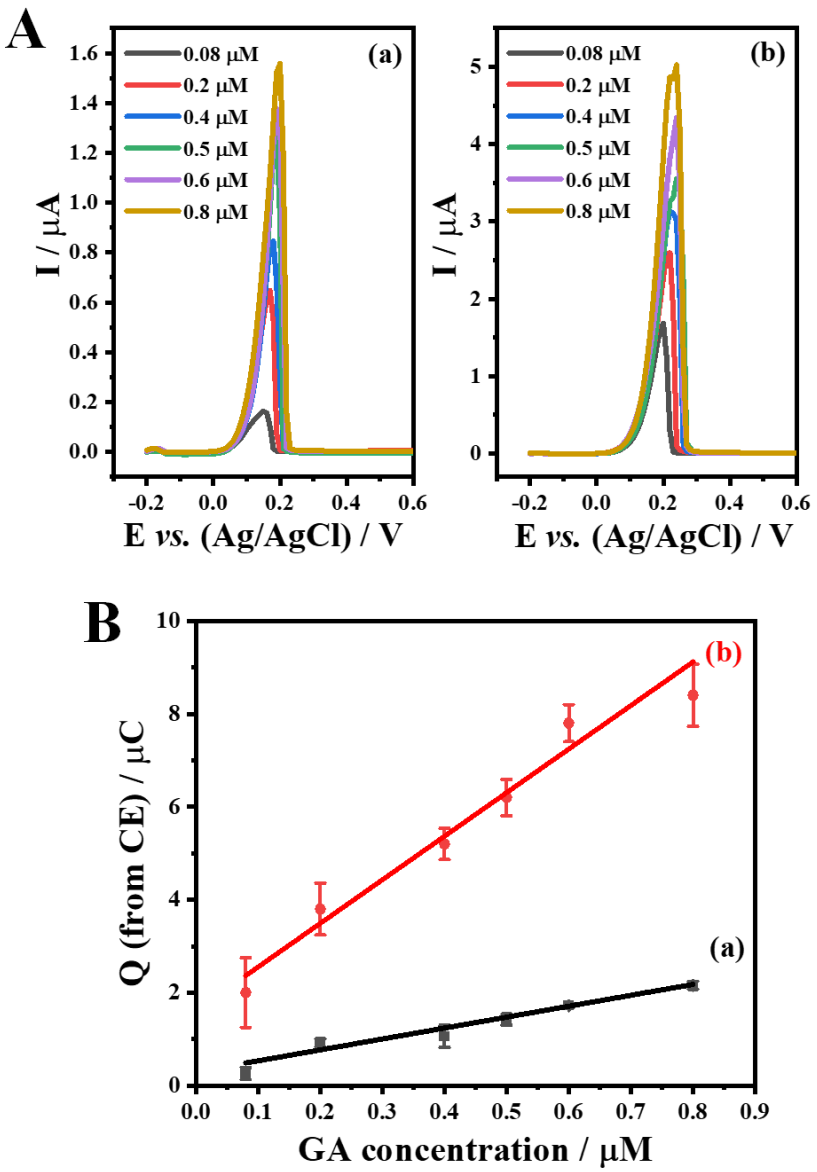

Figure 2.27 Anodic stripping signals recorded at counter electrode after transfer to Cell 2 (A) and corresponding calibration curves (B), for detection of increasing concentrations of gentisic acid (GA) from 0.08 to 8 µM in Cell 1a, respectively without (a) or with stirring (b); potential applied to WE1: +0.3 V vs. Ag/AgCl, for 300 s; solution in Cell 1b: 0.2 M $CuSO_4$ at pH 2; error bars in (B) indicate the standard deviation of 3 experiments.

2.5 Conclusion

In summary, we report a new method of electrochemical stripping analysis for target analytes that do not deposit or adsorb on the working electrode. This is achieved by capturing the stripping signals indirectly from counter electrode, from a metal deposit formed while oxidizing the analyte. An electrochemical cell is designed, with the working electrode and analyte in one compartment (Cell 1a) and a micro-disk counter electrode and Cu^{2+} species in another compartment (Cell 1b). The two compartments are connected with a metal or ionic "bridge". By applying an oxidative potential on working electrode, the analyte in Cell 1a is oxidized while Cu^{2+} is reduced and deposited on the counter electrode. The latter is then transferred to another cell (Cell 2) for determining by anodic stripping the amount of previously deposited $Cu^{(0)}$, which is related to the current flow through Cell 1 and thus indirectly reflects the concentration of analyte. Instead of classical counter electrodes with large surface area, a micro-disk counter electrode is purposely selected for high polarization and low non-Faradaic charging. The effect of the size of counter electrode, the Cu^{2+} concentration and pH of the solution in Cell 1b, and the "bridge" connector were systematically studied. With optimal conditions, the $Cu^{(0)}$ stripping charge from the counter electrode shows good linear relationship with the concentration of the model analyte ($Fc(MeOH)_2$) used here in Cell 1a, which was also confirmed for another analyte (gentisic acid). This method has merits in improving the resolution of current, as the stripping current (peak) is much more clearly defined than the differences in currents sampled during the direct oxidation of the probe. Besides, it may also reduce the background signal from blank solution by "filtering" the background signal (resulting from noise and non-Faradaic charge). Like in classical electrochemical stripping analysis, one may also prolong the oxidation ("accumulation") time or stir the preconcentration solution to enhance performance of analysis. This work extends the applications of stripping analysis and offers new possibilities for electroanalysis by capturing signals from counter electrode.

Chapter III

Visualization of working electrode reactivity from an electrochromic counter electrode

3.1 The concept

Apart from the concentration of analyte, another target of analytical chemistry is the reactivity of materials. In electroanalytical chemistry, it is particularly interesting to study the charge transfer kinetics of electrochemical interfaces. In this chapter, we attempt to develop the concept of visualizing electrochemical reactions on WE indirectly through the optical change of the CE. The principle is illustrated in **Figure 3.1**. By positioning the CE purposely close to the WE, the current distribution on CE is influenced by that on WE, thus may reflect the distribution of reactivity of WE.

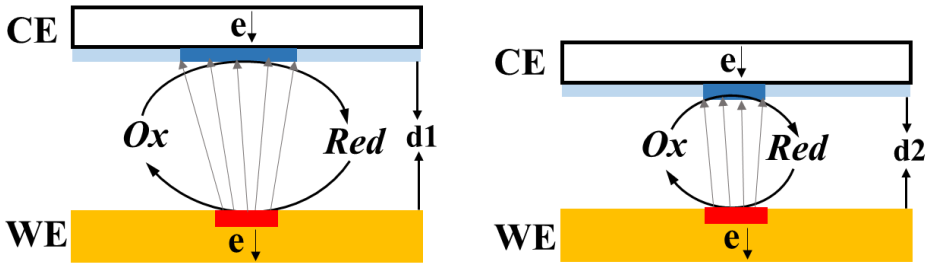

Figure 3.1 Illustration of current distribution (grey line) inducing colour change on CE (dark blue) by an active area on WE (red). The distance between WE and CE: d1 >d2.

Generally, two effect can be envisaged for such system. One is the distribution of electric field in the electrolyte. This is dominant when the electrolyte is weakly supported, having high resistance. In short, the ions prefer the shortest path from WE to CE, thus the current distribution on WE can be approximately "duplicated" to CE. Another effect is the mass transport of redox species. This is like positive feedback SECM, where the product of the reaction on WE reaches CE and gets "recycled" to form reactant that transports back to WE. At the same time, the electrochromic reaction of CE serves as mediator for the charge transfer. Apart from diffusion, migration may also be considered for charged redox species as the two electrodes are positioned close.

All these make it feasible for the visualization of WE reactivity from an electrochromic CE.

3.2 Experimental section

3.2.1 Preparation of different types of electrodes

Preparation of WO_3/ITO. The WO_3 electrochromic CE was prepared by electrodeposition on ITO (Thickness: 0.5 mm, sheet resistance: 10 ohm/sq, area: 15 × 15 mm^2, SPI Supplies, France) from peroxo-tungstic acid (PTA) solution. The latter was prepared by dissolution of 1.8 g of W metallic powder in 20 ml of H_2O_2 and 20 mL of deionized water [251]. The mixture was constantly stirred for 24 h in a cold bath (between 0 and 10 °C). Then, 0.05 g of Pt/C powder was added into the colorless solution to catalyze the decomposition of excess H_2O_2 under string until obtaining a yellow-colored solution. Next, the obtained PTA solution was further centrifuged at 7000 rpm for 8 min in order to remove the precipitate, while the supernatant was recovered and kept in the refrigerator for further use. The electrodeposition was carried out in a conventional three-electrode system, with ITO as WE, an Ag/AgCl commercial RE, and a Pt wire as CE. Before electrodeposition, the ITO surface was cleaned by sonication in acetone, ethanol, $H_2O_2/NH_3{\cdot}H_2O$ (2:1 *vol.* ratio) and water. The WO_3 film was electrodeposited by scanning cyclic voltammetry between 0 and -0.6 V (*vs.* Ag/AgCl) at a scan rate of 2 mV/s for 10 cycles. After electrodeposition, the film was rinsed with water and dried in air. The as-prepared WO_3 film showed dark blue color due to the electrochemical reduction, but it rapidly bleached after a few seconds of exposure in air. The WO_3-coated ITO was stored under ambient condition for use.

Preparation of polyaniline film on ITO (PANI/ITO). The PANI electrochromic CE was prepared by electrodeposition on ITO in 1 M HCl solution containing 0.1 M aniline (purified by distillation)[268]. The processed ITO glass, a Pt sheet, and an Ag/AgCl were used as the WE, CE and RE, respectively. PANI was electrodeposited on the surface of ITO glass by cyclic voltammetry method at between -0.2 and 0.8 V (*vs.* Ag/AgCl) at a scan rate of 10 mV/s for 20 cycles. Finally, PANI/ITO was rinsed with deionized water and ethanol for several times to remove aniline monomer and oligomer PANI, and dried in an oven at 60°C for 4h.

Preparation of (3,4-ethylenedioxythiophene): poly(styrenesulfonate) thin films on ITO (PEDOT: PSS/ITO). The PEDOT: PSS film deposition was done by spin-coating on ITO glass substrates with a spin speed of 5000 rpm for 30 s. Before deposition, the ITO should be cleaned carefully (cleaning ITO operation has been introduced in the section for the preparation WO_3/ITO), and the PEDOT: PSS solution should be sonicated for at least 20 min.

The preparation of working electrode. The WE studied include interdigitated Au electrodes (200 µm band with 200 µm gap, Metrohm), Au-disk array on ITO and Au microelectrode array. The Au-disk array was deposited by sputtering Au on masked ITO for 120 s at 35 mA current to achieve thickness of *ca.* 60 nm (Quorum sputter coater, Q150 TS). The mask was printed on a SLA 3D printer (Asiga) with 200 µm diameter holes, and was removed after sputtering. The Au microelectrode array was prepared by sealing Au wires (25 µm diameter, 99.9%, ChemPur, Germany) in UV-cured resin. First, the structural body of the array with holes of *ca.* 150 µm diameter was 3D printed from UV DLP resin. The Au wires were then inserted in the holes under stereomicroscope, and the holes were closed by filling the same resin for printing. Afterwards, the structure was cured in UV for at least 1 hour. The electrical connection of the Au wires was made by attaching to a Cu sheet with silver epoxy (M.G. Chemicals, UK). The final step was to polish the Au microelectrode array up to 0.1 µm abrasive disc (Buehler, USA) to ensure a smooth surface with Au wires well exposed.

3.2.2 Electrochemical cell assembly for optical imaging

The electrochemical cell consists of a planar WE (interdigitated electrode, microelectrode array, and Au deposit on ITO), a WO_3-coated ITO as CE, and water as electrolyte. The details of WE and CE are detailed in 3.2.1. The WE and CE are separated by a polytetrafluoroethylene (PTFE) spacer (GoodFellow, UK) to control the distance (0.005 − 0.1 mm). This would get rid of potential interference from the inhomogeneity of filter paper used in literature [41]. A square hole of 2 mm × 2 mm was made for filling the deionized water electrolyte. The electrodes were pressed and fixed in a 3D printed frame by two magnets (**Figure 3.2A and 3.2B**).

After assembly, the electrochemical cell was placed under optical microscope for imaging. A CMOS camera is synchronized with potentiostat for capturing the dynamic

color change of the CE. The latter is observed to be correlated with the electrochemical reactivity distribution of WE.

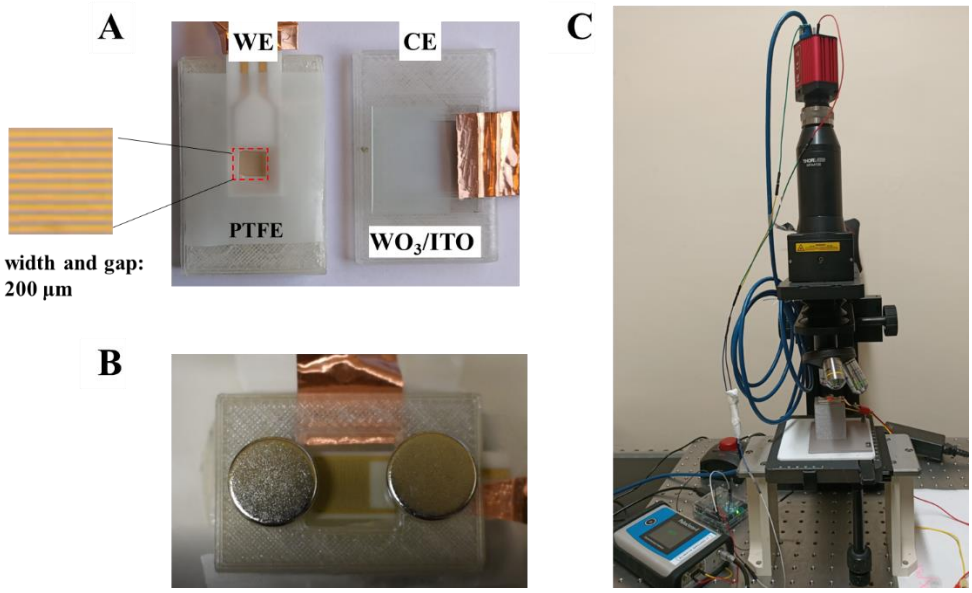

Figure 3.2 The before (A) and after (B) electrochemical cell assembly. (C) The optical imaging system.

The optical imaging system is illustrated in **Figure 3.2C.** A red LED of 623 nm wavelength was used as light source (Thorlabs). The objectives were 4× (NA = 0.10) and 10× (NA = 0.25) from Olympus, Japan. The imaging was carried out by a complementary metal oxide semiconductor (CMOS) camera (Thorlabs, 1919 × 1919 pixels). and a cubic elevator platform to adjust the spatial position of the sample device.

3.2.3 Measurement

Electrochemical and optical measurements were synchronized for visualizing the CE color change upon applying voltage between WE and CE. The voltage was controlled by a potentiostat (PalmSens 4, Netherland). When an electrochemical measurement started, a trigger was sent to Arduino to generate a square wave for triggering the image capture by CMOS camera at desired time intervals. The exposure time of the CMOS camera was 8 ms for each image. In this way, the optical images could precisely reflect

the transient behavior of the electrochemical system. The images were analyzed by ImageJ software.

3.3 Results and discussion

3.3.1 Proof of concept

When the CE is placed close to WE, the reactions on it cannot be neglected and will affect the electrochemical response of the cell. Thus, for analyzing such system, one needs to consider the electrochemical reactions on both WE and CE. Moreover, when the WE and CE are different, either in size or in reactivity, the current distribution shall also be taken into consideration. For example, in direct mode SECM, the microelectrode determines the current distribution on the large-scale substrate and localizes the reactions[38]. Another example is Pt electrocatalyst on carbon substrate. The Pt may locally catalyze the electrochemical oxidation of methanol, yielding higher current density which triggers deeper color change of electrochromic CE [41].

The current distribution can be analyzed by Nernst-Planck Equation, which considers the ohmic drop of electrolyte, the reaction kinetics on both WE and CE, and the mass transport of the reactive species. Depending on the system, it can be simplified by neglecting some of the factors. The simplest case is primary current distribution, which assumes the electrochemical reactions on WE and CE interfaces very fast (Nernst boundary condition) and thus considers only the ohmic drop of electrolyte. The secondary current distribution takes into account the reaction kinetics of WE and CE. In most cases, the kinetics depend on the concentration of reactive species near the electrodes, so the mass transport shall also be coupled. The tertiary current distribution further adds the migration of species, which could be non-negligible when using weakly supported electrolyte.

Here, we demonstrate an example where an interdigitated Au WE is placed in parallel with a WO_3 electrochromic CE. DI water is used as electrolyte. By applying an anodic bias on WE, H_2O is oxidized on WE and WO_3 is reduced on CE. The scheme is shown in **Figure 3.3A**. The reactions are depicted as follows:

at WE: $2H_2O \rightarrow O_2 + 4H^+ + 4e^-$

at CE: $WO_3 + x\ H^+ + xe^- \rightarrow H_xWO_3$

The reduced form H_xWO_3 is blue-colored and can be visualized by naked eyes or under optical microscope. **Figure 3.3B** illustrates the color change of the system during a linear sweep voltammetry scan. At 1.3 V, the current is very low (*ca.* 3.85 µA) and the

WO_3 CE stays transparent. This suggests that the reactions on both WE and CE are negligible. As the applied voltage increases beyond 1.5 V, the current sharply increases and the WO_3 CE starts to turn blue. Moreover, the blue strips on CE fall almost exactly above the Au strips on WE. This indicates that the current distribution on CE follows that on WE. In another word, the shape of WE can be "projected" to CE.

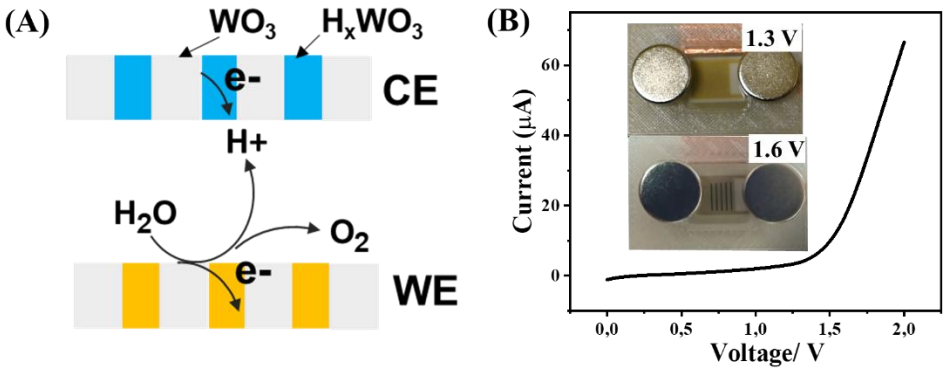

Figure 3.3 (A) Schematic diagram of the reaction mechanism of WE and CE. (B) Linear sweep voltammetry of the electrochromic device from 0 to 2.0 V at a scan rate of 0.05 V/s, the insets: electrochromic photos of CE at 1.3 V and 1.6 V respectively.

3.3.2 The measurement of optical change at CE

The color change of CE was quantitatively measured under optical microscope with a CMOS camera. The electrochemical cell was fixed under optical microscope with the optical focus on the WE. When scanning the voltage from 0 to 2 V (WE *vs.* CE), images were taken at different time, which correspond to different applied voltage thanks to the synchronization. According to the scheme in **Figure 3.4**, the light radiates the WE surface and reflects back to the camera. In the optical pathway, it goes through CE and electrolyte for two times (incite and reflected light). Assume that the optical properties of the WE and the electrolyte do not change during the experiment, the light intensity captured by the camera reflects only the electrochromic effect of the CE. The absorption of CE can thus be derived by dividing the gray value of the colored state by that of the bleached state. In this work, the image taken at 0 V was considered as bleached state for the normalization of gray values. It is seen that the normalized image at 1.3 V shows no strip (**Figure 3.5A**), which is in agreement with no visible color change in **Figure 3.3B**. As the applied voltage increases to 1.6 V, the strips start to appear (**Figure 3.5B**).

This suggests local coloration of the CE in the areas above the Au strips, which differs from those between Au strips. As the applied voltage further increases to 1.9 V, the contrast between colored strips and the gaps becomes higher (**Figure 3.5C**). **Figure 3.5D** shows the variation of normalized gray values across the strips (in horizontal direction in the images). The normalized gray values of the areas above Au strips decrease as the applied voltage increases, indicating that the absorption of WO_3 CE increases. Although the normalized gray values of the areas above gaps between Au strips also decrease obviously after 1.6 V, it could be neglected compared to the normalized gray values of the strips. Moreover, the width of the colored strips is almost identical to that of the Au interdigitated electrodes. This indicate that one may identify conductive areas of WE from the local color change of electrochromic CE.

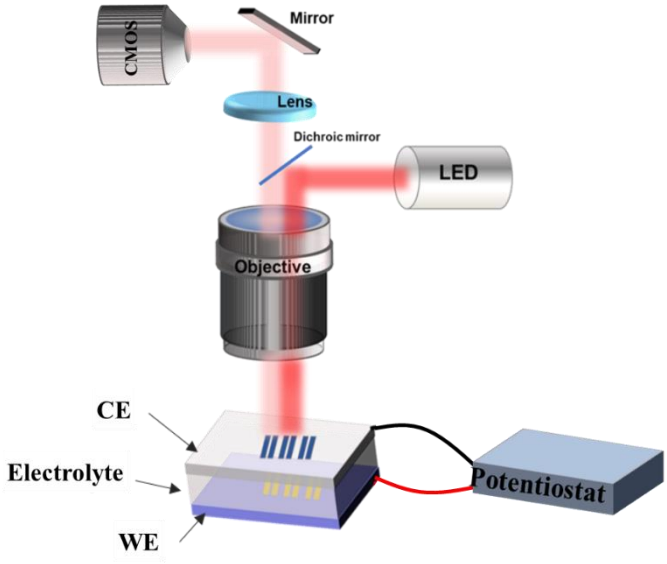

Figure 3.4 Schematic of the experimental setup.

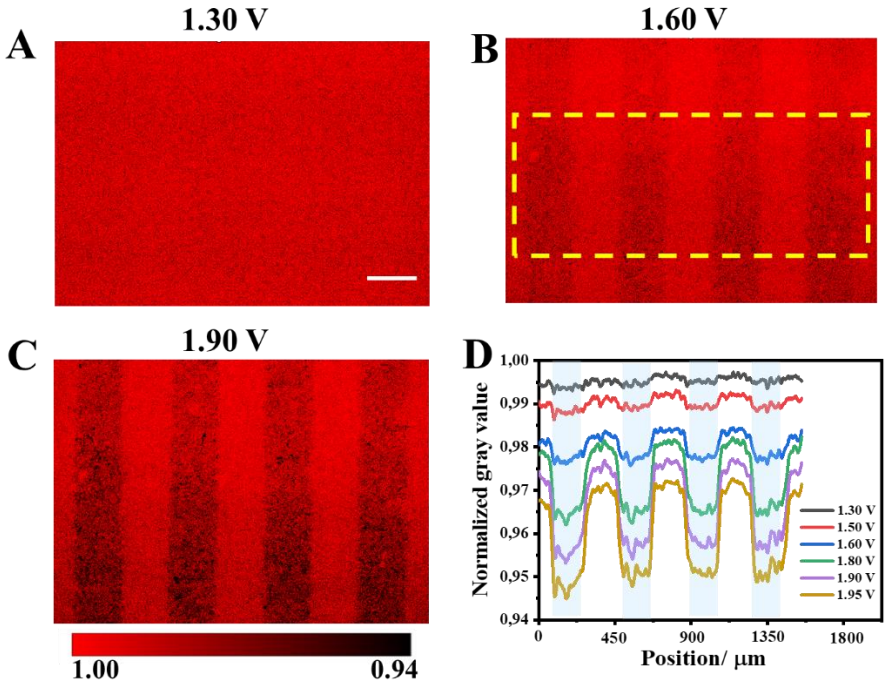

Figure 3.5 (A−C) the optical intensity changes on the CE at voltage for 1.30 V, 1.60 V and 1.90 V, respectively. Scale bar (white): 200 µm. (D) The variation of normalized gray values across the strips and gaps in the yellow dotted frame in **Fig. 3.5B** with increasing the voltage.

3.3.3 The factors affecting local coloration of CE

The color change of CE was also measured as a function of time by applying a constant voltage between WE and CE. **Figure 3.6 (A−B)** shows the images captured at 1, 5 and 15 s when applying 1.9 V on WE *vs.* CE. It is seen that the normalized gray value of the colored strip, which corresponds to the Au strip on WE, gradually decreases with time. Moreover, the areas above the gap between Au strips also start to be colored after *ca.* 5 s (**Figure 3.6A**). Considering that the distance between WE and CE is 25 µm, even 1 s would be sufficient for the H^+ generated on WE diffusing to the CE. Thus, the enhancement in coloration with time is likely related to the kinetics of WO_3 coloration on CE, which is known to be relatively slow in the order of a few seconds [269]. However, as the coloration of WO_3 is driven by intercalation of H^+ in the film, the lateral propagation of H^+ may result in the expansion of colored strips at long time. This may explain the decrease in the normalized gray values, or the increase in coloration, of the gap with time (**Figure 3.6C**).

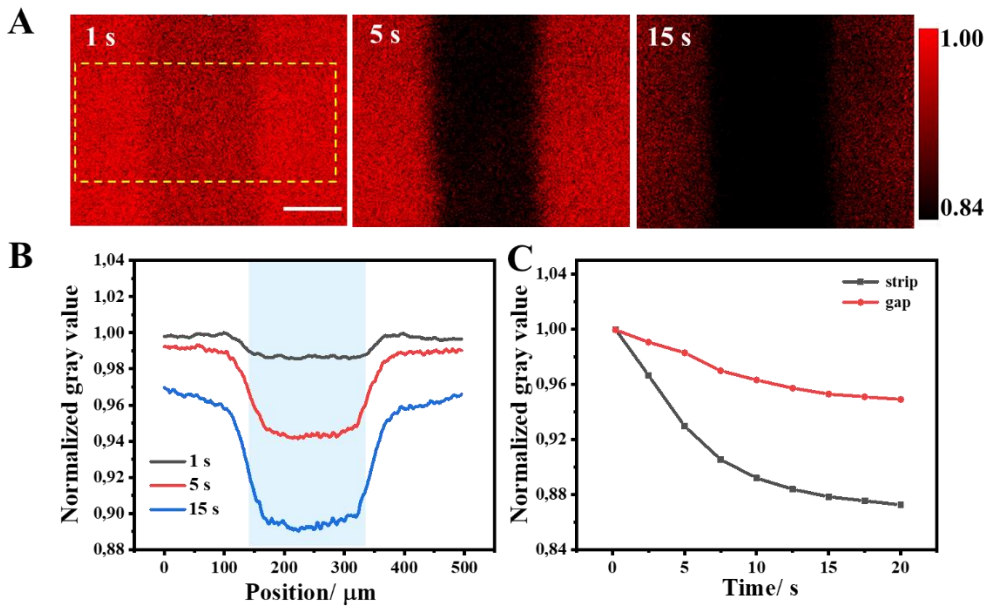

Figure 3.6 The effect of time on the color change on the CE under a voltage of 1.9 V. (A) The color change images of CE at different time. Scale bar (white): 100 μm. (B) The variation of normalized gray values across the regions in the yellow dotted frame in **Fig. 3.6A** at different times. (C) Normalized gray values of strip and gap on the CE as a function of time.

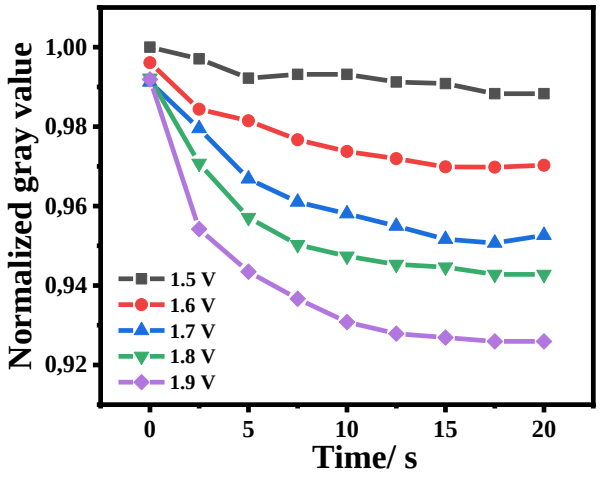

Figure 3.7 The variation of normalized gray values of stripe with time at different voltage across the regions in the yellow dotted frame in **Fig. 3.6A**.

In addition, we also study the variation of normalized gray value for the stripe on the CE with time at different voltage. As shown in **Figure 3.7**, the normalized gray value decreases with time increasing in various constant voltage, however, the greater the applied voltage on the electrochemical cell, the more obvious the reduction of gray value. It can also be seen clearly that the gray value decreases very obviously within 5s, whether the electrochemical cell is applied on low (1.5 V) or high voltage (1.9 V), after 10 s, the gray values tend to remain stable due to lateral diffusion of the H^+ to gap regions. Therefore, choosing suitable time and voltage for optical change of CE is important.

As the local color change on CE is determined by the current distribution in the electrochemical cell, the distance between WE and CE plays an important role. **Figure 3.8(A, B)** shows the images taken at 1.5 V for 5 s with different thickness of spacer. It can be seen that with a distance of 0.2 mm from WE and CE, there is no visible stripe on CE (**Figure 3.8A**), while reducing the thickness of PTFE, stripe can appear on the CE (**Figure 3.8B**). Moreover, the current response decreases as the WE-CE distance increases (**Figure 3.8C**), which could be explained by the resistivity of the electrolyte as well as the hindrance of mass transport of H^+. At the same time, the normalized gray value of the strips on CE increases towards 1 with the increase in distance at a voltage of 1.5V (**Figure 3.9A**), meaning that the color change of CE becomes less significant. Although the normalized gray value of the strips on CE decreases away from 1 at larger distance as increasing the voltage, the normalized gray value of the gaps beside the stripe also decreases (**Figure 3.9A and 3.9B**). This suggests that WE and CE being close is more favorable for projecting the current distribution on WE to CE.

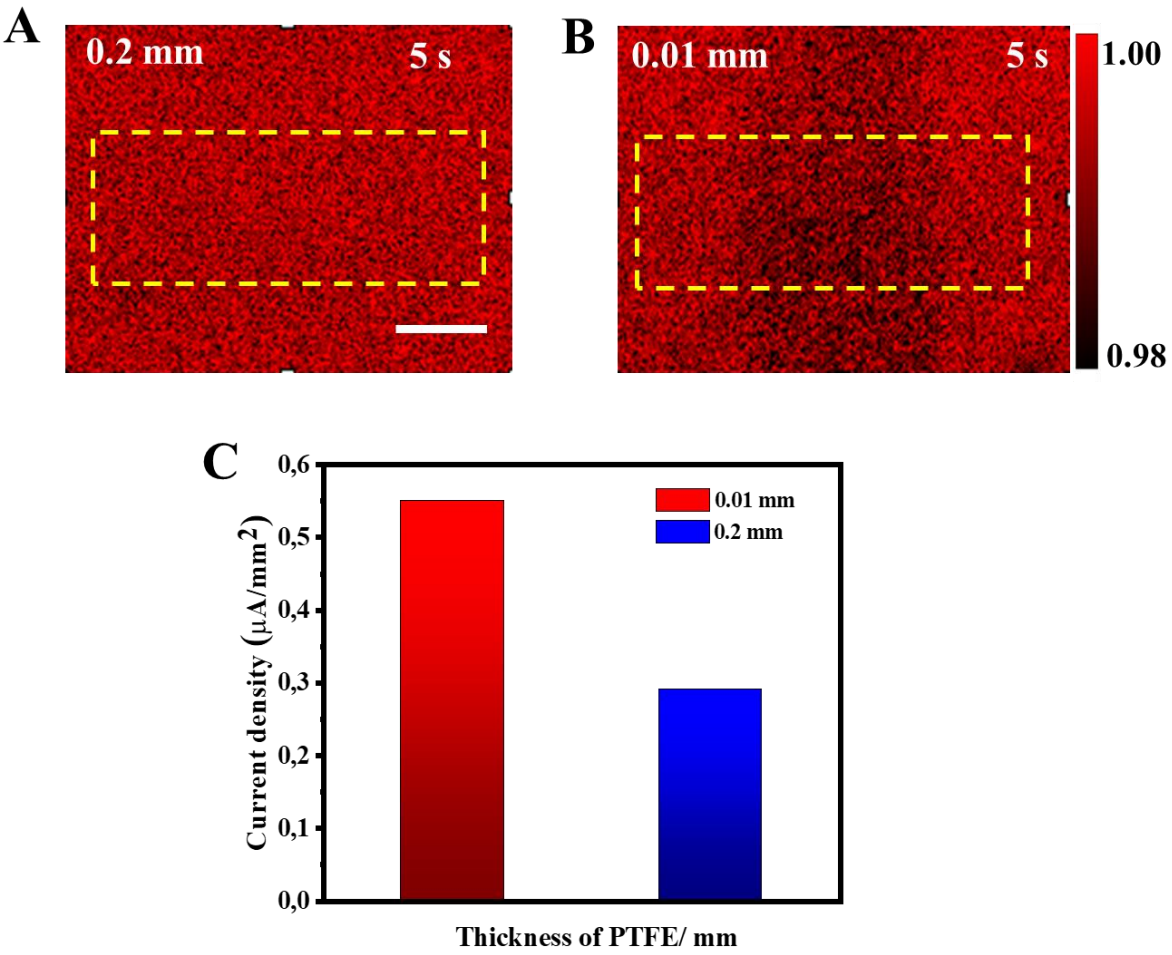

Figure 3.8 The effect of distance between WE and CE on the optical change of CE. (A), (B) The images for optical change of CE at thickness of PTFE for 0.2 mm and 0.01 mm, respectively. Scale bar (white): 100 μm. (C) The current density of electrochromic device for different thickness of PTFE: 0.2 mm and 0.01 mm. The voltage: 1.5 V and time: 5 s.

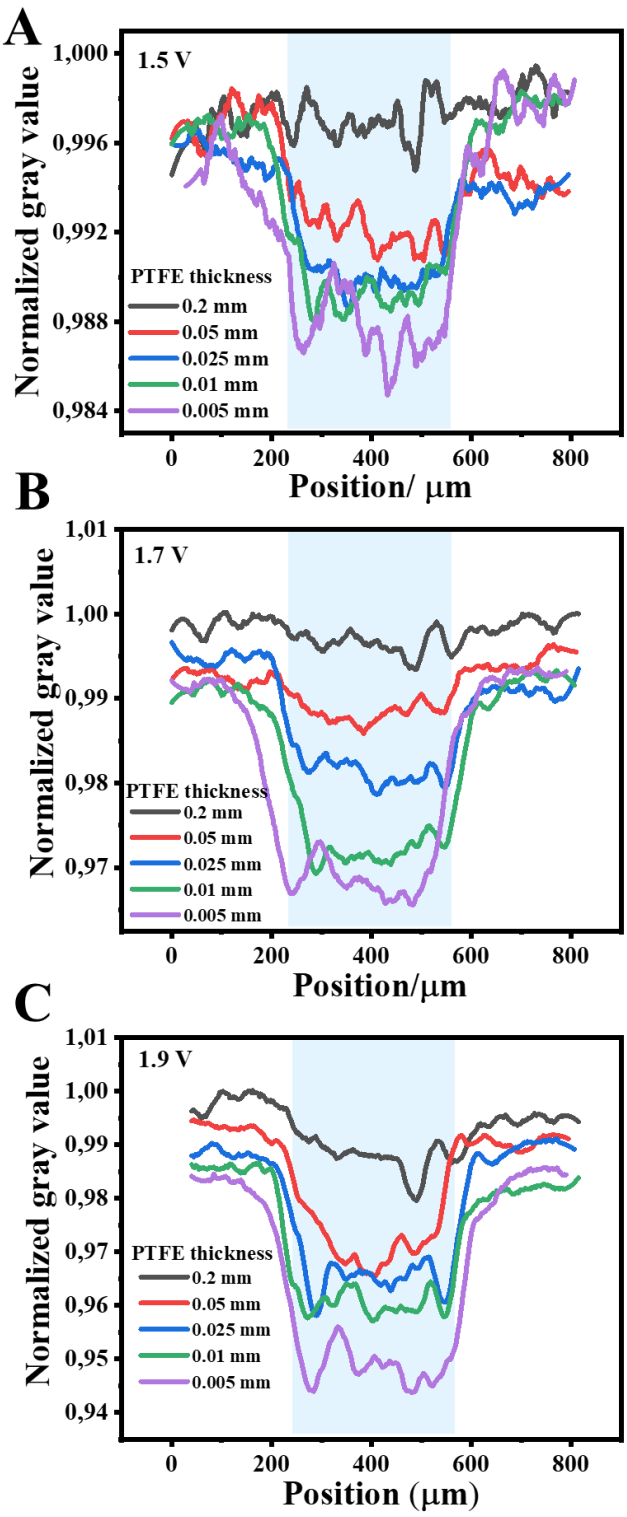

Figure 3.9 The variation of normalized gray values across the regions in the yellow dotted frame in **Fig. 3.8** at different thickness of PTFE: the constant voltage: (A)1.5 V, (B) 1.7 V, and (C) 1.9 V, respectively. The time: 5s.

The CE coloration reaction is also studied using different kinds of electrolytes (Li_2SO_4, Na_2SO_4, LiCl). Here, we use a phone camera to capture the coloration reaction on the CE to be more intuitive. The surface of the CEs both exhibits several blue stripes at 1.8 V for 5 seconds when 0.01M of Li_2SO_4, Na_2SO_4 are used as the electrolyte, respectively (**Figure 3.10A**). Moreover, there is also a slight coloration between these striped gaps on the CE compared with water-based electrolytes. The reason might be that lateral dispersion of current in the solution is more homogenous due to a reduction of the electrolyte resistance. Own to the stronger supporting electrolyte, the coloration of WO_3 directly comes from the intercalation of the Li^+, Na^+. Thus, migration of H^+ to CE that is released from the oxidation of water catalyzed by the WE at a positive bias is weakened. This also means that it isn't beneficial for localizing the current distribution on CE. It is worth noting that the coloration distribution on the CE is more homogeneous as Li_2SO_4 as an electrolyte than that of Na_2SO_4 solution as an electrolyte. It is probably due to the smaller radius of Li^+ compared to Na^+ that makes them easier to insert into WO_3 at same voltage and time. Actually, the colored WO_3 can be rapidly bleached after a few seconds of exposure in air. However, the pattern containing several deep blue stripes remains on the CE after stopping the applied voltage when LiCl is used as an electrolyte (**Figure 3.10B, picture1**). Meanwhile, the Au interdigital electrode also keeps same pattern as CE (**Figure 3.10B, picture2**). After removing the pattern on the CE by rinsing with water, the WO_3 film on the ITO can keep its original state (**Figure 3.10B, picture3**), which means the pattern is not from the reduction of ITO (the reduced ITO is irreversible and keeps brown)[270]. In the case of PANI/ITO instead of WO_3/ITO as CE, the pattern is also observed on the PANI film and Au interdigital electrode when LiCl is used as electrolyte (**Figure 3.10C**). This is likely because the oxidation of a gold interdigital electrode in chloride solutions at anodic bias results in a marked increase in the rate of dissolution of the metal by virtue of the increased stability of Au(I) and Au(III) chloro-complexes[271]. The gold complexes could diffuse quickly to the CE due to the small distance between the WE and the CE. Therefore, the electrolyte containing chloride easily damages the Au interdigital WE which is adverse for the local coloration reaction of CE. Because the pattern on the CE has good symmetry with the pattern on the WE, as well as the uniform pattern distribution, it inspires us that perhaps by optimizing the experimental conditions (concentration, voltage, time, *etc*.), it could be used to replicate fingerprints or other patterns fields in the future.

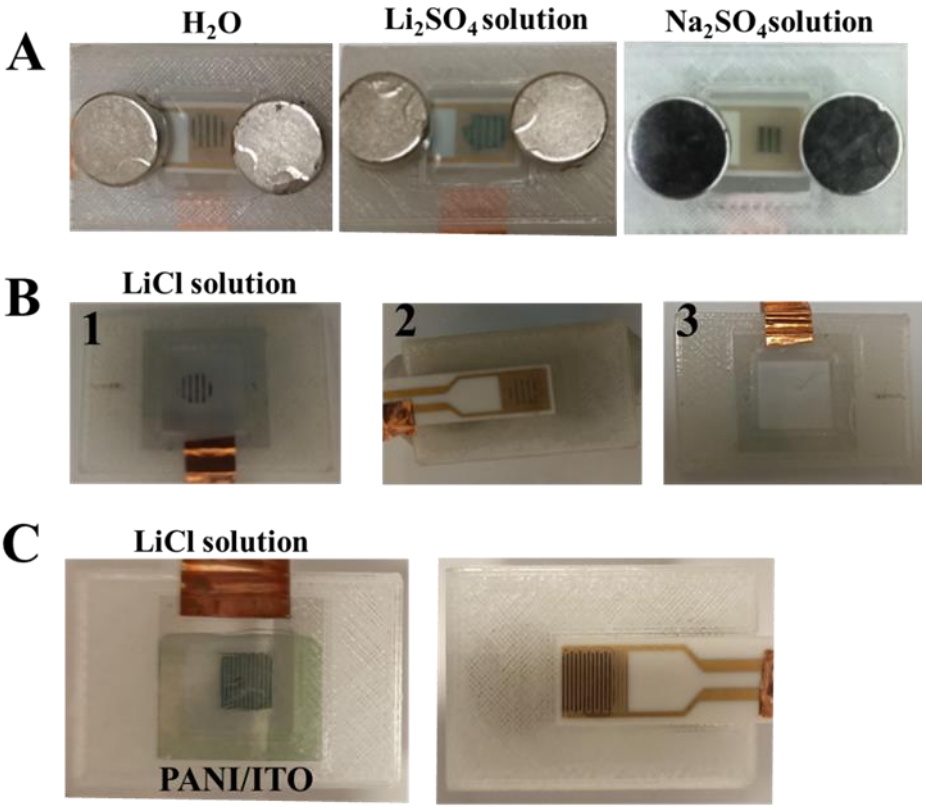

Figure 3.10 The photos for electrochromic of CE at different electrolyte. (A) electrolyte is H_2O, 0.01M Li_2SO_4, and 0.01M Na_2SO_4 from left to right and WO_3/ITO as CE. (B) Electrolyte is 0.01M LiCl and picture1,2,3 represent patterned WO_3/ITO, the locally dissolved Au interdigital electrode, the WO_3/ITO with pattern removed, respectively. (C) Patterned PANI/ITO, the locally dissolved Au interdigital electrode, electrolyte is 0.01M LiCl. All electrochemical cell voltage is carried out at a voltage of 1.8 V and time of 5s.

3.3.4 The study on local reactivity of WE with different substrate

3.3.4.1 WE: Au microelectrode array/resin

The imaging of CE is further challenged with higher spatial resolution using Au microelectrode array as WE. **Figure 3.11A** shows the optical image of the microelectrode array, where each Au microelectrode has a diameter of 25 μm and the gap between adjacent electrodes varies from 20 to 250 μm. By scanning the voltage between WE and CE from 0 to 2 V with 10 μm distance, the current shows a sharp

increase at *ca.* 1.5 V, which corresponds to the onset of electrochemical oxidation of water (**Figure 3.12**). Meanwhile, the color above the areas of Au microelectrodes also starts to change, and the coloration becomes more significant as the applied voltage further increases (**Figure 3.11B**). Note that electrodes 7 and 8, which are located very close (20 µm), become less distinguishable at high voltages (**Figure 3.11C**). This lateral propagation of color is consistent with the observations on Au interdigitated electrodes. It suggests that the distance between adjacent active spots on WE would affect the electrochromic imaging from CE. Experimentally, by controlling proper voltage, it is still possible to visualize 25 µm active electrodes with an insulating gap of *ca.* 20 µm.

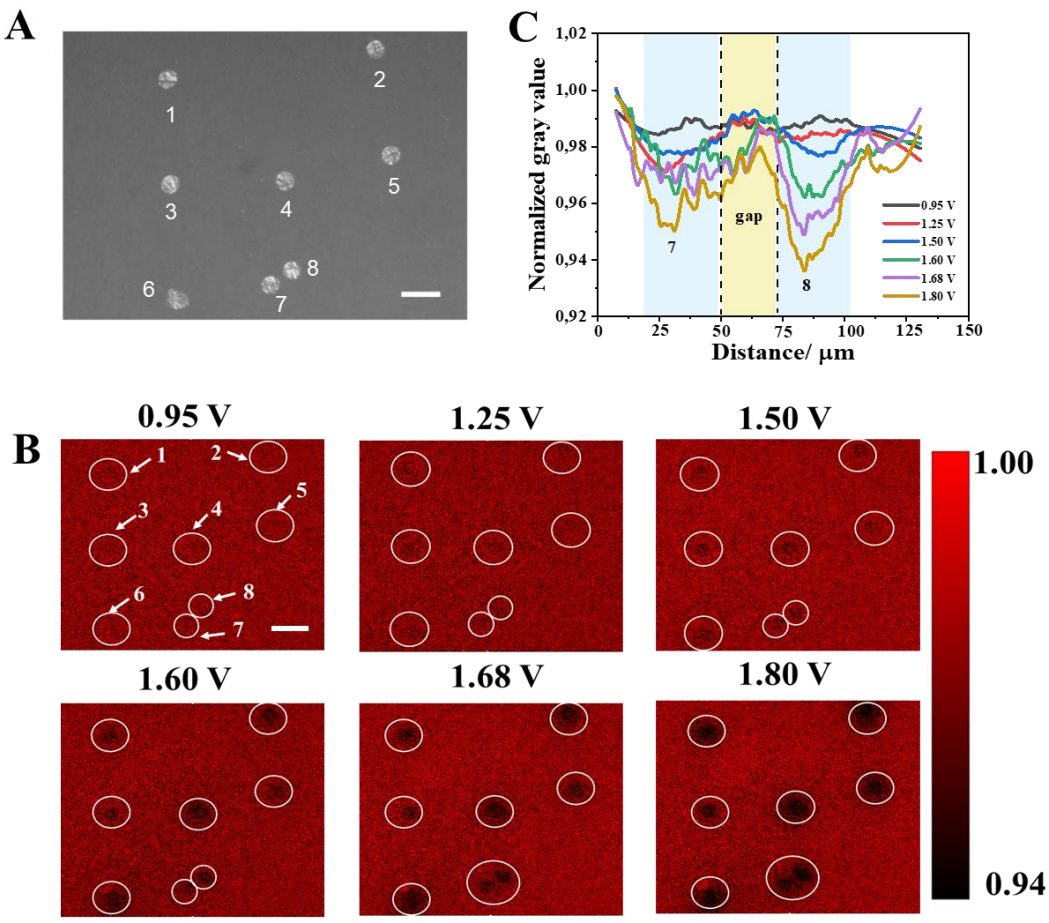

Figure 3.11 (A) Optical micrograph of Au microelectrode array. The scale bar (white): 50 µm. (B) The optical change of CE at different voltage corresponding to the active areas on the WE. Scale bar: 50 µm. (C) The variation of normalized gray value of the region 7, 8, and the gap on CE with increasing the voltage.

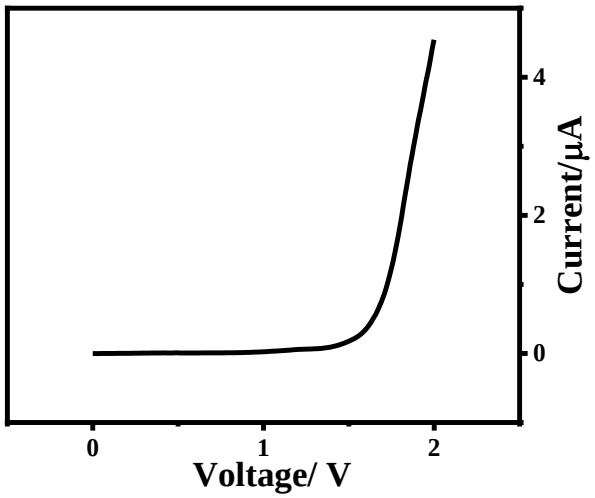

Figure 3.12 Current *vs*. voltage curves of the electrochromic device, scan rate: 0.05 V/s.

3.3.4.2 WE: sputtering Au/ITO glass

The examples above involve WE that is partially conductive. They could be considered as extreme cases where the WE has high contrast between reactive (Au electrodes) and non-reactive (insulator) areas. Here, we demonstrate that the imaging from CE could also be extended to samples with different conductive materials. **Figure 3.13A** shows the photo of WE made of Au disks sputtered on ITO glass. By scanning voltage against a WO_3 CE with 25 μm distance and H_2O as electrolyte, images are acquired as shown in **Figure 3.13B**. After normalizing images with that taken at open circuit voltage (*ca.* 0.005 V), the micro-disks are almost invisible on the CE when the applied voltage is lower than *ca.* 1.0 V. When the voltage rises to *ca.* 1.1-1.3 V, the micro-disks become distinguishable. It is interesting to see that the edges of the disks have lower normalized gray values than the centers (**Figure 3.13C**). This will be discussed later. As the voltage increases to higher than 1.4 V, the color change of CE over the disks is more significant with a decrease in normalized gray value, and it also becomes more uniform. This suggests that higher current is passing through Au than through ITO, which could be related to their different electrocatalytic reactivity for the oxidation of water. However, when the voltage is further increased to 1.8 V, the gaps between Au disks also start to change color. This could be attributed to two possible effects: one is the lateral charge propagation due to higher current and lateral mass transport of H^+, which is similar as

observed from partially conductive samples (**Figure 3.5** and **3.11**); the other is the reduced contrast in electrocatalytic reactivity between Au and ITO, as ITO could also catalyze water oxidation at high potentials.

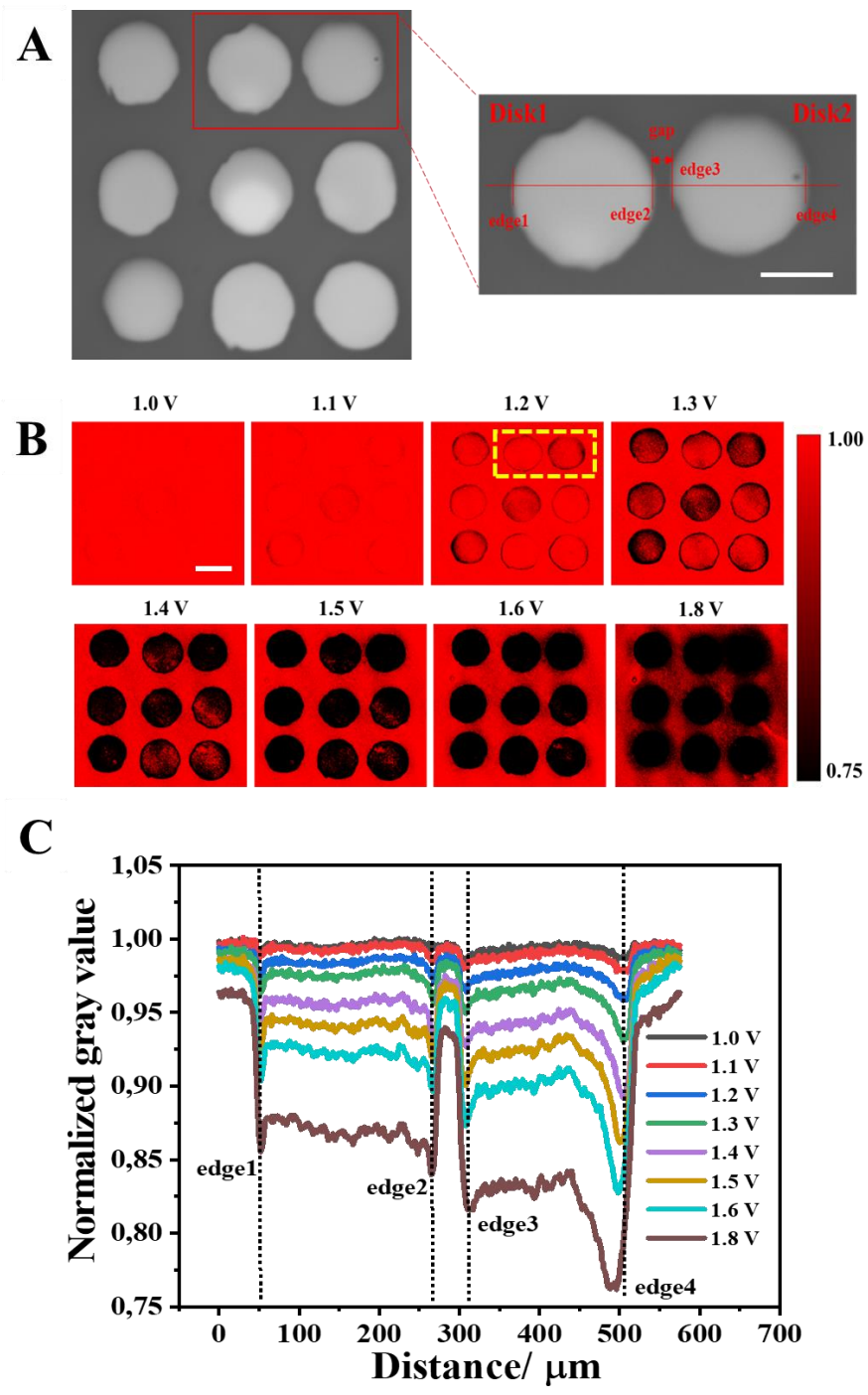

Figure 3.13 (A) Optical micrograph of Au disks sputtered on ITO. Scale bar (white): 100 μm. (B) The optical change of CE with increasing voltage corresponding to the active areas on the WE. Scale bar (white): 200 μm. (C) The variation of normalized

gray value of the two micro-disks on CE (the yellow dotted frame in **Fig. 3.13B**) with increasing the voltage. The edges (1−4) correspond to the edges of the two micro-Au disk on the WE in **Fig 3.13A**, respectively.

Figure 3.14A shows the variation in normalized gray value of gap between two Au disks and the two disks with voltage. The current increases quickly after 1.3 V and at the same time the gray values decrease obviously both the gap and two disks because of polarization reaction on the electrochemical cell. However, as the voltage increases, the gray value difference between the gap and the Au disks gradually increases. Moreover, to ensure that the peak at 1.3 V results from the oxidation of Au on WE, cyclic voltametric (CV) measurements were carried out for three types of electrochemical cell devices, namely: (1) WE: Au disk array/ITO + CE: WO_3/ITO, (2) WE: ITO + CE: WO_3/ITO, and (3) WE: Au disk array/ITO + CE: ITO, by scanning the voltage from 0 to 1.8 V at a scan rate of 0.05 V/s. Compared with the electrochemical cell (2) and (3), the electrochemical cell (1) exhibits obviously redox peaks around 1.40 V and 0.60 V, respectively (**Figure 3.14B**). Moreover, the Au disk array/ITO, ITO and WO_3/ITO as WE (*vs.* Ag/AgCl) in pure water also are studied by scanning CV from 0 to 2.0 V at a scan rate of 0.05 V/s in three electrodes system **(Figure 3.15)**, respectively. However, only the Au disk array/ITO as WE shows an oxidation peak at 1.25 V (**Figure 3.15A**). Therefore, it could be inferred that the oxidation peak in two electrode system (WE: Au disk array/ITO + CE: WO_3/ITO) originates from the oxidation of gold.

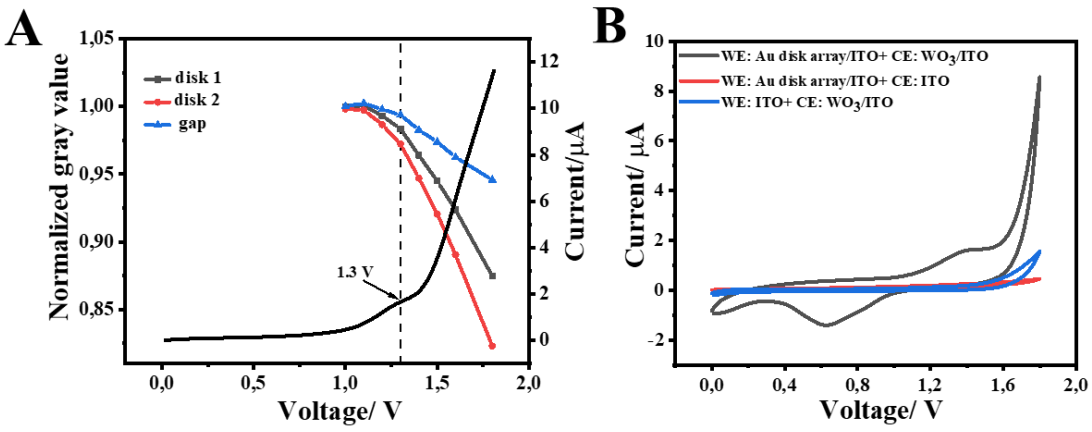

Figure 3.14 (A) Normalized gray value *vs.* voltage curves of Au disk1, Au disk2 and gap (the yellow dotted frame in **Fig. 3.13B**), current *vs.* voltage curves of the electrochemical device, scan rate: 0.05 V/s. (B) Cyclic voltammograms of electrochemical cell at different WE and CE compositions, scan rate: 0.05 V/s.

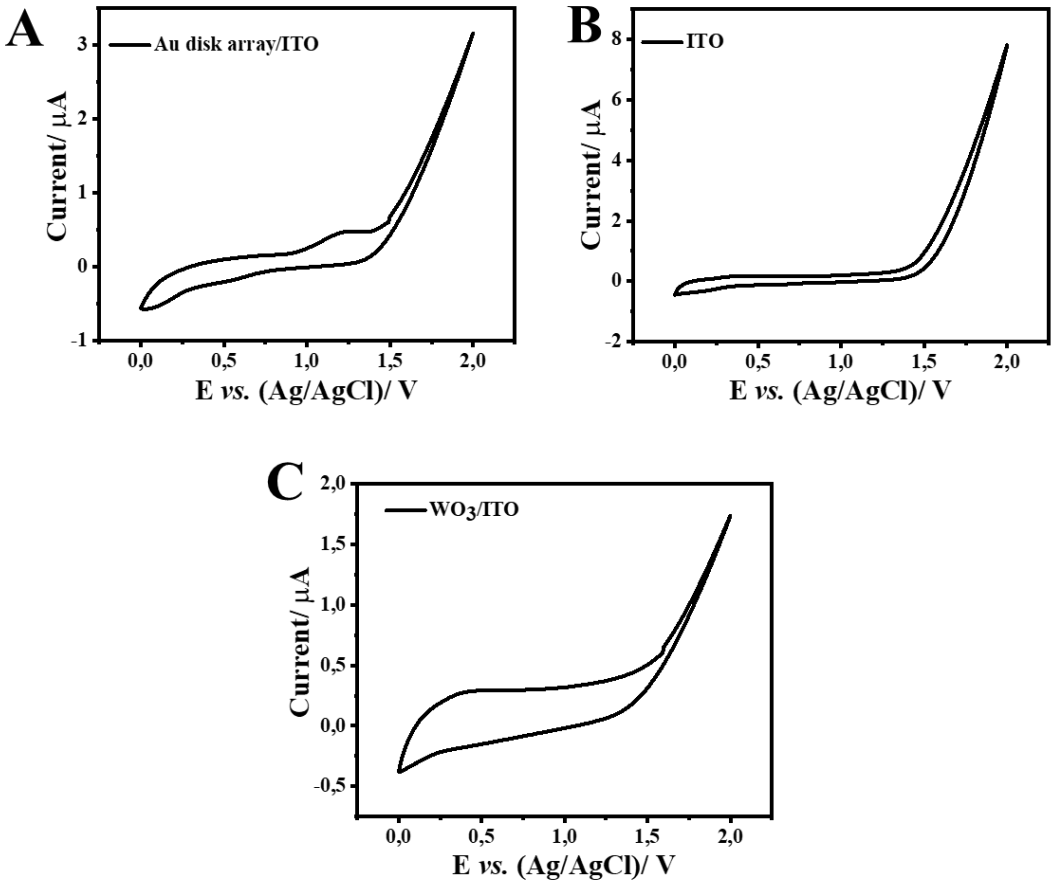

Figure 3.15 Cyclic voltammograms of different types of WEs in pure water at a scan rate of 0.05 V/s. (A) Au disk array/ITO, (B) ITO, (C) WO_3/ITO. Ag/AgCl (saturated KCl) as reference electrode, Pt wire as CE.

In addition, the variation in optical intensity of CE with time at constant voltage also investigated. As a voltage of 1.6 V is applied to this electrochemical cell, the optical image on CE exhibits similar phenomenon with **Figure 3.13(B)**, the edges of the two disks appear firstly at 2s (**Figure 3.16A**) and behave lower normalized gray values than the centers and gap (**Figure 3.16B**). when time increases to 5s, the centers of the two disks are visible, although the normalized gray values are higher than those of the edges. Furthermore, the normalized gray value of the gap also decreases obviously at 15 s due to lateral diffusion of H^+, resulting in less distinguish between two disks. Although the normalized gray value of both gap and disk decrease with time increasing, the difference between them still increases with time (**Figure 3.16C**).

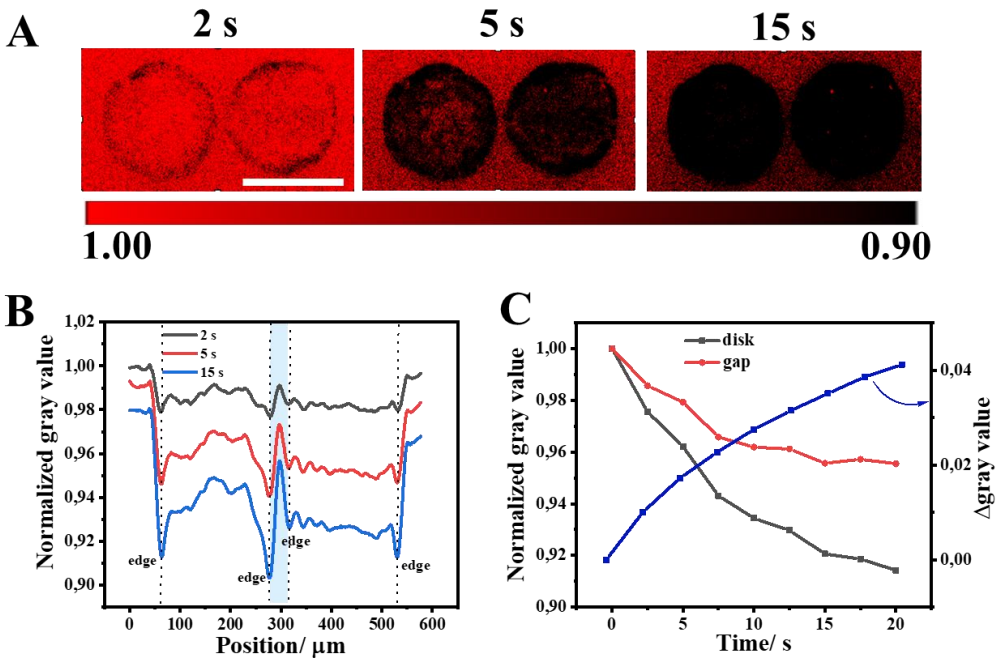

Figure 3.16 (A) The images for optical intensity changes of CE with increasing time corresponding to the active areas on the WE at a voltage of 1.6 V. Scale bar (white): 200 µm. (B) The variation of normalized gray value of the two micro-disks on CE with increasing the time in **Fig 3.16A**. (C) Normalized gray values of disk and gap on the CE as a function of time, Δgray value = normalized gray value of gap – normalized gray value of disk.

Throughout the work, the light intensity (gray value) captured by the camera is systematically normalized with that measured from WO_3 CE at bleaching state. The normalized gray value can be linked to the transmittance of the WO_3 CE only under pre-assumptions that the transmittance of water and the reflectance of WE remain unchanged during the measurement. The former is acceptable when the generation of gas bubbles is insignificant. This is why we did not test higher voltage. However, the latter could be questionable as the optical properties of Au surface were reported to vary under applied potential[272]. **Figure 3.17** shows a control experiment for **Figure 3.13** where the WO_3 CE was replaced by non-electrochromic ITO. It is seen that the current is much lower at the same applied voltage, and the redox peaks disappear (**Figure 3.17A**). This could be explained by the removal of redox reactions of WO_3. The optical images with normalized gray values look very similar for different applied voltages.

Yet, the edges of Au disks could still be distinguished especially when the voltage is high (**Figure 3.17B**), although it has much less contrast to the Au disk and the gap as compared with **Figure 3.13**. One should be very careful in interpreting this edge effect. On one hand, the optical pathway at the junction between Au and ITO is very complex due to their different reflectivity. This might cause some artifacts in imaging. On the other hand, it could also be that the interface junction between Au film and ITO has a high electric intensity. Generally, an interfacial polarization occurs when electrode materials with different charge densities are coupled, resulting in a potential difference, called the Schottky barrier[273]. The potential difference will cause carriers to spontaneously migrate near the interface so the Fermi level will reach an equilibrium. As a result of the interfacial charge redistribution, an electric field would be generated across the interface, which can accelerate electron transfer/ion diffusion. This would result in an improvement in catalyzing water oxidation, and could explain the appearance of normalized gray value change at edges prior to Au disks in **Figure 3.13.**

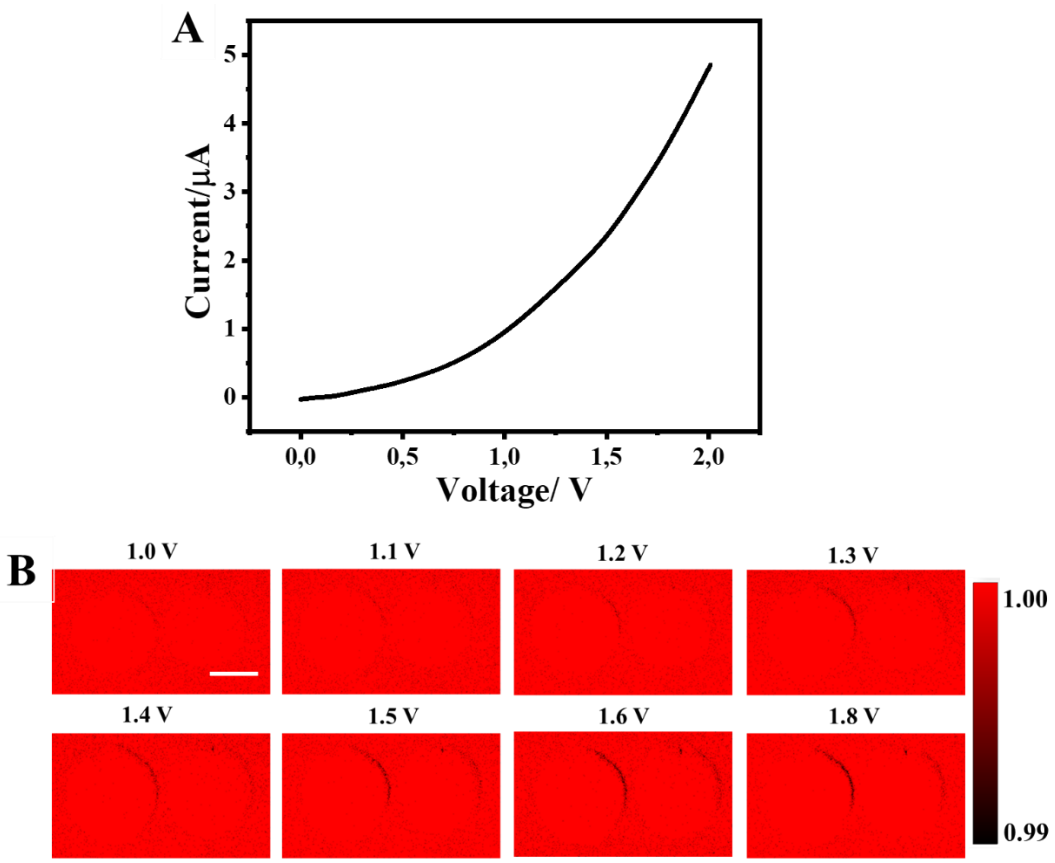

Figure 3.17 The contrast experiment: the optical change of the cell device (bare ITO as CE) with increasing voltage. Scale bar (white): 100 μm.

3.3.4.3 WE: stainless-steel sheet with Au disk and fingerprint

The stainless-steel sheet replaces ITO substrate for sputtering Au disk on its surface as WE. The electrochemical cell reaction conditions (CE, eletrolyte, PTFE thickness) are same with the experiment in **Figure 3.18,** except the WE substrate. **Figure 3.18A** shows the photo of WE made of Au disks sputtered on stainless-steel sheet. By scanning voltage, images are acquired as shown in **Figure 3.18B**. The edges of micro-disks (called micro-rings) are firstly visible on the CE with decreased normalized gray value when the applied voltage is 0.4 V because of Schottky barrier effect, which is consistent with the phenomenon in **Figure 3.13B** (1.1 V to 1.2 V).

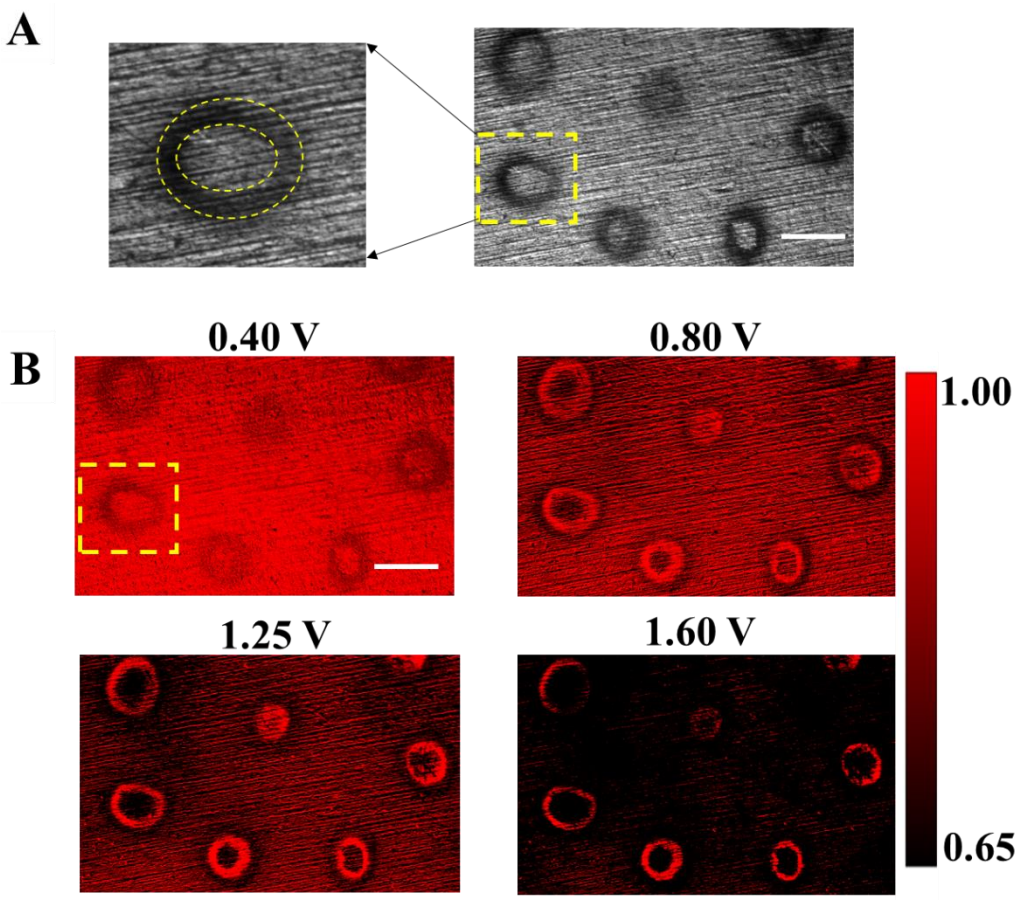

Figure 3.18 (A) Optical micrograph of Au disks sputtered on stainless-steel sheet. Scale bar (white): 200 μm. (B) The optical change of CE with increasing voltage corresponding to the active areas on the WE. Scale bar (white): 200 μm.

The normalized gray values outside and in the middle of the micro-rings also decrease with increasing voltage, but the inside of the micro-rings maintain a higher gray value (bright region). Especially for a higher voltage (1.60 V), the gray value on all the

regions on the CE decrease except that of the inside of the micro-rings. This result is different from the Au/ITO as WE in that the color change from the edges of micro-rings gradually diffuses to the center with increasing the voltage. This reason might be that the Au disks distribution are not uniform on the stainless-steel sheet, as shown in **Figure 3.18**(A) (Enlarged image in yellow dotted line), there is a thicker gold film only at the edges of the gold disk, but it is difficult to see the middle portion.

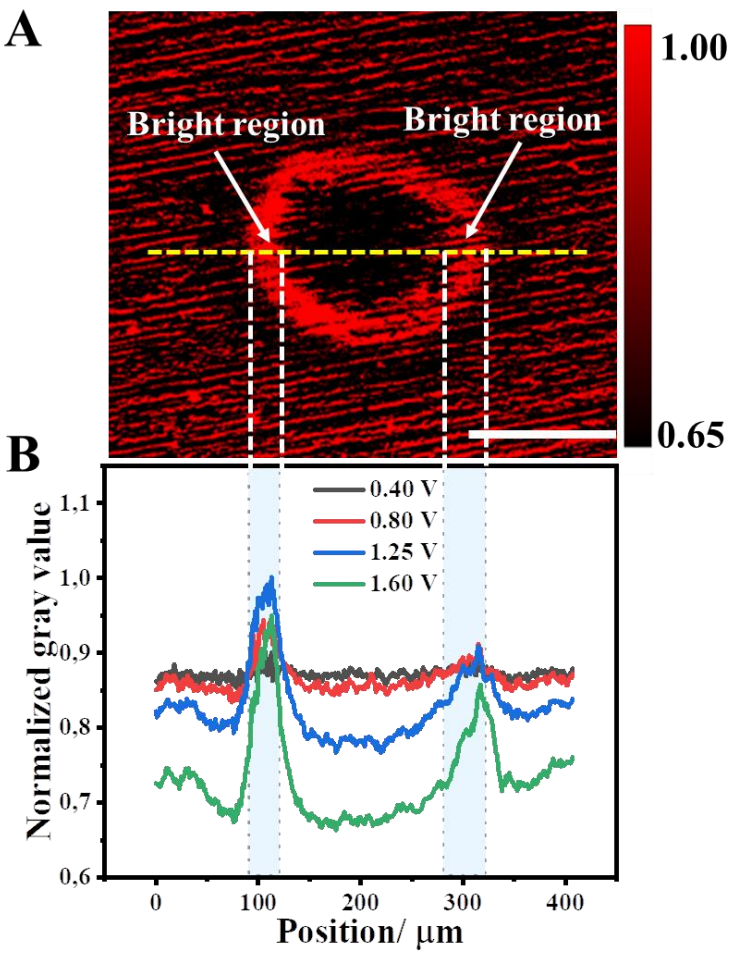

Figure 3.19(A) The micro-disk image in yellow dotted line in **Figure 3.18B**. (B) The variation of normalized gray value of the micro-disks on CE along with the yellow dotted line in **Fig. 3.19A** with increasing the voltage. Scale bar (white): 100 μm.

Since the stainless steel sheet contains some metal elements, such as Ni, Cr, Cu, Co, *etc*. [274], it has high electrocatalytic reactivity for the oxidation of water compared to Au film in this electrochemical cell. Therefore, the current through the stainless steel is

larger than that of the gold film, which causes the color of the corresponding part on the CE to change. **Figure 3.19B** shows the variation of the normalized gray value of a micro-disk (the yellow dotted frame in **Fig. 3.18B**) on CE along with the yellow dotted line in **Figure 3.19A** with increasing the voltage. It can be seen clearly that there are two high gray scale values at positions about 100 μm and 300 μm that do not vary greatly with increasing voltage, corresponding to the bright regions on CE of **Figure 3.19A**. However, the gray value of other regions decreases with the increase of voltage. The bright regions are caused by the negligible color change on the CE, which is a result of the lower electrocatalytic performance of the Au film on stainless steel sheet at this voltage. This result further proves that stainless steel as a substrate has better catalytic activity by local coloration of the CE.

To further verify the extensive application of this analysis method, the local reactivity of stainless-steel sheet covered sebaceous fingerprint is studied. To prepare latent sebaceous fingerprint samples, a volunteer is asked to wash his hands with hand sanitizer, and dry them under a nitrogen stream. And then the volunteer gently rubs his finger over his forehead or nose regions and presses it on stainless steel sheet with a light pressure (**Figure 3.20A**). The stainless-steel sheet covered sebaceous fingerprint as WE, WO_3/ITO as CE, 25 μm PTFE as spacer and pure water as electrolyte are assembled to above-mentioned electrochemical cell. By scanning the voltage from 0 to 1.6 V under optical microscopy, it is seen that several fingerprints gradually appear after 0.45 V (**Figure 3.20C**). The appearance of fingerprints could be explained as follows: when applying the voltage to this electrochemical cell, the regions non-covered with sebaceous on the stainless-steel sheet have high reactivity causing the local coloration on the CE. In contrast, other areas covering the sebaceous behave lower or non-conductivity so that can't result in the local coloration on the CE. Therefore, optical change obviously on the CE corresponding to the active regions on the WE. Moreover, the non-uniform coverage of sebaceous on the stainless-steel sheet led to each fingerprint stripe is not contiguous like the yellow arrow marked in **Figure 3.20B**. This could explain the reason that the optical change of each fingerprint stripe on the CE behave not uniform (yellow arrow marked in **Figure 3.20C**). The above results further indicate this method has meaningful value for reactivity analysis of various WEs.

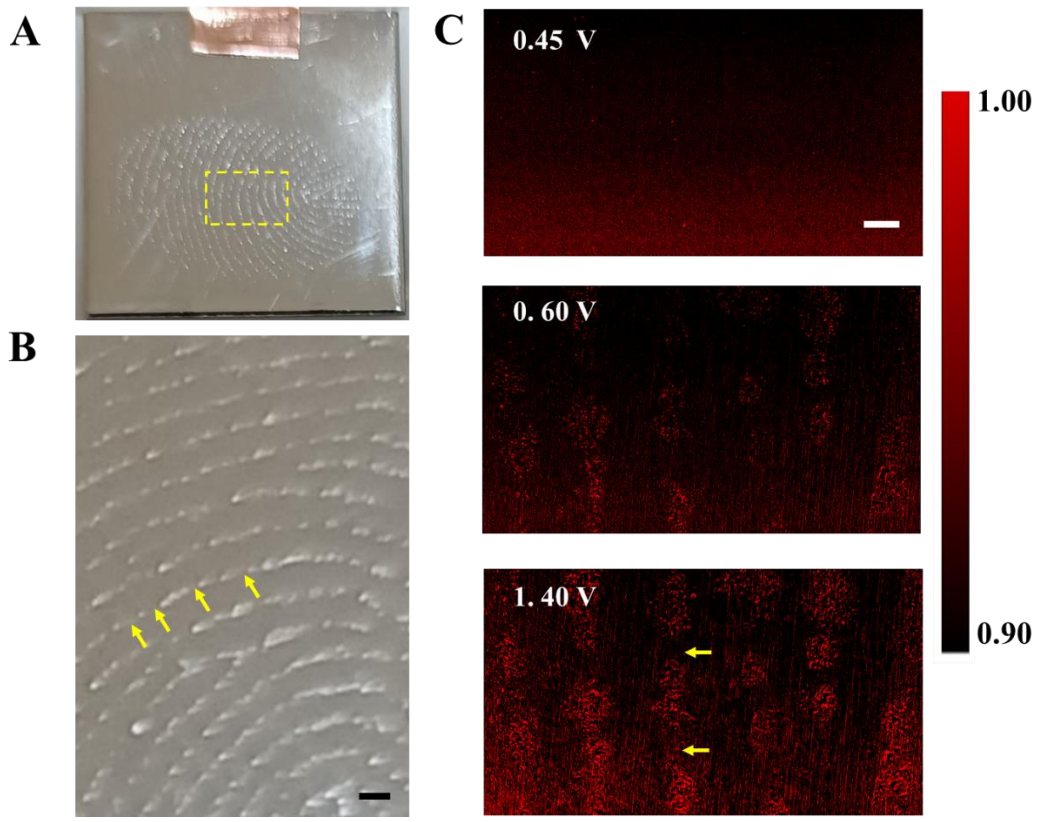

Figure 3.20 (A) Photo of fingerprint on the stainless-steel sheet. (B) The enlarged regions on the yellow dotted frame in (A), scale bar (black): 1000 μm. (C) The images for optical intensity changes on the CE at a voltage of 0.40 V, 0.60 V and 1.40 V, respectively, applied to the WE. Scale bar (white): 300 μm.

3.4 Discussion

The experimental results above clearly demonstrated the link between CE color change and the reactivity of the WE. It arises from the inhomogeneous current distribution in the electrochemical cell. This is counter intuitive to usual principles of electrochemical cell design. First, the electrolyte should have high resistance to inhibit lateral dispersion of current in the solution. This is why we used pure water without adding supporting electrolyte. Second, the CE should be placed as close as possible to WE for "projecting" the pattern. This could avoid homogenizing the current distribution on CE, and could also compensate the absence of supporting electrolyte by reducing resistance of the solution.

The electrochromic reaction of WO_3 CE requires the intercalation of H^+ (**Figure 3.3 A**). A question then arises: Can pure water provide enough H^+ for the color change? With 10^{-7} mol/L concentration in pure water, it is clearly not enough for inducing the clear color change observed in this work. However, one should consider the oxidation of water on WE that generates H^+. The H^+ generated on WE can easily reach CE with mass transport since the two electrodes are positioned close. It is similar as generation-collection mode of SECM[275]. Note that the electrolyte is weakly supported, migration could also play an important role. Considering that H^+ is positively charged, migration facilitates its transfer from WE to CE when applying positive bias on WE. This is beneficial for localizing the current distribution on CE.

The direct projection of WE reactivity to CE color change is only an ideal case. The lateral charge propagation on CE is unavoidable, and even a more general situation. It could occur when applying high voltage (**Figure 3. 5**), or applying voltage for long time (**Figure 3.6**), or having two reactive spots close to each other on WE (**Figure 3.9**). While the former two could still be optimized with experimental conditions, the latter depends on the property of the sample thus may limit the application of the method. A better way is to quantitatively analyze the reactivity of WE from the optical signals on CE by modeling. The model should consider the electrochemical reaction kinetics on both WE and CE, the mass transport of species in the electrolyte including diffusion and migration, and the lateral boundary conditions. Mathematically, two types of lateral boundary conditions are convenient to work with. One is symmetry or no-flux, where the lateral flux of species at boundary is zero. This is applicable for the cell boundary regulated by PTFE spacer, and also for highly symmetrical systems like Au interdigitated electrodes. Another type is semi-infinite diffusion, where the concentration of species always equals to the initial condition (bulk) at the boundary. This is applicable for studying reactive sites that are well apart, with an inert background, such as points 1-6 in **Figure 3.11**. The detail modeling analysis is still ongoing.

From the experimental aspect, several improvements can also be foreseen. The optical signal acquisition could be carried out at multiple wavelengths to improve the sensitivity in capturing the electrochromic change of CE. The electrochromic material for CE could also be optimized for higher color switching speed. This could eliminate the kinetic effect of CE by replacing with Nernst boundary condition, which would greatly ease the analysis of transient behavior of WE.

3.5 Conclusion

The reactivity distribution on WE is successfully projected to the electrochromic CE in the form of local color change, which is then captured by optical imaging. Model systems involving Au interdigitated electrodes, Au microelectrode array, or Au sputtered on ITO as WE, and WO_3 film as CE, are demonstrated. Pure water is used as electrolyte to have high resistance, and the generation of H^+ by oxidation on WE. The latter is essential for driving the coloration of WO_3 CE. The WE is placed in parallel to CE with PTFE spacer controlling the distance. It is seen that the distance needs to be comparable as the size of the target of observation. The effect of voltage and time are studied for inhibiting the lateral color dispersion on CE. This preliminary work opens the door for mapping the reactivity of WE by the optical change of CE. As the signals are captured from the CE, the method does not require specific choice or modification of neither the WE nor the electrolyte. This could be advantageous over optical methods based on direct observation of WE. Possible improvement in both analytical and experimental aspects are discussed.

Chapter IV

Conclusions and Perspectives

In this thesis, we mainly focus on two research aims: one is that using counter electrode (CE) combining with stripping voltammetry to achieve the detection of analytes that cannot usually be detected by this technique (**Chapter II**); another is that mapping local optical change of CE to analyze the reactivity of working electrode (WE) (**Chapter III**).

In first research aim **(Chapter II)**, we have developed a new electroanalytical method based on the CE as signal sensing element. Different from the traditional CE selection criteria, a microelectrode is used as CE (micro-CE). Moreover, the WE and CE are respectively put in two half electrolyte cells (called cell 1a and cell 1b) that are connected by a "bridge". Once the potential is applied to this device, the analytes are oxidized on the WE surface in cell 1a, while Cu^{2+} ions are reduced and deposited as $Cu^{(0)}$ on the CE surface in cell 1b. Therefore, the analytes concentration can be detected by analyzing the $Cu^{(0)}$ stripping signal from CE surface. The major merits of this analysis method include:

1. The stripping electroanalysis method based on micro-CE enables the measurement of analytes that cannot be pre-concentrated on the WE.

2. Separate electrolyte cells effectively prevent mutual interference between WE and CE.

3. The charging current of CE could be negligible due to the usage of microelectrode.

Furthermore, considering that chronoamperometry is applied for the oxidation of analytes in WE surface, it is seen that the charging current on WE can be successfully eliminated by adjusting the oxidized potential of analytes, which avoids the interference of non-faradic current from WE to CE and achieves an accurate detection. when extending $Cu^{(0)}$ deposition time, the better sensitivity and detection of ultra-low concentration can be improved obviously. Moreover, the effect of the concentration and pH value of $CuSO_4$ on the $Cu^{(0)}$ deposit amounts have also been explored. It is illustrated that there is a large $Cu^{(0)}$ deposition efficiency with decreasing concentration

of $CuSO_4$, which is beneficial to the detection of lower analytes concentration. To prove the practical application value of this analysis method, the gentisic acid (an antioxidant molecule used in pharmaceutical industry) has been detected. With and without stirring the analytes solution in cell 1a, the result indicates that the sensitivity of this analysis can be improved by *ca.* 4 times under the condition of stirring. Overall, this new electroanalysis method has the great potential for providing quantitative analysis to analytes that can't be pre-concentrated on the WE.

However, some challenges still exist in this research. First, this analysis method is limited for analytes that just could be oxidized on WE in cell 1a and the concomitant reduction of Cu^{2+} on CE in cell 1b, however other analytes might need to be reduced during detecting in cell 1a that can't be achieved. The CSV might be able to replace the ASV for analysis of pre-concentrated substrate on CE in cell 1b. The conventional CSV technique has been used to determine a variety of inorganic and organic compounds that form an insoluble film on the electrode during the preconcentration step at a positive potential. It means that some non-metal ions like halides (iodide, bromide, chloride) could be used instead of Cu^{2+} to form insoluble film on the electrode surface. The hanging mercury drop electrode (HMDE) is the most commonly used electrode for analyzing metal or non-metal ions. By applying a cathodic potential to the WE to cause the reduction of analytes in cell 1a, at the same time, a sparingly soluble compound would be formed with the mercury electrode (CE) at anodic potential during the preconcentration process (**equation 1.6−1.7**). As a result of the application of the positive potential, metallic mercury is oxidized to mercury(I). Afterward, the deposit is stripped from the electrode by application of a scan toward more negative potentials. Therefore, the analytes concentration could be obtained indirectly from the stripping signal. However, due to the current intensity in CSV depending on the amount of insoluble film formed on the CE area, it is unfavorable for the detection of high concentration analytes which could lead to the surface saturation of CE. Although some solid electrode materials have been reported, for example, silver electrodes have been used for the CSV determination, the drawback of the use of solid electrode materials is the typically poor reproducibility of the analysis and the low sensitivity, as a result of irregularities on the electrode surface and irreversible reduction of hydroxides (in the case of metals).

Second, the coulombic efficiency (the ratio of charge on CE and charge on WE) is not too high (*ca.* 60 %) and decreases with decreasing the concentration of analyte (**Figure 4.1**). This means that only a fraction of the charge on the CE has been used to deposit copper. Other small fraction of the charge might be mainly consumed by hydrogen evolution reaction (HER), the reduction of NO_3^- and dissolved O_2. In addition, the formation of bubbles from HER may block electrode accessibility, thereby changing the area of effective electrodes and reducing copper deposit amount. As increasing the pH value in $CuSO_4$ solution, generation of OH^- caused by water or oxygen reduction will result in a rise in pH, which in turn affects metal speciation or can produce insoluble metal (hydro)oxides (**equation 4.1−4.2**). This also could explain the multiple messy stripping peaks in **Figure 2.21** when the $CuSO_4$ solution with a pH of 4. Therefore, some optimized condition might be taken in cell1b: using Na_2SO_4 electrolyte instead of $NaNO_3$, deoxygenating before Cu^{2+} deposition, assuring the pH is lower than 4.

$$O_2\,(aq) + 2\,H_2O\,(l) + 4e^- \rightarrow 4\,OH^-(aq)\ (alkali) \qquad (4.1)$$

$$Cu^{2+}(aq) + 2\,OH^- \rightarrow Cu(OH)_2(s) \qquad (4.2)$$

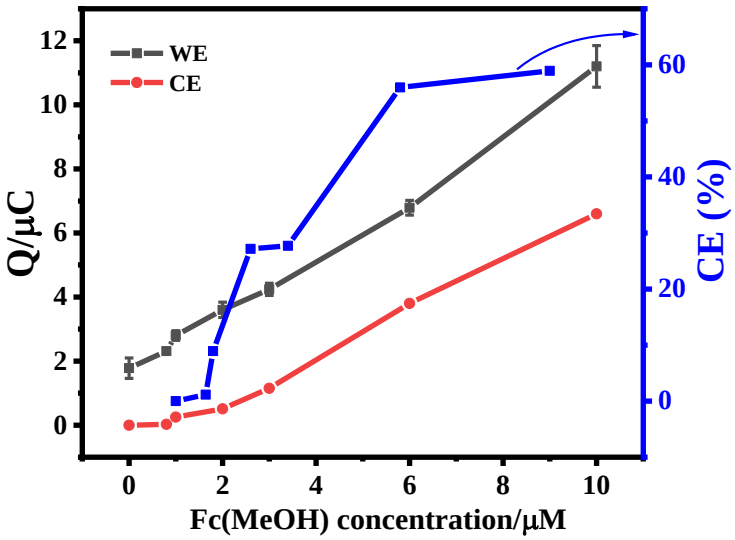

Figure 4.1 Variation of charge (Q, red and black line) and coulomb efficiency (CE, blue line) as a function of $Fc(MeOH)_2$ concentration (by applying +0.3 V to WE1 for 800s

in blank or 0.8,1,2,3, 6 or 10 μM $Fc(MeOH)_2$ solutions in Cell 1a), measured from current integration on WE1 in Cell 1a and Cu stripping from CE1 (=WE2) in Cell 2. Error bars indicate the standard deviation of 5 repetitive measurements.

In second research aim (**Chapter III**), we have developed an optical electrochromic imaging technique based on the CE that can trace the localized electrochemical reactivity on WE surface without extra modification. The substrate containing active regions and WO_3/ITO are used as WE and CE, respectively. WO_3/ITO behaves better electrochromic property with cation ions intercalating inside WO_3 at a negative potential, which can result in the reduction of optical transmittance. To determine the local electrochemical reaction dynamics on WE, we place the WE and CE in parallel and control the distance between them at a micro-meter level so that obtaining local electrochromic on CE. The electrochemical cell is mounted under an optical microscope with optics focused on the WE. The color change of CE can be quantitatively measured with a CMOS camera under an optical microscope. By using this method, we are able to study the local reactivity of diverse WE types (Au interdigital electrode, Au microelectrode array, Au sputtering on ITO) as well as distinguish simultaneous reaction dynamics of multiple active regions on the WE, which provides access to transient behavior of the system. The pure water as electrolyte has resistance high enough to inhibit lateral dispersion of current in the solution. Moreover, due to weakly supported electrolyte, migration could also play an important role. The released H^+ from the oxidation of water catalyzed by the WE at a positive bias could migrate to CE which is beneficial for localizing the current distribution on CE. The effect of time at constant voltage, and voltage on the local optical change of CE are explored. It is found that longer time and higher voltage lead to more uniform color changes on the CE surface due to lateral charge propagation. Moreover, the distance between CE and WE are also investigated by using PTFE spacers with different thicknesses. The results demonstrate that smaller distance is favorable for acquiring non-homogeneous current distribution on the CE. Therefore, the better resolution could be achieved by adjusting the time, voltage and distance between WE and CE. This CE electrochromic technique is expected to find wide applications in electrocatalytic, biosensors, and energy, *etc*., owing to its suitability for CE material and no modification requirements for WE and electrolytes.

For this research, several improvements can also be foreseen:

1. The optical change of CE directly reflects the local reactivity on the WE which is directly related to the local current density distribution. Therefore, the quantitative mathematical derivation of the relationship between the local current density distribution on WE and derivative of the optical intensity change on the CE might be built up according to the **equation** (**4.3−4.4**):

$$\Delta I(X,Y) = \alpha \times \sigma(x,y) = \alpha \int i(x,y,t)_{CE}\, dt \tag{4.3}$$

$$\frac{\partial I(X,Y)}{\partial t} = i(x,y,t)_{CE} = i(x,y,t)_{WE} \tag{4.4}$$

where $\Delta I(X, Y)$, α, $\sigma(x, y)$, $(x, y, t)_{CE}$, and $(x,y,t)_{WE}$ are optical intensity changes in the white circle area in **Figure 4.2(A)**, the constant to translate the charges to the intensity, the total intercalated charge density at local coloration region on CE in **Figure 4.2(B)**, and the local current density on CE is derived from total intercalated charge density, the local current density on WE in **Figure 4.2(B).**

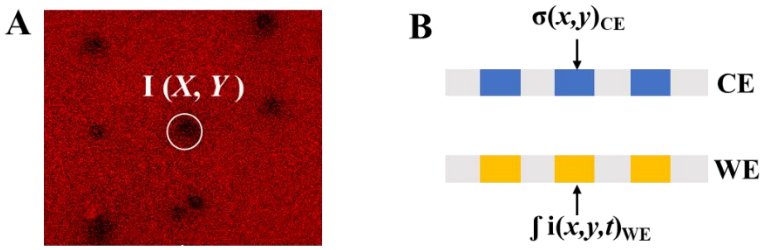

Figure 4.2 (A) The images for optical change on CE. (B) Schematic diagram for two parallel electrodes: local active regions on WE corresponding to local coloration on CE.

In fact, the reaction kinetic of WE and CE, mass transfer (diffusion and migration) should be considered, which lead to the mathematical relationship the optical intensity and local reactivity on WE more complicated. Therefore, that relationship is still being worked on.

2. To understand the factors affecting local reactivity mechanism in this system, we need to build related simulations. To start with, we just consider primary current density distribution, meaning that electrochemical reaction on two electrodes are influenced by the eletrolyte conductivity without concentration gradient on the solution. The model is shown in the **Figure 4.3**.

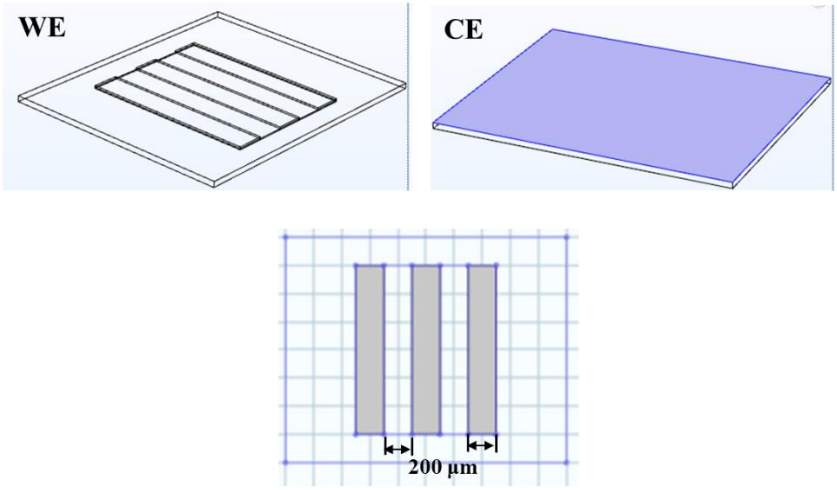

Figure 4.3 The model includes WE and CE, the WE imitates Au interdigital electrode. The width for gap and strip: 200 µm.

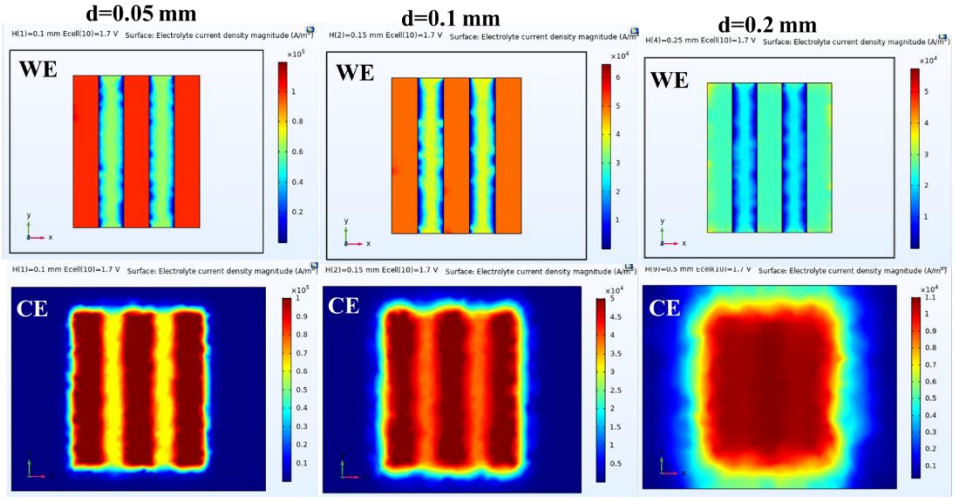

Figure 4.4 The Comsol simulation: current density distribution on WE and CE, repectively. The distance between WE and CE is 0.05 mm, 0.1 mm, and 0.2 mm, respectively.

Here, the effect of the distance between WE and CE on the current density distribution is firstly studied. As shown in **Figure 4.4**, the current density distribution on the WE decreases with increasing the distance, while the current density on the CE also decreases and behaves more homogeneous. This result is similar to the actual experiment (**Figure 3.8**) although this is a asumption condition. However, in practical case, we have to consider the electrode kinetics and mass transfer which might make the current density distribution more homogeneous. In addition, because water as electrolyte has a low conductivity, proton migration also needs to be taken into account, which will make simulation more complicated. At present, migration is also considered,

but convergecnce of simulation can’t be achived. There is no clear explanation for the problem, perhaps it is due to a lack of precision in some parameter settings.

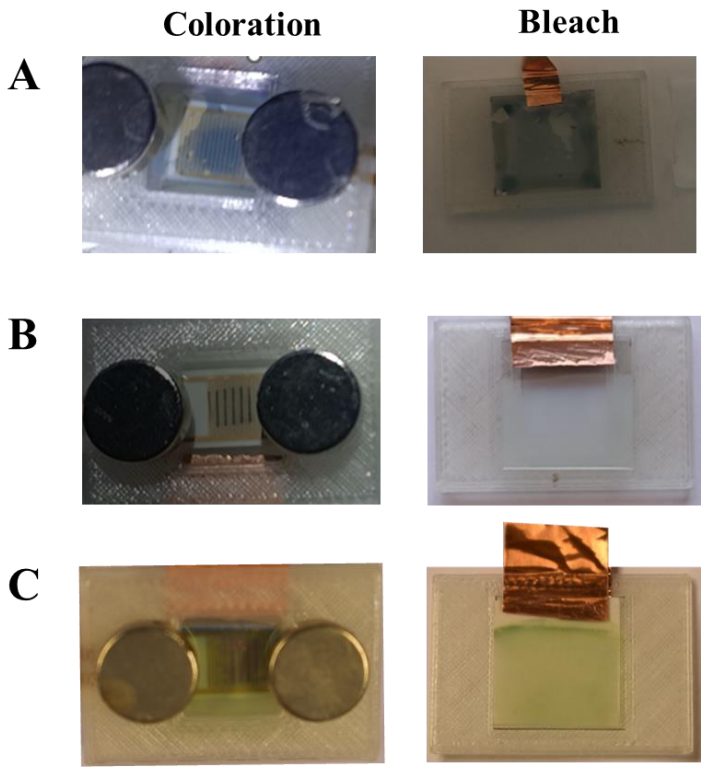

Figure 4.5 The pictures for colaration and bleach of CE at a voltage of 1.8 V, 5s: (A) PEDOT:PSS/ITO, (B) WO_3/ITO, (C)PANI/ITO.

3. The electrochromic material for CE could also be optimized for higher color switching speed. In electrochromic device, the distance between WE and CE is about 25 µm, so even 1 s would be sufficient for the H^+ generated on WE diffusing to the CE. Thus, the enhancement in coloration with time is likely related to the kinetics of WO_3 coloration on CE, which is known to be relatively slow in the order of a few seconds (**Figure 3.6**). To eliminate the kinetic of CE by replacing with Nernst boundary condition, which would greatly simplify the analysis of WE transient behavior, it is possible to use organic materials instead of inorganic ones. The former possess high optical contrast, and exhibit fast response time and high staining efficienc[276]. PEDOT:PSS modified ITO has been attempted as the CE, however, in comparison to the local colaration of WO_3/ITO (**Figure 4.5B**), the coloration effect of PEDOT:PSS/ITO is more homogeneous (**Figure 4.5A**). Moreover, the PEDOT:PSS film is not stable after bleaching. The reason is not yet clear. It might be caused by the

hydrophobic ITO surface leading to poor adhesion. Therefore, This deserves further exploration. When using the Polyaniline (PANI) electrodeposited on the ITO as CE, the four purple stripes are seen clearly under a voltage of 1.8 V, 5 s (**Figure 4.5C**). After bleaching, the PANI film still keeps stable, meaning that it is a better candidate for CE. However, considering that its coloration contrast (from green to deep green or purple) is not very obvious compared to WO_3 (from colorless to blue), we finally chose to use WO_3/ITO as CE.

4**.** To understand whether the thickness of WO_3 film has an effect on coloration contrast and coloration reponse time, the optimal thickness of WO_3 film should be explored. However, the WO_3 electrochromic CE was prepared by electrodeposition on ITO from peroxo-tungstic acid (PTA) solution (Detailed instructions can be found in **section 3.2**). During scanning CV to deposit WO_3 film on ITO, some yellow precipitates will gradually emerge from the PTA solution which means that PTA concentration will change with increasing time. Consequently, the thickness of the WO_3 film cannot be easily controlled, even if it is deposited for the same time and potential. Besides electrodeposition method, a multitude of different techniques have been used for WO_3 film growth on the ITO contaning metal organic chemical vapor deposition, the sol–gel process, pulsed laser deposition or sputter deposition, *etc*. Especially, sputter-deposited coatings exhibit some intrinsic advantages, including high adhesion and homogeneous film thickness, high growth rates, and high reproducibility, which contribute to their dominance in industrial applications. Therefore, to ensure better control over WO_3 film thickness and uniformity, future studies will utilize sputter-deposited coatings methods instead of electrodeposition method.

The future plans: Firstly, we need to solve the above-mentioned problems. After that, we will further explore the factors that affect the resolution. We aim to reach the nanoscale resolution as soon as possible, however, the resolution is currently limited to 25 μm. Therefore, the CE electrochromic material, the cell design containing distance control between two parallel electrode, upgrading optical device will be further optimized.

References

[1] I. Švancara, K. Vytřas, K. Kalcher, A. Walcarius, J. Wang, Carbon paste electrodes in facts, numbers, and notes: A review on the occasion of the 50-years jubilee of carbon paste in electrochemistry and electroanalysis, Electroanalysis. 21 (2009) 7–28. https://doi.org/10.1002/elan.200804340.

[2] C. Batchelor-McAuley, E.J.F. Dickinson, N. V. Rees, K.E. Toghill, R.G. Compton, New electrochemical methods, Anal. Chem. 84 (2012) 669–684. https://doi.org/10.1021/ac2026767.

[3] P. Kissinger, W. Heineman, Laboratory techniques in electroanalytical chemistry, CRC Press, 2018.

[4] F.-R.F. Fan, A.J. Bard, Electrochemical detection of single molecules, Science 267 (1995) 871–874. https://doi.org/10.1126/science.267.5199.871.

[5] W. Dungchai, O. Chailapakul, C.S. Henry, Electrochemical detection for paper-based microfluidics, Anal. Chem. 81 (2009) 5821–5826. https://doi.org/10.1021/ac9007573.

[6] G.A. Crespo, S. Macho, F.X. Rius, Ion-selective electrodes using carbon nanotubes as ion-to-electron transducers, Anal. Chem. 80 (2008) 1316–1322. https://doi.org/10.1021/ac071156l.

[7] R.W. Cattrall, H. Freiser, Coated wire ion selective electrodes, Anal. Chem. 43 (1971) 1905–1906. https://doi.org/10.1021/ac60307a032.

[8] X.A. Perez, A.M. Andrews, Chronoamperometry to determine differential reductions in uptake in brain synaptosomes from serotonin transporter knockout mice, Anal. Chem. 77 (2005) 818–826. https://doi.org/10.1021/ac049103g.

[9] E.J.F. Dickinson, I. Streeter, R.G. Compton, Chronoamperometry and cyclic voltammetry at conical electrodes, microelectrodes, and electrode arrays: theory, J. Phys. Chem. B. 112 (2008) 4059–4066. https://doi.org/10.1021/jp711936y.

[10] M.A. Alpuche-Aviles, D.O. Wipf, Impedance feedback control for scanning electrochemical microscopy, Anal. Chem. 73 (2001) 4873–4881. https://doi.org/10.1021/ac010581q.

[11] F. Xia, T. Mueller, Y. Lin, A. Valdes-Garcia, P. Avouris, Ultrafast graphene photodetector, Nat. Nanotechnol. 4 (2009) 839–843.

https://doi.org/10.1038/nnano.2009.292.

[12] Q. Xie, E. Perez-Cordero, L. Echegoyen, Electrochemical detection of C606- and C706-: Enhanced stability of fullerides in solution, J. Am. Chem. Soc. 114 (1992) 3978–3980. https://doi.org/10.1021/ja00036a056.

[13] D. Ji, L. Liu, S. Li, C. Chen, Y. Lu, J. Wu, Q. Liu, Smartphone-based cyclic voltammetry system with graphene modified screen printed electrodes for glucose detection, Biosens. Bioelectron. 98 (2017) 449–456. https://doi.org/10.1016/j.bios.2017.07.027.

[14] D. Mandler, Fritz Scholz (Ed.): Electroanalytical methods. Guide to experiments and applications, 2nd ed., Anal. Bioanal. Chem. 398 (2010) 2771–2772. https://doi.org/10.1007/s00216-010-4195-5.

[15] K.K. LM Moretto, Environmental analysis by electrochemical sensors and biosensors, Springer New York, 2014.

[16] Q. Liu, C. Ma, X.P. Liu, Y.P. Wei, C.J. Mao, J.J. Zhu, A novel electrochemiluminescence biosensor for the detection of microRNAs based on a DNA functionalized nitrogen doped carbon quantum dots as signal enhancers, Biosens. Bioelectron. 92 (2017) 273–279. https://doi.org/10.1016/j.bios.2017.02.027.

[17] E.E. Ferapontova, E.M. Olsen, K. V. Gothelf, An RNA aptamer-based electrochemical biosensor for detection of theophylline in serum, J. Am. Chem. Soc. 130 (2008) 4256–4258. https://doi.org/10.1021/ja711326b.

[18] J. Wang, Electrochemical glucose biosensors, Chem. Rev. 108 (2008) 814–825. https://doi.org/10.1021/cr068123a.

[19] V.B. Juska, M.E. Pemble, A critical review of electrochemical glucose sensing: evolution of biosensor platforms based on advanced nanosystems, Sensors. 20 (2020) 6013. https://doi.org/10.3390/s20216013.

[20] E.H. Yoo, S.Y. Lee, Glucose biosensors: an overview of use in clinical practice, Sensors. 10 (2010) 4558–4576. https://doi.org/10.3390/s100504558.

[21] R.A. Clark, P.B. Hietpas, A.G. Ewing, Electrochemical analysis in picoliter microvials, Anal. Chem. 69 (1997) 259–263. https://doi.org/10.1021/ac960559a.

[22] K.C. Honeychurch, Printed thick-film biosensors, in: Print. Film., Woodhead Publishing Limited, 2012: pp. 366–409.

[23] S.A. Maier, Plasmonics : Fundamentals and Applications, Springer New York,

NY, 2004.

[24] P. Westbroek, Fundamentals of electrochemistry, in: Anal. Electrochem. Text., 2005: pp. 3–36.

[25] R. Chen, C. Yang, W. Cai, H.-Y. Wang, J. Miao, L. Zhang, S. Chen, B. Liu, Use of platinum as the counter electrode to study the activity of nonprecious metal catalysts for the hydrogen evolution reaction, ACS Energy Lett. 2 (2017) 1070–1075. https://doi.org/10.1021/acsenergylett.7b00219.

[26] J. Lee, J.R. Selman, Electrode corrosion in a compartmented flow cell by diffusion from the counter electrode, J. Electrochem. Soc. 130 (1983) 1237–1242. https://doi.org/10.1149/1.2119932.

[27] J.C. Myland, K.B. Oldham, Uncompensated resistance. 1. The effect of cell geometry, Anal. Chem. 72 (2000) 3972–3980. https://doi.org/10.1021/ac0001535.

[28] Y. Gao, X. Ding, J. Liu, L. Wang, Z. Lu, L. Li, L. Sun, Visible light driven water splitting in a molecular device with unprecedentedly high photocurrent density, J. Am. Chem. Soc. 135 (2013) 4219–4222. https://doi.org/10.1021/ja400402d.

[29] R. Djoumer, A. Anne, A. Chovin, C. Demaille, C. Dejous, H. Hallil, J.L. Lachaud, Converting any faradaic current generated at an electrode under potentiostatic control into a remote fluorescence signal, Anal. Chem. 91 (2019) 6775–6782. https://doi.org/10.1021/acs.analchem.9b00851.

[30] W.W. Liu, W. Jiang, Y.C. Liu, W.J. Niu, M.C. Liu, K. Zhao, L.Y. Zhang, L. Lee, L. Bin Kong, Y.L. Chueh, Platinum-free ternary metallic selenides as nanostructured counter electrode for high-efficiency dye-sensitized solar cell by interface engineering, ACS Appl. Energy Mater. 3 (2020) 3704–3713. https://doi.org/10.1021/acsaem.0c00172.

[31] J. He, L. You, D.T. Tran, J. Mei, Low-temperature thermally annealed niobium oxide thin films as a minimally color changing ion storage layer in solution-processed polymer electrochromic devices, ACS Appl. Mater. Interfaces. 11 (2019) 4169–4177. https://doi.org/10.1021/acsami.8b16154.

[32] R. Engels, C.J. Smit, W.J.M. van Tilborg, Reactions at the counter electrode in electroreductions under aprotic conditions in one-compartment cells, Angew. Chemie Int. Ed. English. 22 (1983) 691–702. https://doi.org/10.1002/anie.198306910.

[33] L. Ji, J. Wang, S. Zuo, Z. Chen, In situ preparation of pt nanoparticles supported on N-Doped carbon as highly efficient electrocatalysts for hydrogen production, J. Phys. Chem. C. 121 (2017) 8923–8930. https://doi.org/10.1021/acs.jpcc.7b01447.

[34] O. Yassine, O. Shekhah, A.H. Assen, Y. Belmabkhout, K.N. Salama, M. Eddaoudi, H 2 S sensors: fumarate-based fcu-MOF thin film grown on a capacitive interdigitated electrode, Angew. Chemie. 128 (2016) 16111–16115. https://doi.org/10.1002/ange.201608780.

[35] R.R. Kamath, M.J. Madou, Three-dimensional carbon interdigitated electrode arrays for redox-amplification, Anal. Chem. 86 (2014) 2963–2971. https://doi.org/10.1021/ac4033356.

[36] Y. Okumura, S. Oana, Effect of counter electrode in electroformation of giant vesicles, Membranes (Basel). 1 (2011) 345–353. https://doi.org/10.3390/membranes1040345.

[37] M.A. Pech-Canul, A.A. Sagüés, P. Castro, Influence of counter electrode positioning on solution resistance in impedance measurements of reinforced concrete, Corrosion. 54 (1998) 663–667. https://doi.org/10.5006/1.3287646.

[38] Y. Wuu, F.F. Fan, A.J. Bard, High resolution deposition of polyaniline on Pt with the scanning electrochemical microscope, J. Electrochem. Soc. 136 (1989) 885–886. https://doi.org/10.1149/1.2096765.

[39] T. Danieli, D. Mandler, Local surface patterning by chitosan-stabilized gold nanoparticles using the direct mode of scanning electrochemical microscopy (SECM), J. Solid State Electrochem. 17 (2013) 2989–2997. https://doi.org/10.1007/s10008-013-2194-0.

[40] F. Grisotto, A. Ghorbal, C. Goyer, J. Charlier, S. Palacin, Direct SECM localized electrografting of vinylic monomers on a conducting substrate, Chem. Mater. 23 (2011) 1396–1405. https://doi.org/10.1021/cm101563n.

[41] K.M. Brace, B.E. Hayden, A.E. Russell, J.R. Owen, A parallel optical screen for the rapid combinatorial electrochromic analysis of electrochemical materials, Adv. Mater. 18 (2006) 3253–3257. https://doi.org/10.1002/adma.200600786.

[42] T.A. O'Shea, K.H. Mancy, Characterization of trace metal-organic interactions by anodic stripping voltammetry, Anal. Chem. 48 (1976) 1603–1607. https://doi.org/10.1021/ac50005a047.

[43] S.B. Adeloju, A.M. Bond, M.H. Briggs, Critical evaluation of some wet digestion methods for the stripping voltammetric determination of selenium in biological materials, Anal. Chem. 56 (1984) 2397–2401. https://doi.org/10.1021/ac00277a031.

[44] W. Holak, Determination of arsenic by cathodic stripping voltammetry with a hanging mercury drop electrode, Anal. Chem. 52 (1980) 2189–2192. https://doi.org/10.1021/ac50063a044.

[45] K.K. Jinadasa, E. Peña-Vázquez, P. Bermejo-Barrera, A. Moreda-Piñeiro, Smart materials for mercury and arsenic determination in food and beverages, Microchem. J. 179 (2022) 107472. https://doi.org/10.1016/j.microc.2022.107472.

[46] Z. Zhang, O. Niwa, S. Shiba, S. Tokito, K. Nagamine, S. Ishikawa, M. Sugimoto, Electrochemical enzyme biosensor for carnitine detection based on cathodic stripping voltammetry, Sensors Actuators B Chem. 321 (2020) 128473. https://doi.org/10.1016/J.SNB.2020.128473.

[47] C.C.G. Silva, L.M. Silva, B.C. e Silva, S.S. Garrido, M.V. Boldrin, D. De Souza, Cathodic stripping voltammetric determination of β-cyfluthrin, a pyrethroid insecticide, using polished silver solid amalgam electrode, J. Solid State Electrochem. 24 (2020) 1819–1826. https://doi.org/10.1007/s10008-020-04538-w.

[48] C.F.P. Paul Worsfold, Alan Townshend, Encyclopedia of analytical sciences, Elsevier Academic Press, 2005.

[49] S.B. Adeloju, Electrochemical stripping analysis of trace and ultra-trace concentrations of toxic metals and metalloids in foods and beverages, in: Food Toxicants Anal., Elsevier, 2007: pp. 667–696.

[50] H. Obata, C.M.G. van den Berg, Determination of picomolar levels of iron in seawater using catalytic cathodic stripping voltammetry, Anal. Chem. 73 (2001) 2522–2528. https://doi.org/10.1021/ac001495d.

[51] R. Kalvoda, M. Kopanica, Adsorptive stripping voltammetry in trace analysis, Pure Appl. Chem. 61 (1989) 97–112. https://doi.org/10.1351/pac198961010097.

[52] J. Schiewe, K.B. Oldham, J.C. Myland, A.M. Bond, V.A. Vicente-Beckett, S. Fletcher, Linear-scan anodic stripping voltammetry with thin-film electrodes: Theory of the stripping stage and experimental tests, Anal. Chem. 69 (1997)

2673–2681. https://doi.org/10.1021/ac961255r.

[53] D.K.Y. Wong, A.G. Ewing, Anodic stripping voltammetry at mercury films deposited on ultrasmall carbon-ring electrodes, Anal. Chem. 62 (1990) 2697–2702. https://doi.org/10.1021/ac00223a010.

[54] C. Agra-Gutiérrez, J.L. Hardcastle, J.C. Ball, R.G. Compton, Anodic stripping voltammetry of copper at insonated glassy carbon-based electrodes: application to the determination of copper in beer, Analyst. 124 (1999) 1053–1057. https://doi.org/10.1039/a902974e.

[55] R. Inam, G. Somer, Determination of selenium in garlic by cathodic stripping voltammetry, Food Chem. 66 (1999) 381–385. https://doi.org/10.1016/S0308-8146(99)00087-4.

[56] G. Colovos, G.S. Wilson, J.L. Moyers, Simultaneous determination of bromide and chloride by cathodic stripping voltammetry, Anal. Chem. 46 (1974) 1051–1054. https://doi.org/10.1021/ac60344a027.

[57] I. Shain, S.P. Perone, Application of stripping analysis to the determination of iodide with silver microelectrodes, Anal. Chem. 33 (1961) 325–329. https://doi.org/10.1021/ac60171a004.

[58] K. Shimizu, R.A. Osteryoung, Determination of sulfide by cathodic stripping voltammetry of silver sulfide films at a rotating silver disk electrode, Anal. Chem. 53 (1981) 584–588. https://doi.org/10.1021/ac00227a006.

[59] T.M. Florence, Cathodic stripping voltammetry. Part I. Determination of organic sulfur compounds, flavins and porphyrins at the sub-micromolar level, J. Electroanal. Chem. 97 (1979) 219–236. https://doi.org/10.1016/S0022-0728(79)80064-9.

[60] B.L. Dennis, J.L. Moyers, G.S. Wilson, Determination of selenium as selenide by differential pulse cathodic stripping voltammetry, Anal. Chem. 48 (1976) 1611–1616. https://doi.org/10.1021/ac50005a049.

[61] O. Abollino, A. Giacomino, M. Malandrino, Stripping Voltammetry, in: Ref. Modul. Chem. Mol. Sci. Chem. Eng., Elsevier, 2018: pp. 238–257.

[62] J. Wang, J.M. Zadeii, Determination of traces of gallium based on stripping voltammetry with adsorptive accumulation, Anal. Chim. Acta. 185 (1986) 229–238. https://doi.org/10.1016/0003-2670(86)80050-2.

[63] S. Legeai, S. Bois, O. Vittori, A copper bismuth film electrode for adsorptive cathodic stripping analysis of trace nickel using square wave voltammetry, J.

Electroanal. Chem. 591 (2006) 93–98. https://doi.org/10.1016/j.jelechem.2006.03.054.

[64] A. Safavi, Highly sensitive and selective measurements of cobalt by catalytic adsorptive cathodic stripping voltammetry, Talanta. 51 (2000) 1117–1123. https://doi.org/10.1016/S0039-9140(00)00278-2.

[65] M. Vega, C.M. van den Berg, Determination of vanadium in sea water by catalytic adsorptive cathodic stripping voltammetry, Anal. Chim. Acta. 293 (1994) 19–28.

[66] A.A. Ensafi, R. Hajian, Determination of tryptophan and histidine by adsorptive cathodic stripping voltammetry using H-point standard addition method, Anal. Chim. Acta. 580 (2006) 236–243. https://doi.org/10.1016/j.aca.2006.07.076.

[67] C.M.G. Den Van Berg, M. Nimmo, O. Abollino, E. Mentasti, The determination of trace levels of iron in seawater, using adsorptive cathodic stripping voltammetry, Electroanalysis. 3 (1991) 477–484. https://doi.org/10.1002/elan.1140030606.

[68] M. Morfobos, A. Economou, A. Voulgaropoulos, Simultaneous determination of nickel(II) and cobalt(II) by square wave adsorptive stripping voltammetry on a rotating-disc bismuth-film electrode, Anal. Chim. Acta. 519 (2004) 57–64. https://doi.org/10.1016/j.aca.2004.05.022.

[69] K.C. Honeychurch, J.P. Hart, D.C. Cowell, Voltammetric behavior and trace determination of lead at a mercury-free screen-printed carbon electrode, Electroanalysis. 12 (2000) 171–177. https://doi.org/10.1002/(SICI)1521-4109(200002)12:3<171::AID-ELAN171>3.0.CO;2-Q.

[70] J. Wang, B. Tian, Mercury-free disposable lead sensors based on potentiometric stripping analysis of gold-coated screen-printed electrodes, Anal. Chem. 65 (1993) 1529–1532. https://doi.org/10.1021/ac00059a008.

[71] G.K. Ziyatdinova, G.K. Budnikov, V.I. Pogorel'tsev, Determination of captopril in pharmaceutical forms by stripping voltammetry, J. Anal. Chem. 61 (2006) 798–800. https://doi.org/10.1134/S1061934806080144.

[72] Y. Bonfil, E. Kirowa-Eisner, Determination of nanomolar concentrations of lead and cadmium by anodic-stripping voltammetry at the silver electrode, Anal. Chim. Acta. 457 (2002) 285–296. https://doi.org/10.1016/S0003-2670(02)00016-8.

[73] R. Feeney, J. Herdan, M.A. Nolan, S.H. Tan, V. V. Tarasov, S.P. Kounaves, Analytical characterization of microlithographically fabricated iridium-based ultramicroelectrode arrays, Electroanalysis. 10 (1998) 89–93. https://doi.org/10.1002/(SICI)1521-4109(199802)10:2<89::AID-ELAN89>3.0.CO;2-J.

[74] J. Wang, J. Lu, S.B. Hocevar, P.A.M. Farias, B. Ogorevc, Bismuth-coated carbon electrodes for anodic stripping voltammetry, Anal. Chem. 72 (2000) 3218–3222. https://doi.org/10.1021/ac000108x.

[75] A. KrÃ^{3}licka, Bismuth-film-plated carbon paste electrodes, Electrochem. Commun. 4 (2002) 193–196. https://doi.org/10.1016/S1388-2481(01)00301-0.

[76] G. Kefala, A study of bismuth-film electrodes for the detection of trace metals by anodic stripping voltammetry and their application to the determination of Pb and Zn in tapwater and human hair, Talanta. 61 (2003) 603–610. https://doi.org/10.1016/S0039-9140(03)00350-3.

[77] G. Kefala, A. Economou, A. Voulgaropoulos, A study of Nafion-coated bismuth-film electrodes for the determination of trace metals by anodic stripping voltammetry, (n.d.). https://doi.org/10.1039/b404978k.

[78] C. Gouveia-Caridade, R. Pauliukaite, C.M.A. Brett, Influence of Nafion Coatings and Surfactant on the Stripping Voltammetry of Heavy Metals at Bismuth-Film Modified Carbon Film Electrodes, Electroanalysis. 18 (2006) 854–861. https://doi.org/10.1002/elan.200603482.

[79] J. Jia, L. Cao, Z. Wang, Nafion/Poly(sodium 4-styrenesulfonate) Mixed Coating Modified Bismuth Film Electrode for the Determination of Trace Metals by Anodic Stripping Voltammetry, Electroanalysis. 19 (2007) 1845–1849. https://doi.org/10.1002/elan.200703923.

[80] R.A. Durst, Chemically modified electrodes: Recommended terminology and definitions (IUPAC Recommendations 1997), Pure Appl. Chem. 69 (1997) 1317–1324. https://doi.org/10.1351/pac199769061317.

[81] W. Kutner, J. Wang, M. L'her, R.P. Buck, Analytical aspects of chemically modified electrodes: Classification, critical evaluation and recommendations (IUPAC Recommendations 1998), Pure Appl. Chem. 70 (1998) 1301–1318. https://doi.org/10.1351/pac199870061301.

[82] V.D. Vaze, A.K. Srivastava, Electrochemical behavior of folic acid at calixarene based chemically modified electrodes and its determination by

adsorptive stripping voltammetry, Electrochim. Acta. 53 (2007) 1713–1721. https://doi.org/10.1016/j.electacta.2007.08.017.

[83] H. Dong, L. Lin, H. Zheng, G. Zhao, B. Ye, Electrode modified with Langmuir–Blodgett (LB) film of calixarenes for preconcentration and stripping analysis of Hg(II), Electroanalysis. 18 (2006) 1202–1207. https://doi.org/10.1002/elan.200603520.

[84] S. Berchmans, S. Arivukkodi, V. Yegnaraman, Self-assembled monolayers of 2-mercaptobenzimidazole on gold: stripping voltammetric determination of Hg(II), Electrochem. Commun. 2 (2000) 226–229. https://doi.org/10.1016/S1388-2481(00)00002-3.

[85] N.Y. Stozhko, N.A. Malakhova, M. V. Fyodorov, K.Z. Brainina, Modified carbon-containing electrodes in stripping voltammetry of metals, J. Solid State Electrochem. 12 (2008) 1185–1204. https://doi.org/10.1007/s10008-007-0472-4.

[86] I.K. Tonle, E. Ngameni, A. Walcarius, Preconcentration and voltammetric analysis of mercury(II) at a carbon paste electrode modified with natural smectite-type clays grafted with organic chelating groups, Sensors Actuators B Chem. 110 (2005) 195–203. https://doi.org/10.1016/j.snb.2005.01.027.

[87] N.A. Carrington, L. Yong, Z.-L. Xue, Electrochemical deposition of sol–gel films for enhanced chromium(VI) determination in aqueous solutions, Anal. Chim. Acta. 572 (2006) 17–24. https://doi.org/10.1016/j.aca.2006.05.020.

[88] B. Hoyer, T.M. Florence, G.E. Batley, Application of polymer-coated glassy carbon electrodes in anodic stripping voltammetry, Anal. Chem. 59 (1987) 1608–1614. https://doi.org/10.1021/ac00140a007.

[89] S.J. Liu, H.G. Nie, J.H. Jiang, G.L. Shen, R.Q. Yu, Electrochemical sensor for mercury(II) based on conformational switch mediated by interstrand cooperative coordination, Anal. Chem. 81 (2009) 5724–5730. https://doi.org/10.1021/ac900527f.

[90] M. Dali, K. Zinoubi, A. Chrouda, S. Abderrahmane, S. Cherrad, N. Jaffrezic-Renault, A biosensor based on fungal soil biomass for electrochemical detection of lead (II) and cadmium (II) by differential pulse anodic stripping voltammetry, J. Electroanal. Chem. 813 (2018) 9–19. https://doi.org/10.1016/j.jelechem.2018.02.009.

[91] C. Li, J. Hu, M. Lu, C. Zhang, Quantum dot-based electrochemical biosensor

for stripping voltammetric detection of telomerase at the single-cell level, Biosens. Bioelectron. 122 (2018) 51–57. https://doi.org/10.1016/j.bios.2018.09.049.

[92] A. Ono, H. Togashi, Highly selective oligonucleotide-based sensor for mercury(II) in aqueous solutions, Angew. Chemie. 116 (2004) 4400–4402. https://doi.org/10.1002/ange.200454172.

[93] N.S. Choi, Z. Chen, S.A. Freunberger, X. Ji, Y.K. Sun, K. Amine, G. Yushin, L.F. Nazar, J. Cho, P.G. Bruce, Challenges facing lithium batteries and electrical double-layer capacitors, Angew. Chemie - Int. Ed. 51 (2012) 9994–10024. https://doi.org/10.1002/ANIE.201201429.

[94] G. Salinas, B.A. Frontana-Uribe, S. Reculusa, P. Garrigue, A. Kuhn, Highly ordered macroporous poly-3,4- ortho -xylendioxythiophene electrodes as a sensitive analytical tool for heavy metal quantification, Anal. Chem. 90 (2018) 11770–11774. https://doi.org/10.1021/acs.analchem.8b03779.

[95] Z. Guo, S. Li, X. meng Liu, Y.P. Gao, W.W. Zhang, X.P. Ding, Mesoporous carbon-polyaniline electrode: Characterization and application to determination of copper and lead by anodic stripping voltammetry, Mater. Chem. Phys. 128 (2011) 238–242. https://doi.org/10.1016/j.matchemphys.2011.03.001.

[96] A.R. Zanganeh, M.K. Amini, Polypyrrole-modified electrodes with induced recognition sites for potentiometric and voltammetric detection of copper(II) ion, Sensors Actuators B Chem. 135 (2008) 358–365. https://doi.org/10.1016/j.snb.2008.09.005.

[97] F.Y. Song, K.K. Shiu, Preconcentration and electroanalysis of silver species at polypyrrole film modified glassy carbon electrodes, J. Electroanal. Chem. 498 (2001) 161–170. https://doi.org/10.1016/S0022-0728(00)00360-0.

[98] N.L. Pickup, J.S. Shapiro, D.K.. Wong, Extraction of silver by polypyrrole films upon a base–acid treatment, Anal. Chim. Acta. 364 (1998) 41–51. https://doi.org/10.1016/S0003-2670(98)00144-5.

[99] Z. Mousavi, J. Bobacka, A. Ivaska, Potentiometric Ag^+ sensors based on conducting polymers: A comparison between poly(3,4-ethylenedioxythiophene) and polypyrrole doped with sulfonated calixarenes, Electroanalysis. 17 (2005) 1609–1615. https://doi.org/10.1002/elan.200503269.

[100] M.A. Rahman, M.S. Won, Y.B. Shim, Characterization of an EDTA bonded conducting polymer modified electrode: Its application for the simultaneous

determination of heavy metal ions, Anal. Chem. 75 (2003) 1123–1129. https://doi.org/10.1021/ac0262917.

[101] M. Lin, M. Cho, W.S. Choe, Y. Son, Y. Lee, Electrochemical detection of copper ion using a modified copolythiophene electrode, Electrochim. Acta. 54 (2009) 7012–7017. https://doi.org/10.1016/j.electacta.2009.07.025.

[102] X. Xie, D. Stueben, Z. Berner, The application of microelectrodes for the measurements of trace metals in water, Anal. Lett. 38 (2005) 2281–2300. https://doi.org/10.1080/00032710500316050.

[103] A.J. Bard, L.R. Faulkner, Electrochemical methods: fundamentals and applications, John Wiley and Sons, 2000.

[104] N. Spano, A. Panzanelli, P.C. Piu, M.I. Pilo, G. Sanna, R. Seeber, A. Tapparo, Anodic stripping voltammetric determination of traces and ultratraces of thallium at a graphite microelectrode, Anal. Chim. Acta. 553 (2005) 201–207. https://doi.org/10.1016/j.aca.2005.08.003.

[105] N.Y. Stozhko, N.A. Malakhova, M. V Fyodorov, K.Z. Brainina, N.Y. Stozhko, N.A. Malakhova, M. V Fyodorov, K.Z. Brainina, Modified carbon-containing electrodes in stripping voltammetry of metals. Part II. Composite and microelectrodes, J Solid State Electrochem. 12 (2008) 1219–1230. https://doi.org/10.1007/s10008-007-0474-2.

[106] G. Sanna, M.I. Pilo, P.C. Piu, A. Tapparo, R. Seeber, Determination of heavy metals in honey by anodic stripping voltammetry at microelectrodes, Anal. Chim. Acta. 415 (2000) 165–173.

[107] R.M. Takeuchi, A.L. Santos, M.J. Medeiros, N.R. Stradiotto, Copper determination in ethanol fuel samples by anodic stripping voltammetry at a gold microelectrode, Microchim. Acta. 164 (2009) 101–106. https://doi.org/10.1007/s00604-008-0039-9.

[108] M. González de la Huebra, Determination of linuron in soil by stripping voltammetry with a carbon fiber microelectrode, Talanta. 54 (2001) 1077–1085. https://doi.org/10.1016/S0039-9140(01)00372-1.

[109] M.A. Baldo, S. Daniele, Anodic stripping voltammetry at bismuth-coated and uncoated carbon microdisk electrodes: Application to trace metals analysis in food samples, Anal. Lett. 37 (2004) 995–1011. https://doi.org/10.1081/AL-120030293.

[110] A. Berduque, Y.H. Lanyon, V. Beni, G. Herzog, Y.E. Watson, K. Rodgers, F.

Stam, J. Alderman, D.W.M. Arrigan, Voltammetric characterisation of silicon-based microelectrode arrays and their application to mercury-free stripping voltammetry of copper ions, Talanta. 71 (2007) 1022–1030. https://doi.org/10.1016/j.talanta.2006.05.090.

[111] C. Kokkinos, A. Economou, Microfabricated chip integrating a bismuth microelectrode array for the determination of trace cobalt(II) by adsorptive cathodic stripping voltammetry, Sensors Actuators B Chem. 229 (2016) 362–369. https://doi.org/10.1016/j.snb.2016.01.148.

[112] P.R.. Silva, M.. El Khakani, B. Le Drogoff, M. Chaker, A.. Vijh, Mercury-electroplated-iridium microelectrode array based sensors for the detection of heavy metal ultratraces: optimization of the mercury charge, Sensors Actuators B Chem. 60 (1999) 161–167. https://doi.org/10.1016/S0925-4005(99)00252-X.

[113] A. Berduque, Y.H. Lanyon, V. Beni, G. Herzog, Y.E. Watson, K. Rodgers, F. Stam, J. Alderman, D.W.M. Arrigan, Voltammetric characterisation of silicon-based microelectrode arrays and their application to mercury-free stripping voltammetry of copper ions, Talanta. 71 (2007) 1022–1030. https://doi.org/10.1016/j.talanta.2006.05.090.

[114] D. Dragoe, N. Spătaru, R. Kawasaki, A. Manivannan, T. Spătaru, D.A. Tryk, A. Fujishima, Detection of trace levels of Pb2+ in tap water at boron-doped diamond electrodes with anodic stripping voltammetry, Electrochim. Acta. 51 (2006) 2437–2441. https://doi.org/10.1016/j.electacta.2005.07.022.

[115] Y. Zhang, D. Li, R.G. Compton, Arsenic (III) detection with underpotential deposition and anodic stripping voltammetry, ChemElectroChem. 8 (2021) 3707–3715. https://doi.org/10.1002/celc.202101022.

[116] P. Ostapczuk, P. Valenta, H. Rützel, H.W. Nürnberg, Application of differential pulse anodic stripping voltammetry to the determination of heavy metals in environmental samples, Sci. Total Environ. 60 (1987) 1–16. https://doi.org/10.1016/0048-9697(87)90403-7.

[117] S.B. Adeloju, A.M. Bond, M.H. Briggs, Multielement determination in biological materials by differential pulse voltammetry, Anal. Chem. 57 (1985) 1386–1390. https://doi.org/10.1021/ac00284a046.

[118] I. Baranowska, P. Markowski, A. Gerle, J. Baranowski, Determination of selected drugs in human urine by differential pulse voltammetry technique, Bioelectrochemistry. 73 (2008) 5–10.

https://doi.org/10.1016/j.bioelechem.2008.04.022.

[119] M. Šeruga, I. Novak, L. Jakobek, Determination of polyphenols content and antioxidant activity of some red wines by differential pulse voltammetry, HPLC and spectrophotometric methods, Food Chem. 124 (2011) 1208–1216. https://doi.org/10.1016/j.foodchem.2010.07.047.

[120] J. Gardiner, M.J. Stiff, The determination of cadmium. lead, copper and zinc in ground water, estuarine water, sewage and sewage effluent by anodic stripping voltammetry, Water Res. 9 (1975) 517–523. https://doi.org/10.1016/0043-1354(75)90077-9.

[121] T.R. Copeland, R.A. Osteryoung, R.K. Skogerboe, Elimination of copper-zinc intermetallic interferences in anodic stripping voltammetry, Anal. Chem. 46 (1974) 2093–2097. https://doi.org/10.1021/ac60350a036.

[122] E.Y. Neiman, L.G. Petrova, V.I. Ignatov, G.M. Dolgopolova, The third element effect in anodic stripping voltammetry, Anal. Chim. Acta. 113 (1980) 277–285. https://doi.org/10.1016/S0003-2670(01)93741-9.

[123] P. Ostapczuk, Z. Kublik, Voltammetric and potentiometric comparison of tendencies of cadmium and zinc to intermetallic compound formation with silver, copper and gold in mercury, J. Electroanal. Chem. Interfacial Electrochem. 83 (1977) 1–17. https://doi.org/10.1016/S0022-0728(77)80497-X.

[124] J.A. Wise, D.A. Roston, W.R. Heineman, The effects of Copper-Zinc and Copper-Cadmium intermetallic compounds in different systems used for anodic stripping voltammetry, Anal. Chim. Acta. 154 (1983) 95–104. https://doi.org/10.1016/0003-2670(83)80010-5.

[125] S. Beng Khoo, J. Zhu, Poly(pyrogallol) film on glassy carbon electrode for selective preconcentration and stripping voltammetric determination of Sb(III), Anal. Chim. Acta. 373 (1998) 15–27. https://doi.org/10.1016/S0003-2670(98)00386-9.

[126] M. Naushad, Z.A. ALOthman, Separation of toxic Pb^{2+} metal from aqueous solution using strongly acidic cation-exchange resin: analytical applications for the removal of metal ions from pharmaceutical formulation, Desalin. Water Treat. 53 (2015) 2158–2166. https://doi.org/10.1080/19443994.2013.862744.

[127] G. Zhao, G. Liu, A portable electrochemical system for the on-site detection of heavy metals in farmland soil based on electrochemical sensors, IEEE Sens. J.

18 (2018) 5645–5655. https://doi.org/10.1109/JSEN.2018.2845306.

[128] X. Dai, R.G. Compton, Gold nanoparticle modified electrodes show a reduced interference by Cu(II) in the detection of As(III) using anodic stripping voltammetry, Electroanalysis. 17 (2005) 1325–1330. https://doi.org/10.1002/elan.200403246.

[129] D.W.M. Arrigan, Tutorial review. Voltammetric determination of trace metals and organics after accumulation at modified electrodes, Analyst. 119 (1994) 1953. https://doi.org/10.1039/an9941901953.

[130] A. Safavi, N. Maleki, E. Shams, H.R. Shahbaazi, Determination of copper by adsorptive stripping voltammetry of its complex with adenine, Electroanalysis. 14 (2002) 929. https://doi.org/10.1002/1521-4109(200207)14:13<929::AID-ELAN929>3.0.CO;2-W.

[131] B.J. Feldman, J.D. Osterloh, B.H. Hata, A. D'Alessandro, Determination of lead in blood by square wave anodic stripping voltammetry at a carbon disk ultramicroelectrode, Anal. Chem. 66 (1994) 1983–1987. https://doi.org/10.1021/ac00085a010.

[132] A.M. Harbin, C.M.G. van den Berg, Determination of ammonia in seawater using catalytic cathodic stripping voltammetry, Anal. Chem. 65 (1993) 3411–3416. https://doi.org/10.1021/ac00071a013.

[133] C.M.G. van den Berg, S.H. Khan, J.P. Riley, Determination of tin in sea water by adsorptive cathodic stripping voltammetry, Anal. Chim. Acta. 222 (1989) 43–54. https://doi.org/10.1016/S0003-2670(00)81878-4.

[134] A. Safavi, N. Maleki, H.R. Shahbaazi, Indirect determination of cyanide ion and hydrogen cyanide by adsorptive stripping voltammetry at a mercury electrode, Anal. Chim. Acta. 503 (2004) 213–221. https://doi.org/10.1016/j.aca.2003.10.032.

[135] P.C. do Nascimento, M. da S. Marques, M. Hilgemann, L.M. de Carvalho, D. Bohrer, S.G. Pomblum, S. Schirmer, Simultaneous determination of cadmium, copper, lead and zinc in amino acid parenteral nutrition solutions by anodic stripping voltammetry and sample digestion by UV iIrradiation, Anal. Lett. 39 (2006) 777–790. https://doi.org/10.1080/00032710600611558.

[136] G. Mattsson, L. Nyholm, Å. Olin, U. Örnemark, Determination of selenium in freshwaters by cathodic stripping voltammetry after UV irradiation, Talanta. 42 (1995) 817–825. https://doi.org/10.1016/0039-9140(95)01494-V.

[137] W.D. Ellis, Anodic stripping voltammetry, J. Chem. Educ. 50 (1973) A131. https://doi.org/10.1021/ed050pA131.

[138] L.M. de Carvalho, G. Schwedt, G. Henze, S. Sander, Redoxspeciation of selenium in water samples by cathodic stripping voltammetry using an automated flow system, Analyst. 124 (1999) 1803–1809. https://doi.org/10.1039/a906469i.

[139] J. Wang, Stripping analysis: principles, instrumentation, and applications, Vch Pub, 1985.

[140] S.B. Hocevar, I. Švancara, B. Ogorevc, K. Vytřas, Antimony film electrode for electrochemical stripping analysis, Anal. Chem. 79 (2007) 8639–8643. https://doi.org/10.1021/ac070478m.

[141] K. Brainina, E. Neyman, Electroanalytical stripping methods, John Wiley & Sons Inc, 1994.

[142] R. Kalvoda, Review of adsorptive stripping voltammetry — assessment and prospects, Fresenius. J. Anal. Chem. 349 (1994) 565–570. https://doi.org/10.1007/BF00323458.

[143] G. Herzog, V. Beni, Stripping voltammetry at micro-interface arrays: A review, Anal. Chim. Acta. 769 (2013) 10–21. https://doi.org/10.1016/j.aca.2012.12.031.

[144] R. Murry, Molecular design of electrode surfaces, Techniques of chemistry, 1992.

[145] A. Walcarius, M. Etienne, G. Herzog, V. Urbanova, N. Vilà, Electrode materials (bulk materials and modification), in: Environ. Anal. by Electrochem. Sensors Biosens., Springer New York, NY, 2014: pp. 403–495. https://doi.org/10.1007/978-1-4939-0676-5_16.

[146] R.W. Murray, Chemically modified electrodes, Acc. Chem. Res. 13 (1980) 135–141. https://doi.org/10.1021/ar50149a002.

[147] I. Svancara, K. Kalcher, A. Walcarius, K. Vytras, Electroanalysis with carbon paste electrodes, CRC Press, 2012. https://doi.org/10.1201/b11478.

[148] J.J. BelBruno, Molecularly imprinted polymers, Chem. Rev. 119 (2019) 94–119. https://doi.org/10.1021/acs.chemrev.8b00171.

[149] A. Bossi, F. Bonini, A.P.F. Turner, S.A. Piletsky, Molecularly imprinted polymers for the recognition of proteins: The state of the art, Biosens. Bioelectron. 22 (2007) 1131–1137. https://doi.org/10.1016/j.bios.2006.06.023.

[150] G. Herzog, D.W.M. Arrigan, Application of disorganized monolayer films on gold electrodes to the prevention of surfactant inhibition of the voltammetric detection of trace metals via anodic stripping of underpotential deposits: Detection of copper, Anal. Chem. 75 (2003) 319–323. https://doi.org/10.1021/ac026093f.

[151] J. Gong, T. Zhou, D. Song, L. Zhang, X. Hu, Stripping voltammetric detection of mercury(II) based on a bimetallic Au-Pt inorganic-organic hybrid nanocomposite modified hlassy carbon electrode, Anal. Chem. 82 (2010) 567–573. https://doi.org/10.1021/ac901846a.

[152] J.L. Amphlett, G. Denuault, Scanning electrochemical microscopy (SECM): An investigation of the effects of tip geometry on amperometric tip response, J. Phys. Chem. B. 102 (1998) 9946–9951. https://doi.org/10.1021/jp982829u.

[153] P.K. Hansma, B. Drake, O. Marti, S.A.C. Gould, C.B. Prater, The scanning ion-conductance microscope, Science (80). 243 (1989) 641–643. https://doi.org/10.1126/science.2464851.

[154] M.E. Snowden, A.G. Güell, S.C.S. Lai, K. McKelvey, N. Ebejer, M.A. O'Connell, A.W. Colburn, P.R. Unwin, Scanning electrochemical cell microscopy: Theory and experiment for quantitative high resolution spatially-resolved voltammetry and simultaneous ion-conductance measurements, Anal. Chem. 84 (2012) 2483–2491. https://doi.org/10.1021/ac203195h.

[155] M. Saqib, Y. Fan, R. Hao, B. Zhang, Optical imaging of nanoscale electrochemical interfaces in energy applications, Nano Energy. 90 (2021) 106539. https://doi.org/10.1016/j.nanoen.2021.106539.

[156] S. Wang, X. Huang, X. Shan, K.J. Foley, N. Tao, Electrochemical surface plasmon resonance: Basic formalism and experimental validation, Anal. Chem. 82 (2010) 935–941. https://doi.org/10.1021/ac902178f.

[157] Y. Chen, D. Zhao, J. Fu, X. Gou, D. Jiang, H. Dong, J.-J. Zhu, In situ imaging facet-induced spatial heterogeneity of electrocatalytic reaction activity at the subparticle level via electrochemiluminescence microscopy, Anal. Chem. 91 (2019) 6829–6835. https://doi.org/10.1021/acs.analchem.9b01044.

[158] J.P. Guerrette, S.J. Percival, B. Zhang, Fluorescence coupling for direct imaging of electrocatalytic heterogeneity, J. Am. Chem. Soc. 135 (2013) 855–861. https://doi.org/10.1021/ja310401b.

[159] B. Liu, S.A. Rotenberg, M. V. Mirkin, Scanning electrochemical microscopy of

living cells: Different redox activities of nonmetastatic and metastatic human breast cells, Proc. Natl. Acad. Sci. 97 (2000) 9855–9860. https://doi.org/10.1073/pnas.97.18.9855.

[160] T. Sun, Y. Yu, B.J. Zacher, M. V Mirkin, Scanning electrochemical microscopy of individual catalytic nanoparticles, Angew. Chemie Int. Ed. 53 (2014) 14120–14123. https://doi.org/10.1002/anie.201408408.

[161] G.A. Snook, T.D. Huynh, A.F. Hollenkamp, A.S. Best, Rapid SECM probing of dissolution of $LiCoO_2$ battery materials in an ionic liquid, J. Electroanal. Chem. 687 (2012) 30–34. https://doi.org/10.1016/j.jelechem.2012.08.021.

[162] Y. González-García, S.J. García, A.E. Hughes, J.M.C. Mol, A combined redox-competition and negative-feedback SECM study of self-healing anticorrosive coatings, Electrochem. Commun. 13 (2011) 1094–1097. https://doi.org/10.1016/j.elecom.2011.07.009.

[163] S. Cannan, J. Cervera, R.J. Steliaros (née Haskins), E. Bitziou, A.L. Whitworth, P.R. Unwin, Scanning electrochemical microscopy (SECM) studies of catalytic EC′ processes: theory and experiment for feedback, generation/collection and imaging measurements, Phys. Chem. Chem. Phys. 13 (2011) 5403. https://doi.org/10.1039/c0cp02530e.

[164] K. Eckhard, X. Chen, F. Turcu, W. Schuhmann, Redox competition mode of scanning electrochemical microscopy (RC-SECM) for visualisation of local catalytic activity, Phys. Chem. Chem. Phys. 8 (2006) 5359. https://doi.org/10.1039/b609511a.

[165] D. Filotás, B.M. Fernández-Pérez, J. Izquierdo, A. Kiss, L. Nagy, G. Nagy, R.M. Souto, Improved potentiometric SECM imaging of galvanic corrosion reactions, Corros. Sci. 129 (2017) 136–145. https://doi.org/10.1016/j.corsci.2017.10.006.

[166] K. Mahankali, N.K. Thangavel, L.M. Reddy Arava, In situ electrochemical mapping of lithium–sulfur battery interfaces using AFM–SECM, Nano Lett. 19 (2019) 5229–5236. https://doi.org/10.1021/acs.nanolett.9b01636.

[167] S. Krämer, R.R. Fuierer, C.B. Gorman, Scanning probe lithography using self-assembled monolayers, Chem. Rev. 103 (2003) 4367–4418. https://doi.org/10.1021/cr020704m.

[168] J. Xiang, J. Guo, F. Zhou, Scanning electrochemical microscopy combined with surface plasmon resonance: Studies of localized film thickness variations

and molecular conformation changes, Anal. Chem. 78 (2006) 1418–1424. https://doi.org/10.1021/ac051601h.

[169] D.J. Comstock, J.W. Elam, M.J. Pellin, M.C. Hersam, Integrated ultramicroelectrode−nanopipet probe for concurrent scanning electrochemical microscopy and scanning ion conductance microscopy, Anal. Chem. 82 (2010) 1270–1276. https://doi.org/10.1021/ac902224q.

[170] L. Guerret-Legras, J.F. Audibert, I.M.G. Ojeda, G.V. Dubacheva, F. Miomandre, Combined SECM-fluorescence microscopy using a water-soluble electrofluorochromic dye as the redox mediator, Electrochim. Acta. 305 (2019) 370–377. https://doi.org/10.1016/j.electacta.2019.03.069.

[171] B. Paulose Nadappuram, K. McKelvey, J.C. Byers, A.G. Güell, A.W. Colburn, R.A. Lazenby, P.R. Unwin, Quad-barrel multifunctional electrochemical and ion conductance probe for voltammetric analysis and imaging, Anal. Chem. 87 (2015) 3566–3573. https://doi.org/10.1021/acs.analchem.5b00379.

[172] F. GE, R.C. TENENT, D.O. WIPF, Fabricating and imaging carbon-fiber immobilized enzyme ultramicroelectrodes with scanning electrochemical microscopy., Anal. Sci. 17 (2001) 27–35. https://doi.org/10.2116/analsci.17.27.

[173] C. Deng, M. Li, Q. Xie, M. Liu, Q. Yang, C. Xiang, S. Yao, Construction as well as EQCM and SECM characterizations of a novel Nafion/glucose oxidase-glutaraldehyde/poly(thionine)/Au enzyme electrode for glucose sensing, Sensors Actuators B Chem. 122 (2007) 148–157. https://doi.org/10.1016/j.snb.2006.05.017.

[174] B.R. Horrocks, D. Schmidtke, A. Heller, A.J. Bard, Scanning electrochemical microscopy. 24. Enzyme ultramicroelectrodes for the measurement of hydrogen peroxide at surfaces, Anal. Chem. 65 (1993) 3605–3614. https://doi.org/10.1021/ac00072a013.

[175] N. Matsui, T. Kaya, K. Nagamine, T. Yasukawa, H. Shiku, T. Matsue, Electrochemical mutagen screening using microbial chip, Biosens. Bioelectron. 21 (2006) 1202–1209. https://doi.org/10.1016/j.bios.2005.05.004.

[176] J. Mauzeroll, E.A. Hueske, A.J. Bard, Scanning electrochemical microscopy. 48. Hg/Pt hemispherical ultramicroelectrodes: Fabrication and characterization, Anal. Chem. 75 (2003) 3880–3889. https://doi.org/10.1021/ac034088l.

[177] Y. Lee, S. Amemiya, A.J. Bard, Scanning electrochemical microscopy. 41. theory and characterization of ring electrodes, Anal. Chem. 73 (2001) 2261–

2267. https://doi.org/10.1021/ac0014764.

[178] M. Nebel, S. Neugebauer, K. Eckhard, W. Schuhmann, Ring-disk microelectrodes for simultaneous constant-distance and constant-current mode scanning electrochemical microscopy, Electrochem. Commun. 27 (2013) 160–163. https://doi.org/10.1016/j.elecom.2012.11.028.

[179] L. Danis, D. Polcari, A. Kwan, S.M. Gateman, J. Mauzeroll, Fabrication of carbon, gold, platinum, silver, and mercury ultramicroelectrodes with controlled geometry, Anal. Chem. 87 (2015) 2565–2569. https://doi.org/10.1021/ac503767n.

[180] D. Polcari, P. Dauphin-Ducharme, J. Mauzeroll, Scanning Electrochemical Microscopy: A Comprehensive Review of Experimental Parameters from 1989 to 2015, (2016). https://doi.org/10.1021/acs.chemrev.6b00067.

[181] Y. Takahashi, A.I. Shevchuk, P. Novak, Y. Murakami, H. Shiku, Y.E. Korchev, T. Matsue, Simultaneous noncontact topography and electrochemical imaging by SECM/SICM featuring ion current feedback regulation, J. Am. Chem. Soc. 132 (2010) 10118–10126. https://doi.org/10.1021/ja1029478.

[182] S. Fang, H.J. Lee, A.W. Wark, R.M. Corn, Attomole microarray detection of microRNAs by nanoparticle-amplified SPR imaging measurements of surface polyadenylation reactions, J. Am. Chem. Soc. 128 (2006) 14044–14046. https://doi.org/10.1021/ja065223p.

[183] V.T. Nguyen, H. Bin Seo, B.C. Kim, S.K. Kim, C.S. Song, M.B. Gu, Highly sensitive sandwich-type SPR based detection of whole H_5N_x viruses using a pair of aptamers, Biosens. Bioelectron. 86 (2016) 293–300. https://doi.org/10.1016/j.bios.2016.06.064.

[184] C. CAMPBELL, G. KIM, SPR microscopy and its applications to high-throughput analyses of biomolecular binding events and their kinetics, Biomaterials. 28 (2007) 2380–2392. https://doi.org/10.1016/j.biomaterials.2007.01.047.

[185] C.E. Wagner, L.J.A. Macedo, A. Opdahl, Temperature gradient approach for rapidly assessing sensor binding kinetics and thermodynamics, Anal. Chem. 87 (2015) 7825–7832. https://doi.org/10.1021/acs.analchem.5b01518.

[186] R. Orlowski, H. Raether, The total reflection of light at smooth and rough silver films and surface plasmons, Surf. Sci. 54 (1976) 303–308. https://doi.org/10.1016/0039-6028(76)90227-2.

[187] R.J. Green, R.A. Frazier, K.M. Shakesheff, M.C. Davies, C.J. Roberts, S.J.B. Tendler, Surface plasmon resonance analysis of dynamic biological interactions with biomaterials, Biomaterials. 21 (2000) 1823–1835. https://doi.org/10.1016/S0142-9612(00)00077-6.

[188] S. Wang, X. Huang, X. Shan, K.J. Foley, N. Tao, Electrochemical surface plasmon resonance: Basic formalism and experimental validation, Anal. Chem. 82 (2010) 935–941. https://doi.org/10.1021/ac902178f.

[189] Y. Fang, H. Wang, H. Yu, X. Liu, W. Wang, H.-Y. Chen, N.J. Tao, Plasmonic imaging of electrochemical reactions of single nanoparticles, Acc. Chem. Res. 49 (2016) 2614–2624. https://doi.org/10.1021/acs.accounts.6b00348.

[190] Y. Wang, X. Shan, S. Wang, N. Tao, P.-Y. Blanchard, K. Hu, M. V Mirkin, Imaging local electric field distribution by plasmonic impedance microscopy, Anal. Chem. 88 (2016) 1547–1552. https://doi.org/10.1021/acs.analchem.5b04382.

[191] Y. Wang, H. Wang, Y. Chen, Y. Wang, H. Chen, X. Shan, N. Tao, Fast electrochemical and plasmonic detection reveals multitime scale conformational gating of electron transfer in Cytochrome c, J. Am. Chem. Soc. 139 (2017) 7244–7249. https://doi.org/10.1021/jacs.7b00839.

[192] D. Jiang, Y. Jiang, Z. Li, T. Liu, X. Wo, Y. Fang, N. Tao, W. Wang, H.Y. Chen, Optical imaging of phase transition and Li-ion diffusion kinetics of single $LiCoO_2$ nanoparticles during electrochemical cycling, J. Am. Chem. Soc. 139 (2017) 186–192. https://doi.org/10.1021/jacs.6b08923.

[193] J. Zhao, S. Xue, R. Ji, B. Li, J. Li, Localized surface plasmon resonance for enhanced electrocatalysis, Chem. Soc. Rev. 50 (2021) 12070–12097. https://doi.org/10.1039/D1CS00237F.

[194] M. Kitta, K. Murai, K. Yoshii, H. Sano, Electrochemical surface plasmon resonance spectroscopy for investigation of the initial process of lithium metal deposition, J. Am. Chem. Soc. 143 (2021) 11160–11170. https://doi.org/10.1021/jacs.1c04934.

[195] J. Zhao, C. Zhang, Y. Lu, Q. Wu, Y. Yuan, M. Xu, J. Yao, Surface-enhanced Raman spectroscopic investigation on surface plasmon resonance and electrochemical catalysis on surface coupling reaction of pyridine at Au/TiO_2 junction electrodes, J. Raman Spectrosc. 51 (2020) 2199–2207. https://doi.org/10.1002/jrs.5982.

[196] R. Kurita, Y. Yokota, A. Ueda, O. Niwa, Electrochemical surface plasmon resonance measurement in a microliter volume flow cell for evaluating the affinity and catalytic activity of biomolecules, Anal. Chem. 79 (2007) 9572–9576. https://doi.org/10.1021/ac071412u.

[197] L.R.F. Allen J. Bard, Electrochemical methods: Fundamentals and Applications, Wiley; 2nd edition, 2000.

[198] H.Y. Li, S.M. Zhou, J. Li, Y.L. Chen, S.Y. Wang, Z.C. Shen, L.Y. Chen, H. Liu, X.X. Zhang, Analysis of the Drude model in metallic films, Appl. Opt. 40 (2001) 6307. https://doi.org/10.1364/AO.40.006307.

[199] K.J. Foley, X. Shan, N.J. Tao, Surface impedance imaging technique, Anal. Chem. 80 (2008) 5146–5151. https://doi.org/10.1021/ac800361p.

[200] M. Hasheminejad, Y. Fang, M. Li, Y. Jiang, W. Wang, H.Y. Chen, Plasmonic imaging of the interfacial potential distribution on bipolar electrodes, Angew. Chemie. 129 (2017) 1651–1655. https://doi.org/10.1002/ange.201611235.

[201] Y. Fang, W. Wang, X. Wo, Y. Luo, S. Yin, Y. Wang, X. Shan, N. Tao, Plasmonic imaging of electrochemical oxidation of single nanoparticles, J. Am. Chem. Soc. 136 (2014) 12584–12587. https://doi.org/10.1021/ja507097y.

[202] X. Shan, I. Díez-Pérez, L. Wang, P. Wiktor, Y. Gu, L. Zhang, W. Wang, J. Lu, S. Wang, Q. Gong, J. Li, N. Tao, Imaging the electrocatalytic activity of single nanoparticles, Nat. Nanotechnol. 7 (2012) 668–672. https://doi.org/10.1038/nnano.2012.134.

[203] E. Yoo, J. Kim, E. Hosono, H. shen Zhou, T. Kudo, I. Honma, Large reversible Li storage of graphene nanosheet families for use in rechargeable Lithium ion batteries, Nano Lett. 8 (2008) 2277–2282. https://doi.org/10.1021/nl800957b.

[204] N. Liu, Z. Lu, J. Zhao, M.T. McDowell, H.-W. Lee, W. Zhao, Y. Cui, A pomegranate-inspired nanoscale design for large-volume-change lithium battery anodes, Nat. Nanotechnol. 9 (2014) 187–192. https://doi.org/10.1038/nnano.2014.6.

[205] L.S. Dolci, S. Zanarini, L. Della Ciana, F. Paolucci, A. Roda, Development of a new device for ultrasensitive electrochemiluminescence microscopy imaging, Anal. Chem. 81 (2009) 6234–6241. https://doi.org/10.1021/ac900756a.

[206] J. Dong, Y. Xu, Z. Zhang, J. Feng, Operando imaging of chemical activity on gold plates with single-molecule electrochemiluminescence microscopy, Angew. Chemie. 134 (2022). https://doi.org/10.1002/ange.202200187.

[207] C. Ma, Y. Cao, X. Gou, J.-J. Zhu, Recent progress in electrochemiluminescence sensing and imaging, Anal. Chem. 92 (2020) 431–454. https://doi.org/10.1021/acs.analchem.9b04947.

[208] R.A. Marcus, On the theory of chemiluminescent electron-transfer reactions, J. Chem. Phys. 43 (1965) 2654–2657. https://doi.org/10.1063/1.1697190.

[209] B. Fleet, G.F. Kirkbright, C.J. Pickford, The electrogenerated chemiluminescence of pyrene and some related compounds, J. Electroanal. Chem. Interfacial Electrochem. 30 (1971) 115–121. https://doi.org/10.1016/0368-1874(71)85039-6.

[210] R.Y. Lai, A.J. Bard, Electrogenerated chemiluminescence. 70. The application of ECL to determine electrode potentials of Tri- n -propylamine, its radical cation, and intermediate free radical in MeCN/Benzene solutions, J. Phys. Chem. A. 107 (2003) 3335–3340. https://doi.org/10.1021/jp026743j.

[211] X. Liu, L. Shi, W. Niu, H. Li, G. Xu, Environmentally friendly and highly sensitive ruthenium(II) Tris(2,2′-bipyridyl) electrochemiluminescent system using 2-(Dibutylamino)ethanol as co-reactant, Angew. Chemie Int. Ed. 46 (2007) 421–424. https://doi.org/10.1002/anie.200603491.

[212] J.P. Choi, K.T. Wong, Y.M. Chen, J.K. Yu, P.T. Chou, A.J. Bard, Electrogenerated chemiluminescence. 76. Excited singlet state emission vs excimer emission in Ter(9,9-diarylfluorene)s, J. Phys. Chem. B. 107 (2003) 14407–14413. https://doi.org/10.1021/jp036140n.

[213] W. Miao, J.P. Choi, A.J. Bard, Electrogenerated chemiluminescence 69: The Tris(2,2‘-bipyridine)ruthenium(II), ($Ru(bpy)_3^{2+}$)/Tri- n -propylamine (TPrA) system revisitedA new route involving $TPrA^{\bullet+}$ cation radicals, J. Am. Chem. Soc. 124 (2002) 14478–14485. https://doi.org/10.1021/ja027532v.

[214] C.A. Marquette, L.J. Blum, Electro-chemiluminescent biosensing, Anal. Bioanal. Chem. 390 (2008) 155–168. https://doi.org/10.1007/s00216-007-1631-2.

[215] W. Zhao, H.Y. Chen, J.J. Xu, Electrogenerated chemiluminescence detection of single entities, Chem. Sci. 12 (2021) 5720–5736. https://doi.org/10.1039/D0SC07085H.

[216] M.M. Chen, W. Zhao, M.J. Zhu, X.L. Li, C.H. Xu, H.Y. Chen, J.J. Xu, Spatiotemporal imaging of electrocatalytic activity on single 2D gold nanoplates via electrogenerated chemiluminescence microscopy, Chem. Sci. 10

(2019) 4141–4147. https://doi.org/10.1039/C9SC00889F.

[217] A.J. Wilson, K. Marchuk, K.A. Willets, Imaging electrogenerated chemiluminescence at single gold nanowire electrodes, Nano Lett. 15 (2015) 6110–6115. https://doi.org/10.1021/acs.nanolett.5b02383.

[218] M.J. Zhu, J. Bin Pan, Z.Q. Wu, X.Y. Gao, W. Zhao, X.H. Xia, J.J. Xu, H.Y. Chen, Electrogenerated chemiluminescence imaging of electrocatalysis at a single Au-Pt janus nanoparticle, Angew. Chemie. 130 (2018) 4074–4078. https://doi.org/10.1002/ange.201800706.

[219] K. Ma, Y. Zhang, L. Liu, J. Xi, X. Qiu, T. Guan, Y. He, In situ mapping of activity distribution and oxygen evolution reaction in vanadium flow batteries, Nat. Commun. 10 (2019) 5286. https://doi.org/10.1038/s41467-019-13147-9.

[220] Y. He, G. Pan, L. Li, S. Zhong, L. Li, Z. Liu, Y. Yu, Local charge transfer within a covalent organic framework and Pt nanoparticles promoting interfacial catalysis, Catal. Sci. Technol. 12 (2022) 3240–3246. https://doi.org/10.1039/D1CY02024B.

[221] A. Almalla, A. Hertwig, D. Fischer, O. Ozcan, J. Witt, Development of layer-by-layer assembled thin coatings on aluminium alloy AA2024-T3 for high resolution studies of local corrosion processes, J. Appl. Polym. Sci. 137 (2020) 49826. https://doi.org/10.1002/app.49826.

[222] X. Yang, X. Li, S.D. Khochare, P. Ruchhoeft, W.C. Shih, X. Shan, Imaging the electrochemical impedance of single cells via conductive polymer thin film, ACS Sensors. 6 (2021) 485–492. https://doi.org/10.1021/acssensors.0c02051.

[223] D. Momotenko, J.C. Byers, K. McKelvey, M. Kang, P.R. Unwin, High-speed electrochemical imaging, ACS Nano. 9 (2015) 8942–8952. https://doi.org/10.1021/acsnano.5b02792.

[224] W. Guo, P. Zhou, L. Sun, H. Ding, B. Su, Microtube electrodes for imaging the electrochemiluminescence layer and deciphering the reaction mechanism, Angew. Chemie. 133 (2021) 2117–2121. https://doi.org/10.1002/ange.202012340.

[225] X. Shan, U. Patel, S. Wang, R. Iglesias, N. Tao, Imaging local electrochemical current via surface plasmon resonance, Science 327 (2010) 1363–1366. https://doi.org/10.1126/science.1186476.

[226] J. Lu, W. Wang, S. Wang, X. Shan, J. Li, N. Tao, Plasmonic-based electrochemical impedance spectroscopy: Application to molecular binding,

Anal. Chem. 84 (2012) 327–333. https://doi.org/10.1021/ac202634h.

[227] R. Liu, X. Shan, H. Wang, N. Tao, Plasmonic measurement of electron transfer between a single metal nanoparticle and an electrode through a molecular layer, J. Am. Chem. Soc. 141 (2019) 11694–11699. https://doi.org/10.1021/jacs.9b05388.

[228] S.M. Oja, B. Zhang, Imaging transient formation of diffusion layers with fluorescence-enabled electrochemical microscopy, Anal. Chem. 86 (2014) 12299–12307. https://doi.org/10.1021/ac5035715.

[229] Y. Ma, C. Colin, J. Descamps, S. Arbault, N. Sojic, Shadow electrochemiluminescence microscopy of single mitochondria, Angew. Chemie Int. Ed. 60 (2021) 18742–18749. https://doi.org/10.1002/ANIE.202105867.

[230] J. Zhang, R. Jin, D. Jiang, H.-Y. Chen, Electrochemiluminescence-based capacitance microscopy for label-free imaging of antigens on the cellular plasma membrane, J. Am. Chem. Soc. 141 (2019) 10294–10299. https://doi.org/10.1021/jacs.9b03007.

[231] M.M. Richter, Electrochemiluminescence (ECL), Chem. Rev. 104 (2004) 3003–3036. https://doi.org/10.1021/cr020373d.

[232] S.K. Deb, Opportunities and challenges of electrochromic phenomena in transition metal oxides, Sol. Energy Mater. Sol. Cells. 25 (1992) 327–338. https://doi.org/10.1016/0927-0248(92)90077-3.

[233] C. GRANQVIST, Electrochromic oxides: A unified view, Solid State Ionics. 70–71 (1994) 678–685. https://doi.org/10.1016/0167-2738(94)90393-X.

[234] M. Wang, X. Xing, I.F. Perepichka, Y. Shi, D. Zhou, P. Wu, H. Meng, Electrochromic smart windows can achieve an absolute private state through thermochromically engineered electrolyte, Adv. Energy Mater. 9 (2019) 1900433. https://doi.org/10.1002/aenm.201900433.

[235] J. Jensen, H.F. Dam, J.R. Reynolds, A.L. Dyer, F.C. Krebs, Manufacture and demonstration of organic photovoltaic-powered electrochromic displays using roll coating methods and printable electrolytes, J. Polym. Sci. Part B Polym. Phys. 50 (2012) 536–545. https://doi.org/10.1002/polb.23038.

[236] R.M. Sapstead, N. Corden, A. Robert Hillman, Latent fingerprint enhancement via conducting electrochromic copolymer films of pyrrole and 3,4-ethylenedioxythiophene on stainless steel, Electrochim. Acta. 162 (2015) 119–128. https://doi.org/10.1016/j.electacta.2014.11.061.

[237] M.A. Farahmand Nejad, S. Ranjbar, C. Parolo, E.P. Nguyen, R. Álvarez-Diduk, M.R. Hormozi-Nezhad, A. Merkoçi, Electrochromism: An emerging and promising approach in (bio)sensing technology, Mater. Today. 50 (2021) 476–498. https://doi.org/10.1016/j.mattod.2021.06.015.

[238] V. Rai, R.S. Singh, D.J. Blackwood, D. Zhili, A review on recent advances in electrochromic devices: A material approach, Adv. Eng. Mater. 22 (2020) 2000082. https://doi.org/10.1002/adem.202000082.

[239] R.J. Mortimer, Organic electrochromic materials, Electrochim. Acta. 44 (1999) 2971–2981. https://doi.org/10.1016/S0013-4686(99)00046-8.

[240] R.J. Mortimer, A.L. Dyer, J.R. Reynolds, Electrochromic organic and polymeric materials for display applications, Displays. 27 (2006) 2–18. https://doi.org/10.1016/j.displa.2005.03.003.

[241] M. Nicho, Synthesis of derivatives of polythiophene and their application in an electrochromic device, Sol. Energy Mater. Sol. Cells. 82 (2004) 105–118. https://doi.org/10.1016/j.solmat.2004.01.009.

[242] K.J. Patel, G.G. Bhatt, J.R. Ray, P. Suryavanshi, C.J. Panchal, All-inorganic solid-state electrochromic devices: a review, J. Solid State Electrochem. 21 (2017) 337–347. https://doi.org/10.1007/s10008-016-3408-z.

[243] M. Gugole, O. Olsson, S. Rossi, M.P. Jonsson, A. Dahlin, Electrochromic inorganic nanostructures with high chromaticity and superior brightness, Nano Lett. 21 (2021) 4343–4350. https://doi.org/10.1021/acs.nanolett.1c00904.

[244] C.. Granqvist, Electrochromic tungsten oxide films: Review of progress 1993–1998, Sol. Energy Mater. Sol. Cells. 60 (2000) 201–262. https://doi.org/10.1016/S0927-0248(99)00088-4.

[245] M. Dhanasankar, K.K. Purushothaman, G. Muralidharan, Optical, structural and electrochromic studies of molybdenum oxide thin films with nanorod structure, Solid State Sci. 12 (2010) 246–251. https://doi.org/10.1016/j.solidstatesciences.2009.10.021.

[246] P. Liu, Electrochromic and chemochromic performance of mesoporous thin-film vanadium oxide, Solid State Ionics. 165 (2003) 223–228. https://doi.org/10.1016/j.ssi.2003.08.044.

[247] J. Kim, M. Rémond, D. Kim, H. Jang, E. Kim, Electrochromic conjugated polymers for multifunctional smart windows with integrative functionalities, Adv. Mater. Technol. 5 (2020) 1900890.

https://doi.org/10.1002/admt.201900890.

[248] Y.S. Zou, Y.C. Zhang, D. Lou, H.P. Wang, L. Gu, Y.H. Dong, K. Dou, X.F. Song, H.B. Zeng, Structural and optical properties of WO_3 films deposited by pulsed laser deposition, J. Alloys Compd. 583 (2014) 465–470. https://doi.org/10.1016/j.jallcom.2013.08.166.

[249] V.K. Thakur, G. Ding, J. Ma, P.S. Lee, X. Lu, Hybrid materials and polymer electrolytes for electrochromic device applications, Adv. Mater. 24 (2012) 4071–4096. https://doi.org/10.1002/adma.201200213.

[250] V.K. Thakur, G. Ding, J. Ma, P.S. Lee, X. Lu, Hybrid materials and polymer electrolytes for electrochromic device applications, Adv. Mater. 24 (2012) 4071–4096. https://doi.org/10.1002/adma.201200213.

[251] M. Deepa, M. Kar, S.A. Agnihotry, Electrodeposited tungsten oxide films: annealing effects on structure and electrochromic performance, Thin Solid Films. 468 (2004) 32–42. https://doi.org/10.1016/j.tsf.2004.04.056.

[252] P. Ashrit, Transition metal oxide thin film-based chromogenics and devices, Elsevier: Amsterdam, the Netherlands, 2017.

[253] G. Zhang, K. Lu, X. Zhang, W. Yuan, M. Shi, H. Ning, R. Tao, X. Liu, R. Yao, J. Peng, Effects of annealing temperature on optical band gap of sol-gel tungsten trioxide films, Micromachines. 9 (2018) 377. https://doi.org/10.3390/mi9080377.

[254] J. Zhang, R. Jin, D. Jiang, H.-Y. Chen, Electrochemiluminescence-based capacitance microscopy for label-free imaging of antigens on the cellular plasma membrane, J. Am. Chem. Soc. 141 (2019) 10294–10299. https://doi.org/10.1021/jacs.9b03007.

[255] K.J. Patel, C.J. Panchal, M.S. Desai, P.K. Mehta, An investigation of the insertion of the cations H^+, Na^+, K^+ on the electrochromic properties of the thermally evaporated WO_3 thin films grown at different substrate temperatures, Mater. Chem. Phys. 124 (2010) 884–890. https://doi.org/10.1016/J.MATCHEMPHYS.2010.08.021.

[256] Q. Liu, C. Ma, X.P. Liu, Y.P. Wei, C.J. Mao, J.J. Zhu, A novel electrochemiluminescence biosensor for the detection of microRNAs based on a DNA functionalized nitrogen doped carbon quantum dots as signal enhancers, Biosens. Bioelectron. 92 (2017) 273–279. https://doi.org/10.1016/j.bios.2017.02.027.

[257] W. Xu, K. Fu, P.W. Bohn, Electrochromic sensor for multiplex detection of metabolites enabled by closed bipolar electrode coupling, ACS Sensors. 2 (2017) 1020–1026. https://doi.org/10.1021/acssensors.7b00292.

[258] G. Feng, J. Guo, H. Tian, Z. Li, Y. Shi, X. Li, X. Yang, D. Mayerich, Y. Yang, X. Shan, Probe the localized electrochemical environment effects and electrode reaction dynamics for metal batteries using in situ 3D microscopy, Adv. Energy Mater. 12 (2022) 2103484. https://doi.org/10.1002/aenm.202103484.

[259] H. Ding, W. Guo, B. Su, Imaging cell-matrix adhesions and collective migration of living cells by electrochemiluminescence microscopy, Angew. Chemie. 132 (2020) 457–464. https://doi.org/10.1002/ange.201911190.

[260] Q. Xia, X. Chen, C. Liu, R. Bin Song, Z. Chen, J. Zhang, J. jie Zhu, Label-free probing of electron transfer kinetics of single microbial cells on a single-layer graphene via structural color microscopy, Nano Lett. 21 (2021) 7823–7830. https://doi.org/10.1021/acs.nanolett.1c02828.

[261] D.L. Robinson, B.J. Venton, M.L.A. V Heien, R.M. Wightman, Detecting subsecond dopamine release with fast-scan cyclic voltammetry in vivo, Clin. Chem. 49 (2003) 1763–1773. https://doi.org/10.1373/49.10.1763.

[262] W. Dungchai, O. Chailapakul, C.S. Henry, Electrochemical detection for paper-based microfluidics, Anal. Chem. 81 (2009) 5821–5826. https://doi.org/10.1021/ac9007573.

[263] A.K. Srivastava, M. Deepa, S. Singh, R. Kishore, S.A. Agnihotry, Microstructural and electrochromic characteristics of electrodeposited and annealed WO_3 films, Solid State Ionics. 176 (2005) 1161–1168. https://doi.org/10.1016/J.SSI.2004.10.006.

[264] C.L. Sun, H.H. Lee, J.M. Yang, C.C. Wu, The simultaneous electrochemical detection of ascorbic acid, dopamine, and uric acid using graphene/size-selected Pt nanocomposites, Biosens. Bioelectron. 26 (2011) 3450–3455. https://doi.org/10.1016/j.bios.2011.01.023.

[265] R.F. Brocenschi, T.A. Silva, B.C. Lourencao, O. Fatibello-Filho, R.C. Rocha-Filho, Use of a boron-doped diamond electrode to assess the electrochemical response of the naphthol isomers and to attain their truly simultaneous electroanalytical determination, Electrochim. Acta. 243 (2017) 374–381. https://doi.org/10.1016/j.electacta.2017.05.044.

[266] K.C. Honeychurch, Printed thick-film biosensors, in: Print. Film., Elsevier,

2012: pp. 366–409. https://doi.org/10.1533/9780857096210.2.366.

[267] R.A. Cottis, Electrochemical methods, in: Shreir's Corros., Elsevier, 2010: pp. 1341–1373. https://doi.org/10.1016/B978-044452787-5.00068-8.

[268] Q. Qin, Y. Guo, Preparation and characterization of nano-polyaniline film on ITO conductive glass by electrochemical polymerization, J. Nanomater. 2012 (2012) 1–6. https://doi.org/10.1155/2012/519674.

[269] O. Bohnke, B. Vuillemin, Proton insertion into thin films of amorphous WO_3: kinetics study, Mater. Sci. Eng. B. 13 (1992) 243–246. https://doi.org/10.1016/0921-5107(92)90172-6.

[270] L. Liu, S. Yellinek, I. Valdinger, A. Donval, D. Mandler, Important implications of the electrochemical reduction of ITO, Electrochim. Acta. 176 (2015) 1374–1381. https://doi.org/10.1016/j.electacta.2015.07.129.

[271] J.N. Gaur, G.M. Schmid, Electrochemical behavior of gold in acidic chloride solutions, J. Electroanal. Chem. Interfacial Electrochem. 24 (1970) 279–286. https://doi.org/10.1016/S0022-0728(70)80152-8.

[272] Y. Shi, G. Feng, X. Li, X. Yang, A.H. Ghanim, P. Ruchhoeft, D. Jackson, S. Mubeen, X. Shan, Electrochemical impedance imaging on conductive surfaces, Anal. Chem. 93 (2021) 12320–12328. https://doi.org/10.1021/acs.analchem.1c02040.

[273] Y. Wu, B. Zhu, M. Huang, L. Liu, Q. Shi, M. Akbar, C. Chen, J. Wei, J.F. Li, L.R. Zheng, J.S. Kim, H.B. Song, Proton transport enabled by a field-induced metallic state in a semiconductor heterostructure, Science 369 (2020) 184–188. https://doi.org/10.1126/science.aaz9139.

[274] Y. Zheng, Y. Zhang, Z. Wang, Y. Liu, M. He, P. Wu, Synthesis of stainless-steel-net supported TS-1 catalyst and its catalytic performance in liquid-phase epoxidation reactions, Ind. Eng. Chem. Res. 50 (2011) 9587–9593. https://doi.org/10.1021/ie200757f.

[275] C.M. Sánchez-Sánchez, J. Rodríguez-López, A.J. Bard, Scanning electrochemical microscopy. 60. quantitative calibration of the SECM substrate generation/tip collection mode and its use for the study of the oxygen reduction mechanism, Anal. Chem. 80 (2008) 3254–3260. https://doi.org/10.1021/ac702453n.

[276] B. Grant, N.J. Clecak, M. Oxsen, A. Jaffe, G.S. Keller, Study of the electrochromism of methoxyfluorene compounds, J. Org. Chem. 45 (1980)

702–705. https://doi.org/10.1021/jo01292a030.

Appendix

Chemicals

The specifications for all the chemicals used in the different experimental procedures can be found in **Table 1** as follows:

Table 1: Chemicals and reagents used in the experiments

Chemical name	Molecular formula	Molar mass	Purity	Supplier
Nitric acid	HNO_3	63.01	65%	Sigma
Sodium Nitrate	$NaNO_3$	84.99	99.5%	Prolabo
Copper Sulfate	$CuSO_4$	159.61	99%	Sigma
Ferrocenedimethanol	$Fc(MeOH)_2$	246.08	97%	Sigma
Sulphuric acid	H_2SO_4	98.08	98%	Sigma
Hydrogen peroxide	H_2O_2	34.1	30%	–
Ammonium hydroxide	$NH_3 \cdot H_2O$	35.05	25%	–
Tungsten powder	W	183.84	99.99%	–
platinum on carbon powder	Pt/C		10 wt.% loading	–
2,5-Dihydroxybenzoic acid	$C_7H_6O_4$	154.12	98%	–
Aniline	$C_6H_5NH_2$	93.13	99.5%	–

All reagents were of analytical grade and used without further purification. Deionized water obtained from a Millipore water purification system (⩾18 MΩ cm, 25 °C, Milli-Q, Millipore Co.) was used in all experiments.